BIO-INSPIRED ROBOT DESIGN WITH COMPLIANT UNDERACTUATED SYSTEMS

A DISSERTATION
SUBMITTED TO THE DEPARTMENT OF MECHANICAL ENGINEERING
AND THE COMMITTEE ON GRADUATE STUDIES
OF STANFORD UNIVERSITY
IN PARTIAL FULFILLMENT OF THE REQUIREMENTS
FOR THE DEGREE OF
DOCTOR OF PHILOSOPHY

Sangbae Kim
March 2008

I certify that I have read this dissertation and that, in my opinion, it is fully adequate in scope and quality as a dissertation for the degree of Doctor of Philosophy.

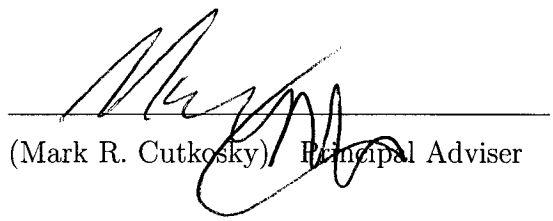

(Mark R. Cutkosky) Principal Adviser

I certify that I have read this dissertation and that, in my opinion, it is fully adequate in scope and quality as a dissertation for the degree of Doctor of Philosophy.

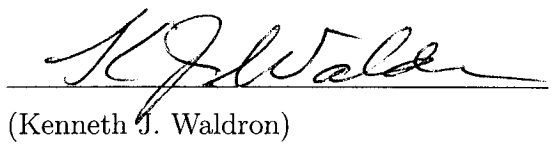

(Kenneth J. Waldron)

I certify that I have read this dissertation and that, in my opinion, it is fully adequate in scope and quality as a dissertation for the degree of Doctor of Philosophy.

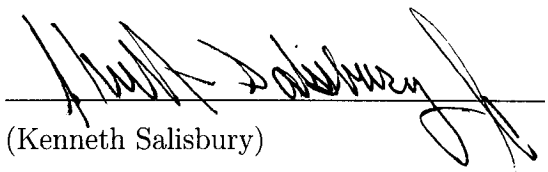

(Kenneth Salisbury)

Approved for the University Committee on Graduate Studies.

Abstract

Mobile robot designers are increasingly searching for inspiration and design cues from biological models. Biomechanical studies of running animals underscore the importance of the passive properties of muscles, tendons and other elements of the musculoskeletal system. These elements play significant roles in self stabilization and elastic energy storage, resulting in smoother and more efficient locomotion. Although the animals' systems are extremely complex, they frequently behave as though following a simpler dynamic template when executing repetitive motions, as in walking, running or climbing. Consequently, for operation under limited circumstances, a bio-inspired robot often needs only to match a simplified approximation to the animal's behavior. This observation motivates the use of under-actuated compliant mechanisms, in which a modest number of independently controlled actuators are augmented with passive compliant elements. The resulting mechanisms can execute periodic trajectories that are functions of external loads, as well as actuator inputs, to approximate the behaviors seen in nature.

Underactuated compliant mechanisms also afford practical advantages to the robot designer. The elastic elements provide a lower mechanical impedance and allow for better force control when paired with geared servo motors. They also increase the physical robustness of the mechanisms and isolate the motors from shock when unexpected impacts occur.

Guided by these considerations, this thesis explores a particular class of underactuated compliant mechanism that is particularly suitable for the legs of small bio-inspired robots. The thesis begins by establishing the general motivation, terminology and analysis framework for this class of mechanism. The subsequent chapters

explore applications of the approach through three bio-inspired robots. The compliant mechanisms used in each of the three robots are created using a multi-material rapid-prototyping process, Shape Deposition Manufacturing, which allows hard and soft materials to be combined in a single structure.

The first of three robot examples is *iSprawl*, a cockroach-inspired hexapod with compliant, underactuated legs. Passive hip joints and a light and flexible push-pull cable transmission in the axial direction allow the legs to cycle very rapidly for a 14Hz stride frequency. Tuning of the leg properties, based on high-speed video observations and force measurements, allowed the speed of *iSprawl* to increase from five to fifteen body-lengths per second. The second bio-inspired robot example is *Spinybot*, a hexapod that climbs rough surfaces including stucco, concrete and brick walls using toes with miniature spines. An underactuated leg mechanism cycles the toes through a sequence of contacting the wall, engaging the spines, applying loads, disengaging the spines and repositioning the foot at each step. Nonlinear compliances in the toe linkages help to distribute forces and keep the spines engaged for reliable climbing. The third robot is *Stickybot*, a gecko-inspired quadruped that climbs smooth vertical surfaces using directional dry adhesion. *Stickybot* contains several types of underactuated mechanisms in its body, legs and toes. At the smallest length scale, the undersides of the toes are covered with a unique material called directional polymeric stalks, inspired by the directional setae and lamellae of the gecko. The combination of directional adhesion and a hierarchy of compliant mechanisms allows *Stickybot* to distribute forces evenly over the toes and to attach and detach its feet from surfaces with a minimum of effort. The result is very smooth, gecko-like climbing, achieved with a simple control system.

Acknowledgments

I would like to thank my adviser, my parents, family and friends for all the support along the way. I would also like to thank all current and past members of the Biomimetics and Dextrous Manipulation Lab (BDML), the Center for Design Research (CDR) and other Stanford affiliates that I have worked with.

Contents

Abstract iv

Acknowledgments vi

1 Introduction 1

1.1 Motivation 1

1.2 Biologically-inspired compliant underactuated design 4

1.2.1 Bioinspired design process 8

1.3 Thesis Overview 9

1.4 Contributions 10

2 Compliant underactuated systems 12

2.1 Scope of the problem 12

2.1.1 Definition of an underactuated compliant system 16

2.1.2 Foot trajectory 17

2.1.3 Compliance matrix 20

2.1.4 Compliance Superposition 23

2.1.5 Design procedure of compliant mechanisms in bio-inspired robots 25

2.2 Differential system 28

3 iSprawl: running with passive dynamics 30

3.1 Introduction 30

3.2 Mechanical Design of *iSprawl* 33

3.2.1 Leg trajectory 35

3.3 Tuning Parameters for Smooth Open-Loop Running 37
3.3.1 Desired Leg Extension Profile 39
3.3.2 Performance 44
3.3.3 Energetics 46
3.3.4 Ground Reaction Forces 47
3.4 Summary 49

4 Spinybot: Climbing with compliant microspines **51**
4.1 Introduction 51
4.2 Spine and Surface scaling 52
4.3 Toe and Foot Design: Promoting Attachment and Load Sharing . . . 54
4.4 Underactuated leg design 61
4.5 Body Design: Promoting Load Sharing and Stability 65
4.6 Discussion 68
4.6.1 Adapting Spines to Heavier Robots 70

5 Stickybot : Climbing with Directional adhesion **72**
5.1 Introduction 72
5.2 Adhesion and Compliance 75
5.2.1 Hierarchical Conformability in the Gecko 77
5.2.2 Hierarchical Conformability in Stickybot 78
5.3 Directional Friction and Adhesion 82
5.4 Distributed Force Control 89
5.4.1 Distributed Force Control in the Gecko 89
5.4.2 Distributed Force Control in Stickybot 89
5.4.3 Leg compliance design for force control 90
5.4.4 Force Sensors 92
5.4.5 Force Controller 93
5.5 Results 95
5.6 Discussion 99

6 Conclusions **102**

6.1 Summary 102

6.2 Future directions 104

A Appendices **107**

A.1 Crank-Slider Kinematics 107

A.2 Spine Failure Modes 108

A.3 R_a and R_q Calculation 111

Bibliography **112**

List of Tables

3.1 Physical Parameters for *iSprawl* 37

3.2 Parameters for Single Analytic Leg Model in Figure 3.6 39

4.1 SpinybotII Toe Compliance Matrices 59

4.2 Compliances and Damping Parameters for Toe Linkage 60

4.3 SpinybotII Specifications 66

4.4 Effect of Scaling Parameters on Toe Compliances. Desired suspension compliances in the x- and y-directions (i.e., $1/k_{xx}$ and $1/k_{yy}$, respectively) vary as a function of robot weight, spine size and number of spines. The values in the table show how the compliances should be varied to maintain a constant x-direction compliance for the entire foot, and appropriate displacements in the y-direction, to engage most of the spines while not over-extending them. Usually the required number of toes n depends on the spine size, leading to $n \propto 1/r_s$ for a constant robot mass. 68

5.1 Physical Parameters for *Stickybot* 100

List of Figures

1.1 A good golf swing requires little distal motion during the acceleration period. The relative positions of the club, arm, and shoulder remain at almost the same configuration during downswing, when most of energy is transfered from the legs to the arms. A major portion of the power is gained from the uncoiling motion of the upper body and the torso from (a) to (b). At the body configuration shown (a), the shoulder and the wrist muscles are fully stretched, which is the best position to transmit large forces (and one of the worst positions to actively generate contracting forces). (c)(top) shows the rough trend of muscle force-speed relationship based on A.V. Hill's equation; (c)(bottom) shows the length-tension relationship of active (stimulated) and passive (unstimulated) skeletal muscle [115, 59] 2

1.2 (a) Long ligaments, tendon and small pennate muscles in the horse's leg are morphologically advantageous for a faster stride and elastic energy storage. (b) Ligaments are part of the construction of the human foot and provide additional compliance in walking and running. The drawing shows the plantar fascia, one of the tissues supporting weight, and storing and releasing energy, in human locomotion. 3

1.3 Biological observation leads to the hypothesis of a simplified dynamic model, the spring-loaded inverted pendulum, which can be applied to a robotic system [50]. 6

1.4 A design process for bio-inspired robots 8

2.1 An example of an underactuated leg of a bio-inspired robot: the number of degrees of freedom describing the position and orientation of the foot in the plane is three, but there are five parameters needed to define the state of the loaded system. 14
2.2 Trajectory of a leg in 2-dimensional space (left) and corresponding periodic actuator input (right). 15
2.3 (a) Trajectory of hip joint observed in the ground coordinate frame. In the case of a running robot with compliances, the trajectory of the hip joint is usually concave during the stance phase. (b) Correspodning trajectory of the foot in a coordinate frame attached to the hip joint. 18
2.4 Comparison between unloaded and loaded trajectory. When there is no external force on foot, the foot follows the unloaded trajectory. During stance phase, the foot follows the inverse of the hip joint trajectory with a ground reaction force in the body coordinate frame. 19
2.5 Compliance matrix in the body coordinate frame and in the foot coordinate frame 21
2.6 Compliance calculation for combination of springs, by superposition. . 24
2.7 Compliance superposition in 2-D linkages 25
2.8 (left)Schematics of iSprawl leg. Rotational hip joint is passive and prismatic joint is actuated with serial axial compliance. (right) Sequence of the leg movement. 26
2.9 Rocker-bogie linkage system and hydraulic differential 29

3.1 *iSprawl*: a fully autonomous hexapedal robot driven by an electric motor and flexible push-pull cables. 32
3.2 Power transmission system for *iSprawl*. A double crank-slider is used to store and convert the rotational energy from the motor to linear oscillations. 34
3.3 Power transmission system for *iSprawl*. Schematic sketch shows the flexible and rigid sections of the push-pull cables. 35

3.4 Schematic of the leg design of iSprawl shows the unloaded trajectory and nominal loaded trajectory of the foot. Flexible polymeric joints provide rotational compliance. Axial compliance is realized with a rubber tube in the sleeve that guides the cable, as shown in Figure 3.5 36
3.5 Schematic of the leg compression spring design utilizing a tension spring in the flexible sleeve around the push-pull cable. Also shown are the frictional dampers (on front and middle legs). 38
3.6 Schematic of the desired leg extension profile needed to produce a sinusoidal trajectory of the center of mass during stance. Dashed line shows trajectory that would occur without compression assuming that the foot stays in contact to the ground based only on a kinematic relationship. (In practice, the body trajectory will not exactly follow this kinematic approximation. In particular, the transition between the end of the dotted curve and the solid curve would not be as abrupt.) 40
3.7 The theoretical and experimental leg extension profiles for *iSprawl* running at 2.3 m/s. Also shown are the path of the COM and the extension of the axial spring for each case. The dashed line in the analytical plot shows COM trajectory that would occur without any spring compression. Curves for the measured leg extension and COM trajectory represent averages of three successive strides shown in gray dots. . . . 41
3.8 Running speed of *iSprawl* vs. stride frequency 44
3.9 Electrical power consumption of *iSprawl* without load and with running load. 46
3.10 Specific resistance vs. speed for *iSprawl* running on smooth terrain. . 47
3.11 The vertical and horizontal individual leg ground reaction forces for a cockroach and *Sprawlita* [4] and for *iSprawl*, in comparison to the idealized SLIP model [9]. 48

4.1 Profile photograph of typical spine, with shaft dia., $d = 270\mu m$ and tip radius $r_s = 10\mu m$, engaging a rough profile of 80 grit aluminum oxide sandpaper. 55

4.2 Picture of upper section of SpinybotII on concrete wall and detailed view of several spines independently engaging asperities on the concrete surface. 56
4.3 Photograph and equivalent elastic linkages for one toe of the climbing robot. Linkage at left shows the deflected position for a 40g load, superimposed on the undeflected position (shown in dotted lines). Key to labels: **1.** 200 mm diameter spines (inside dotted circles), **2.** tendon for applying loads, **3.** soft urethane flexure permitting travel in y direction, **4.** buckling flexures with large compliance value in the $-x$ direction under compression, lower compliance under tension, **5.** primarily rotational flexure for the proximal spine, **6.** buckling/lift-off flexure for proximal spine. 57
4.4 Side and plan view of one foot containing ten toes. The toes can deflect independently of each other. In addition, the entire foot can displace in the distal (y) direction due to an un-actuated prismatic joint. . . 62
4.5 The sequence of motions is accomplished using an underactuated mechanism consisting of a single rotary RC servo motor and an elastic band that is taut while the foot is disengaged. **Top**: Tension in rubber band helps engagment of spines to asperities. **Middle**: When the foot is engaged, the loose elastic band prevents forces that would push the robot away from the wall. **bottom**: A hard stop causes the leg to lift off the wall as the servo rotates upward, with the elastic band keeping the leg pushed against the hard stop. 63
4.6 Photograph of SpinybotII wall and diagram of climbing mechanism. Each set of three legs is attached to a mechanism that allows the robot to "ratchet" its way up the wall with an alternating tripod gait. A long tail helps to reduce the pitching moment. The center of mass (COM) is within the polygon of contacts, to minimize yawing rotations in the plane of the wall. 67

4.7 Photograph of new toe design. For heavier robots, this toe design is thinner and studier at higher forces. Flexure(white part) angle is aligned in various angle from bottom structure such that the toe produce nonlinear stiffness. 70

5.1 Stickybot, a new bio-inspired robot capable of climbing smooth surfaces. Inset: detail of toes curling to facilitate detachment. 73
5.2 Modulus of bulk material and feature size of distal end of different structures. Microstructured geometries can lower the overall stiffness of bulk materials so that they become tacky. This principle allows geckos to use β-keratin for their adhesive structures. At smaller scales, tip geometry plays a less important role in adhesion forces, for a given bulk material modulus. 75
5.3 Hierarchy of compliant structures in the gecko for conforming at many length scales. (From [14], reprinted with the permission of K. Autumn). 78
5.4 The elements of Stickybot's hierarchical compliance over a range of length scales. 79
5.5 Schematic of cross section view of Stickybot toe fabricated via Shape Deposition Manufacturing. 80
5.6 Two stage differential system actuated by a single push-pull actuator. It facilitates conformation on uneven surfaces and distributes the contact forces among four toes. 81
5.7 Details of nomenclature used to calculate cable profile of the toes. . . 82
5.8 Anisotropic stalks comprised of 20 Shore-A polyurethane. Stalks measure 380 μm in diameter at the base. The base angle is 20° and the tip angle is 45°. 82
5.9 Molding process used to fabricate anisotropic patches. Mold is manufactured out of hard wax and then filled with liquid urethane polymer. A cap eliminates contact with air and creates final tip geometry. . . 84

5.10 Comparison of the frictional-adhesion model [12] and the Johnson-Kendall-Roberts (JKR) model [69] with pulloff force data from a single toe of Stickybot's directional adhesive patches (513 stalks). (A) When dragged against the preferred direction, the directional patch exhibits friction and no adhesion. (B) When dragged in the preferred direction, the directional patch demonstrates adhesion proportional to the shear force, albeit with saturation at the highest levels (unlike gecko setae). (C) The frictional-adhesion model has an upper shear force limit. In comparison, the JKR model shows the typical behavior of an isotropic elastic material with adhesion. 85
5.11 Pulloff data for the DPS patches in the normal-lateral plane. Data is shown for two different levels of tangential force, approximately 0 N and 1.5 N. 87
5.12 Schematic of optimal tangential forces for a planar two-legged climber under isotropic versus anisotropic adhesion at different inclinations. Arrow directions and magnitudes shown in proportion to optimal tangential forces (dot represents zero tangential force). 88
5.13 (left) Stickybot loaded and unloaded foot trajectories are shown in the sagittal plane(y-z), (right) Schematic representation of the wing compliance and the force-deflection relationship for a linear spring as compared to the preloaded case. 91
5.14 Stickybot leg compliances are shown in the dorsal plane (x-y). The tangential force sensor measures deflection of serial compliance element at the shoulder joint. 93
5.15 Unfiltered tangential force sensor readings compared to tangential and lateral forces measured using a force plate mounted to a load cell. . . 94
5.16 Schematic used to generate values for the grasp matrix 95
5.17 Force plate data of rear left foot (left) and front right foot (right) of Stickybot climbing with a 6s period at a speed of 1.5cm/s. Data filtered at 10Hz. Two successive runs are shown to illustrate repeatability. . . 96

5.18 Comparison of normal force profiles of anisotropic and isotropic patches on a climbing robot. Point A on the curves refers to the preloading phase of the cycle. Point B highlights when the foot is in the adhesive regime during a stroke. Points C and D are when the foot is unloaded and detached, causing large normal forces in the case of the isotropic patch. 97

5.19 Tangential and normal contact forces of StickyBots front left foot during one climbing step. Approximate (Eq. 1) contact limit surface for one foot based on tests of individual DPS patches is also shown. Initial normal preload (A) brings DPS patches into contact with the climbing substrate and then increasing tangential force allows the foot to sustain the required adhesive loads (A-B). At the end of stance (B) the right front foot is brought into contact, increasing the adhesive force at the left foot (C). Smooth detachment is achieved by moving the contact force to the origin in force-space and intersecting the limit surface (D). 99

A.1 Schematic of Crank and Slider 107

A.2 Curved beam with variables used in spine failure mode analysis. . . . 109

Chapter 1

Introduction

1.1 Motivation

Golfers and tennis players are often taught to "Swing with the body." One of the interpretations of this concept is that players should transfer the energy from the body to the club or racket while keeping their arm muscles passive. During the initial acceleration period, kinetic energy, initiated with motions of the legs and torso, is transmitted to the tip of the club or racket through the musculoskeletal structure and realizes a high velocity at the distal end. Throughout this period, arm muscles are in tension but do not actively impart motions. At first glance, this advice may seem counterintuitive, as the muscles in the arms, wrist and hand are smaller, closer to the club or racquet, and presumably capable of finer control than those in the torso. Indeed, in an expert's swing, a higher impact can be achieved by actively providing additional speed and stiffening distal muscles at or just before impact. However, many beginners and intermediate players are prone to exert undesirable forces in the distal muscles, producing a slower tip velocity or less accurate positioning.

For beginners, the best swing often can be achieved by focusing on big muscles in the body with a minimum of control in the arm and hand, relying on natural power transfer through the passive dynamics of arm structure as shown in Fig.1.1. This passive swing regime may be related to the intrinsic characteristic of the muscle. According to A. V. Hill's equation of the force-velocity relationship of muscle [116],

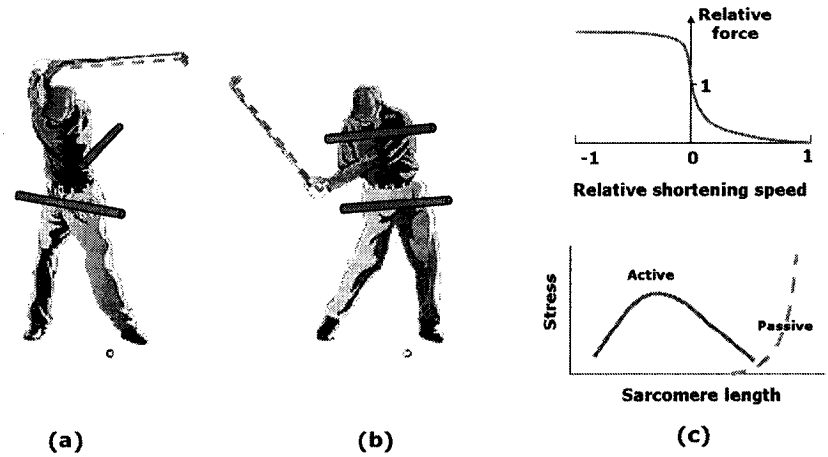

Figure 1.1: A good golf swing requires little distal motion during the acceleration period. The relative positions of the club, arm, and shoulder remain at almost the same configuration during downswing, when most of energy is transfered from the legs to the arms. A major portion of the power is gained from the uncoiling motion of the upper body and the torso from (a) to (b). At the body configuration shown (a), the shoulder and the wrist muscles are fully stretched, which is the best position to transmit large forces (and one of the worst positions to actively generate contracting forces). (c)(top) shows the rough trend of muscle force-speed relationship based on A.V. Hill's equation; (c)(bottom) shows the length-tension relationship of active (stimulated) and passive (unstimulated) skeletal muscle [115, 59]

the maximum tension on muscle can be much higher when the muscle is extending or resisting motion than that when it is actively contracting. Therefore, even a small muscle can transmit a large amount of energy as long as it is not contracting but extending or resisting, as seen in Fig.1.1(c). Taking advantage of this characteristic, it may be that the players are maintaining a higher tension when they keep their arm muscles passive than when they try to actively move them during the swing. Alternatively, it may be that with little time to respond, beginners are better off adopting an appropriate passive compliance in the arm and allowing an open-loop force/motion trajectory to guide the hand. Also, keeping the arm muscles passive may improve swing consistency, since we need to pay attention to only a few muscles to control a

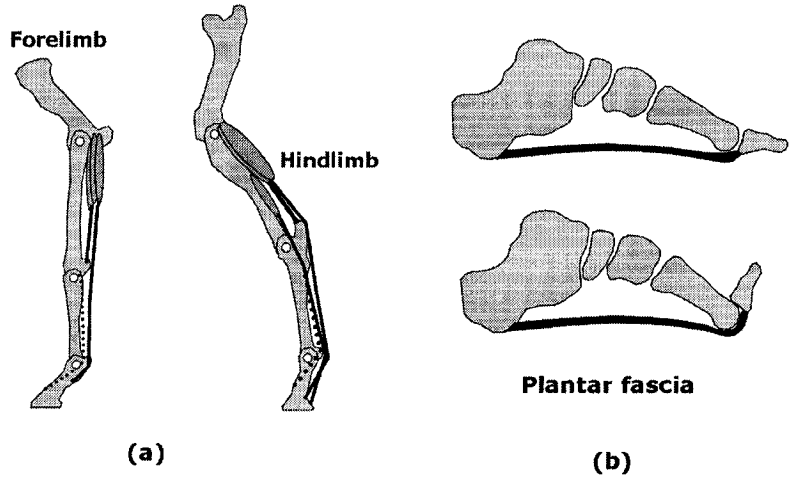

Figure 1.2: (a) Long ligaments, tendon and small pennate muscles in the horse's leg are morphologically advantageous for a faster stride and elastic energy storage. (b) Ligaments are part of the construction of the human foot and provide additional compliance in walking and running. The drawing shows the plantar fascia, one of the tissues supporting weight, and storing and releasing energy, in human locomotion.

complex system and the passive arm behaves in a predictable way. Additionally, the arm muscles are less prone to fatigue when they work passively since their metabolic energy consumption is significantly lower than normal operation [5]. For these particular tasks where the motion is rather simple and energetic, some muscles perform better behaving as passive elements.

The passive role of muscle is also apparently crucial in legged locomotion. Smaller distal muscles with tendons and ligaments enable much more efficient locomotion by providing elastic energy storage and passive stabilization. The gastrocnemius muscles of many ungulates have long tendons which, as basic elastic elements, provide shock absorption and energy storage (Fig.1.2). Biologists present evidence of the importance of tendon elasticity in many vertebrates. The horse gastrocnemius tendon, significantly longer than the muscle, stores energy in a similar way to a spring in cyclic locomotion [4]. Similarly, kangaroo rats [20, 3] exhibit elastic energy storage in tendons of the gastrocnemius muscles. In the running turkey, the amount of energy recovered by tendons is bigger than that of active contraction of the gastrocnemius

muscle [106]. These examples attest to the importance of compliance and energy storage in the musculoskeletal system.

The musculoskeletal system is not only elastic, but visco-elastic, which is useful for the stabilization of locomotion. For example, the energy dissipation in the exoskeleton of an insect contributes to its stability when running over rough terrain [81, 53, 90, 89]. Biological observations indicate that cockroaches run over rough terrain without significant speed reduction and without significant changes in the EMG signals to their leg muscles [48]. In other words, dynamic adjustment of the motor control pattern is not required to maintain stability. The effect can be thought of as similar to well-tuned automobile suspension, which soaks up bumps without throwing the car off course. According to Full and Farley [48], "Many think that the brain is issuing orders and commands. But we believe the nerve system can only make suggestions, which are compromised and reconciled with the mechanical system's own mind."

Insect morphology seems to have several advantages in conjunction with the "passive muscle" concept. Proximal muscles are usually bigger and stronger and distal muscles are lighter and smaller. First, the low mass of the distal leg reduces the acceleration torque required at the hip joint. With a smaller rotational inertia about the hip, the legs can also achieve a faster return motion and, hence, a higher stride frequency resulting in faster and more efficient running [88]. In addition, a lighter distal leg dissipates less energy through impacts. Upon contact with the ground, the kinetic energy of a colliding mass (e.g. the foot) is dissipated through forms of heat, vibration, and sound. Thus, a smaller and lighter distal leg can create smoother motion and a more efficient transformation between kinetic and potential energy.

1.2 Biologically-inspired compliant underactuated design

In comparison to the use of passive mechanisms in animals, the traditional approach to robot actuation and control has followed a very different path. The most commonly used actuators are electromagnetic motors which, although well suited for precise

control, have severe limitations in terms of shape and power density. In addition, because electric motors are ill suited for low speeds and high forces or torques, they require transmissions with large speed reductions when connected to the joints of a robot. The transmissions typically reduce the overall efficiency and result in large reflected inertias (proportional to the square of the speed ratio) at the tips of the legs. An alternative solution for power transmission has been devised using cable mechanisms [107] for smoother force response and removal of backlash. However, the problem of reflected inertia remains and the mechanics of routing cables around joints and keeping them tensioned properly can lead to complex designs.

In addition to limitations in actuation, the control and sensing capabilities of robots are impoverished in comparison to those of animals. Robotic sensors are inferior, with lower dynamic range and sparse distribution in comparison to their natural counterparts. Conventionally, sensing and controlling each additional degree of freedom is expensive. The complexity of supplying power and signals to the joints of a robot grows at least as the square of the number of actuators. These limitations reduce the dexterity of robots and prevent them from responding gracefully to high speed landings and unexpected contact loads. To overcome these limitations, passive mechanical properties can be advantageous. For example, compliance in the leg can help to accommodate and moderate the complicated dynamic interactions of the foot with the environment without requiring extra actuators, sensors and controlled degrees of freedom at the ankle or foot.

Interestingly, some biologists believe that simplified models can accurately describe the behavior of complex biological systems in routine, steady-state operation. There is some indication that biological systems, although they are incredibly complex in comparison to the most sophisticated robots, are often controlled to behave as though they were simple, or as though they were following a relatively simple "dynamic template." Cavagna introduced the spring-mass model [29] for legged-locomotion. The relationship between the effective stiffness of legs and gait is detailed by a simple spring leg model [87]. Blickhan describes extensive work on a spring-mass model for running and hopping [24]. The concept of a dynamic "template and anchor" provides a more generalized methodology [51] for explaining why animals may

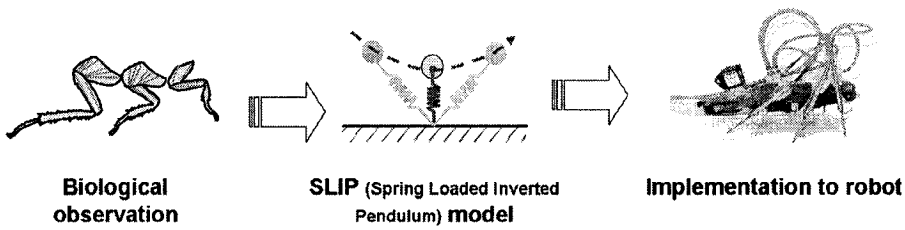

Figure 1.3: Biological observation leads to the hypothesis of a simplified dynamic model, the spring-loaded inverted pendulum, which can be applied to a robotic system [50].

control complex musculoskeletal systems to behave like simpler systems. By seeking synergies and symmetries [105], the "template" can suggest a generic, reduced model that helps to implement the main principles and motion control strategies. The "anchor" guides low level strategies for embedding templates in elaborated models that reveal more details of locomotion.

As an extraordinary example of the potential of simplified passive mechanisms, in Paralympics competitions, a lightweight compliant prosthetic foot has been designed to enable amputees to run as fast as normal athletes [93]. In 2008, runner Oscar Pistorius was denied a shot at the Olympics due to the "unfair advantage" in speed and energy consumption afforded by his prosthetic carbon-fiber feet [2]. In this example, although the prosthetic leg cannot replace all the functions of a biological leg, it approximates the passive functions of muscle and tendon for energy storage and stabilization during running to afford an advantage.

In summary, there are strong motivations to identify passive mechanical systems that can reduce the total number of actuators and thereby simplify the overall control problem while helping to maintain stability. As animals exploit the mechanical characteristics of tendons and ligaments, running robots need to incorporate passive compliance in their legs in order to smooth the ground reaction force and achieve efficient locomotion. An additional advantage is that passive compliant mechanisms are often physically robust – certainly more robust than corresponding mechanisms with stiff links and multiple small actuators. For limited tasks, such as running or

walking, simple underactuated mechanisms can approximate the passive functions of the biological models and even exceed their performance.

In recent work, robotic designers, drawing upon an understanding of biomechanics, have been implementing passive features in their designs to compensate for the limitations of actuators and control systems. Pratt shows that the advantages of serial compliance in actuator design include improved shock tolerance, lower reflected inertia, accurate and stable force control, and a capacity for energy storage [101, 102]. The resulting designs sustain less inadvertent damage to the environment and the machine when unexpected contacts or loads occur. Several multi-legged robots have been developed using serial passive elastic elements as replacements for actuated degrees of freedom. For example, *Rhex*[108] utilizes rotational actuators with axial (radial) compliance in its legs. The *Sprawl* robots [30, 74] have prismatic actuators for leg extension and passive hip joints. *Puppy* [66] presents dynamic running with active shoulder actuators and passive knee joints. *Scout 2* [100] has axial prismatic compliance. These robots are all examples of the succcessful exploitation of passive self-stabilization characteristics of compliant leg design, roughly analogous to biological examples utilizing muscles and tendons ror running.

Another class of passive design is the differential mechanism, which is often used in robotic and prosthetic grippers to approximate human grasping without recourse to many independently actuated degrees of freedom. One early underactuated prosthetic hand was designed with sensory feedback control [117]. Its simple elastic coupling and underactuated fingers helped to reduce the control effort of users. Hirose introduced the "Active Cord Mechanism" (ACM), composed of serial linkages controlled by one cable actuated in a coupled mechanism [64, 63]. By taking advantage of a differential system, the serial links can passively conform to an object and distribute the force over the contact surface. In a more recent prosthetic hand design, additional springs between linkages help balance forces along the fingers, helping them to conform to objects [27]. In the palm of this hand, a differential mechanism distributes the overall grasp force between fingers so that the entire grasp can be accomplished with a single actuator [84]. In other work, the forces and kinematics of multi-phalanx underactuated finger systems have been studied in detail [22, 23]. In the area of mobile robots,

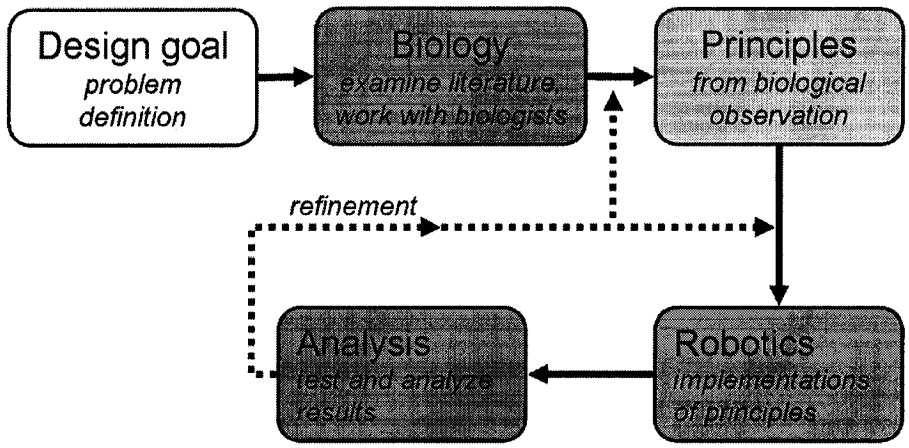

Figure 1.4: A design process for bio-inspired robots

an innovative passive "legged wheel" design is found in the *Shrimp* robot [112], capable of rolling across highly unstructured terrain without costly sensors and feedback control.

1.2.1 Bioinspired design process

As indicated in Figure 1.4, the process of bio-inspired robot design begins with the careful study of exemplars from nature. However, transferring ideas from the biological world to the mechanical design space is more involved than simply reproducing the physical structures found in animals. Bio-inspired robot design requires multiple interdisciplinary processes, including defining the design goal, searching for biological analogies, extracting general principles from observations, and implementing those principles in an iterative process of design, evaluation and refinement.

As a starting point, the design goal for the robot needs to be clearly defined. The inspiration may stem from a designer's curiosity about how some animal accomplishes a particular feat, such as scampering up a vertical wall. The next stage is to identify multiple examples from nature and to learn about the structures, materials, control

systems and behaviors that allow them to accomplish desired functions. Conversations with biologists are invaluable for identifying a range of animal examples and for pointers to the literature concerning their morphology and operation. Although the animal examples are generally impressive, it is important to remember that nature does not produce optimal solutions in any formal sense. Rather, nature works on the principle of what is "good enough" to afford a competitive advantage. In addition, the structures observed in animals are typically required to fulfill many functions in addition to those of interest to the designer. For example, one cannot take a dog's leg as the ideal model for running given that the dog uses its leg for many other functions too. Sometimes, comparing homologous features among several species helps to remove bias from the interpretation. Through cautious observation and reasoning, we can extract hypotheses about the principles that govern the animals' behavior and performance. The next step is, selectively, to implement the principles in a robot. Since mechanical components differ from biological organisms, the principles need to be adapted in an artificial design space. It is not desirable to simply replace the biological features with mechanical counterparts since artificial design elements differ greatly from natural ones. The underlying functional principles need to be extracted from biology, digested by the designer and reincarnated. Modification of the principles through subsequent experimentations and analysis will ultimately provide refinement of the principles, and will accordingly improve the final design.

1.3 Thesis Overview

The approach taken in this thesis follows the general pattern of Figure 1.4. The work is restricted to a particular class of robotic applications and mechanisms, as defined in Chapter 2, which introduces a framework for describing and analyzing compliant, quasi-static underactuated mechanisms. The next chapters provide several detailed examples of the approach. Chapter 3 focuses on the design and analysis of a bio-inspired running robot, highlighting its unique power transmission system and underactuated leg design. The robot's legs are made out of a combination of hard and soft polymeric material and are tuned for smooth and fast running. Chapter 4

focuses on Spinybot, an exterior-wall-climbing robot which utilizes micro spines with a soft, independent suspension system. Spinybot's underactuated legs are designed to change their compliance as the feet travel along a trajectory, to facilitate engaging asperities on the surface and to distribute the climbing loads. Chapter 5 focuses on Stickybot, a robot that exploits directional dry adhesion for climbing smooth surfaces. It has four limbs and 12 actuators, presenting a highly underactuated system with over 30 degree of freedom for distributing the forces. Directional Polymeric Stalks (DPS) are designed for generating directional adhesion that allows control of adhesion according to the direction of loading. The last chapter concludes with a summary of the ideas presented as well as future work.

1.4 Contributions

The main contribution of this thesis is providing novel design ideas for legged robots with compliant, underactuated mechanisms. Inspired by flexible biological structures, the mechanisms allow passive adaptive behavior, self-stabilization and force distribution. The main accomplishments of this work are:

- design, analysis and testing of a novel biologically inspired compliant suspension system for a running robot that allows it to run faster than any other hexapod for its size, in terms of body-lengths per second;
- design and analysis of a new bio-inspired compliant suspension for the Spinybot climbing robot that allows it to achieve a desired foot trajectory, with desired ratios of compliances at various points along the trajectory;
- design of new bio-inspired compliant mechanisms for Stickybot that allow it to interact with vertical surfaces, distributing the forces evenly among the feet;
- design of a novel bio-inspired compliant under-actuated system that allows each of the toes of Stickybot to attach and detach and to achieve an approximately uniform pressure and shear stress distribution, in order to maximize the benefits of directional dry adhesion.

Before going into the details of each of these robotic systems, I present, in the next chapter, a framework for the definition and design of compliant under-actuated robotic mechanisms that is generally suitable for small legged robots moving at moderate speeds.

Chapter 2

Compliant underactuated systems

Before diving into detailed descriptions of various underactuated mechanisms in bio-inspired robots, it is useful to define "passive underactuated mechanisms" and to establish a notation and framework for describing such devices and their behavior. Following these definitions, this chapter proposes a design procedure that can be applied to a particular class of compliant, underactuated mechanisms associated with the limbs of bio-inspired robots.

2.1 Scope of the problem

The term "underactuated" is used to describe systems that have passive degrees of freedom. Most conventional robotic systems employ actuators at every joint, rigidly attached to the respective linkage such that the kinematic configuration is fully defined by the positions of the actuators. Unlike conventional mechanisms, underactuated systems include passive joints that allow for additional degrees of freedom. There has been significant research on the behavior of the dynamic coupling between actuated linkages and free pivot joints [7]. Utilizing similar concepts, highly energy-efficient bipedal robots are presented as a successful implementation of passive dynamics by virtue of dynamic coupling among under-actuated leg linkages [86].

The robot appendages presented in this thesis constitute a special class of underactuated mechanisms. They involve passive compliance at every joint, usually in series

with a small position-controlled servo gearmotor. They are small and light weight (e.g. in comparison to the robot body) so that the leg inertias have little effect on the dynamics of the robot. The velocities are generally low (on the order of centimeters per second), which further supports a quasi-static analysis in which damping and acceleration forces are ignored.[1] Accordingly, when analyzing the trajectories and behaviors of the limbs, it suffices to focus on their compliance and kinematics.

For the robots described in the following chapters, compliance is realized by a layered rapid prototyping process called Shape Deposition Manufacturing (SDM) [120, 21], which permits multiple grades of polymer to be incorporated in a single structure. Regions with soft, elastomeric polymers create localized compliant joints; stiff polymers (sometimes reinforced with carbon fibers and other fabrics) play the role of rigid links. Because the compliant regions are much softer than the stiff regions, this thesis uses a lumped-parameter model of passive compliance instead of a continuous elastic model. Finally, because the small robots use servo gearmotors with relatively high gear ratios, operated under position control, it is a reasonable approximation to assume that all compliance is due to the passive compliance in the joints. Where it is necessary to achieve an approximation to force control at a joint, the solution is to put an elastomeric element in series with the gearmotor and to monitor its compliant deflection, adjusting the commanded position of the gearmotor accordingly.

Assumptions

To summarize, the main assumptions and limitations associated with the design of bio-inspired appendages in this thesis are as follows:

- The problem of determining the forces on the legs is quasi-static, since the inertial and damping forces of the legs are small in comparison to those of the robot body. The forces applied to the leg consist of actuator forces and contact forces. Passive damping may be present in the legs, but does not produce large enough forces to affect the compliant deflections.

[1] The one exception to the low-speed assumption is *iSprawl*, but in this case the legs are so light that their inertial forces are still small compared to those of the robot body.

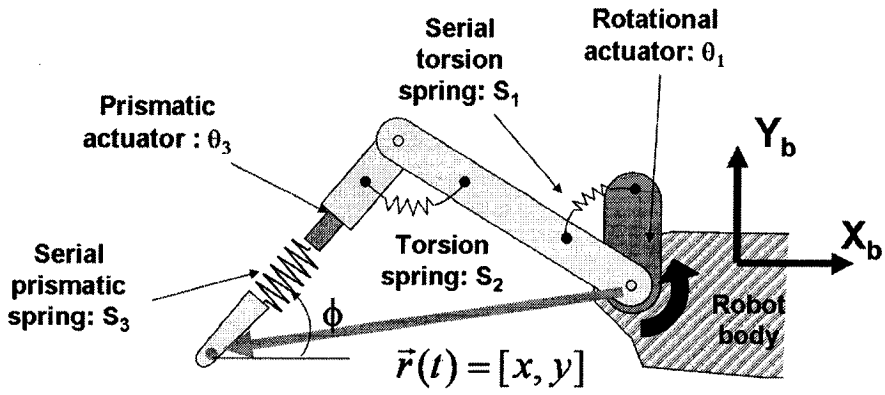

Figure 2.1: An example of an underactuated leg of a bio-inspired robot: the number of degrees of freedom describing the position and orientation of the foot in the plane is three, but there are five parameters needed to define the state of the loaded system.

- The actuators are stiff, position-controlled devices that follow a commanded trajectory. In practice, they have some servo compliance, however this compliance can be lumped into the passive compliance in series with each actuator at the joint.

- The leg compliances are concentrated at discrete locations and the compliance at each location is fixed so that a constant coefficient, lumped-parameter analysis applies.

- The leg mechanism is a statically determinate system, with a single contact, typically at the foot in normal operation. Therefore, if the contact forces at the foot are known, the compliant deflections of the leg can be calculated.

- The interaction with the ground is treated as a point contact without slip. Where the contact is clearly not a point, as in the case of *Stickybot*, the ankle is a free spherical joint so that no torques are transmitted between the leg and the ground.

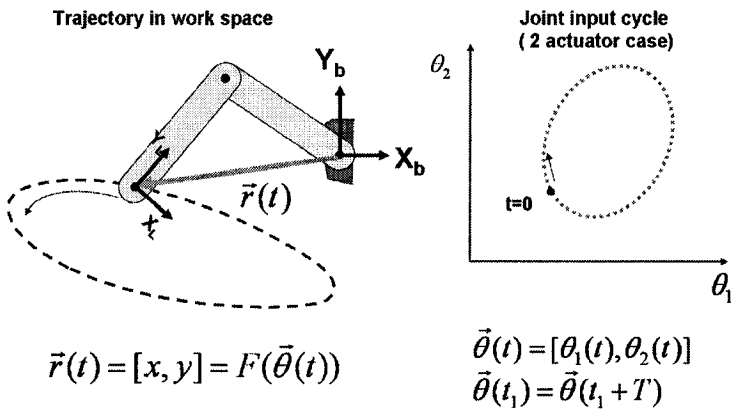

Figure 2.2: Trajectory of a leg in 2-dimensional space (left) and corresponding periodic actuator input (right).

Notation

The following notational conventions will be used in defining and analyzing compliant, underactuated robot limbs:

- θ_i represents the state of the ith joint actuator, which can be a linear or angular value depending on whether the actuator is rotational or prismatic.
- S_i represents ith joint compliant deflection with respect to an unloaded configuration. S_i can represent a rotational or linear deflection, depending on the type of joint. For example, S_2 for joint 2 in Figure 2.1 is rotational and S_3 is linear. If a joint has an actuator, but negligible compliance, then $S_i = 0$ for that joint; conversely, if a joint is purely passive, as in the case of joint 2 in Figure 2.1, then $\theta_i = 0$ and S_i fully describes the state of the joint.
- jc_i represents the magnitude of the compliance (inverse of stiffness) at the ith joint. It can represent either a rotational or linear compliance.
- For the coordinate frames, subscript b represents the body coordinate frame (X_b, Y_b) attached to the hip joint where the leg is attached to the body. Subscript f represents the foot coordinate frame attached to the foot. Its orientation is the same as that of the distal link of the leg. Subscript g represents the

ground coordinate frame attached to a foothold in the ground with an absolute orientation such that Y_g is perpendicular to the ground.

- Three different trajectories are defined: the *unloaded trajectory*, r_u, represents the foot trajectory that is created by the actuators when there are no external forces, such as contact forces. Thus, all $S_i = 0$ for the unloaded trajectory. The *nominal trajectory*, r_n, represents the trajectory of the foot when the robot is under operation with the ideal environment (e.g. running on flat ground or climbing a smooth wall with no disturbances). The *adapted trajectory*, r_a, is the actual foot trajectory under real operation. It deviates a small amount from the *nominal trajectory* due to disturbances from imperfections in the environment or system.

- The jacobian matrix, J, in this chapter relates joint space to ground space, defined in the ground coordinate frame.

2.1.1 Definition of an underactuated compliant system

An underactuated mechanism is defined as a system for which the number of parameters required to determine the entire static state of the system exceeds the number of actuators.

Number of independent actuators: A
Number of parameters to define the static state of the system : P
Fully-actuated system A $\geq$ P
Underactuated system A $<$ P

In other words, an underactuated system still has degrees of freedom with the actuators fixed. Figure 2.1 shows an example of an underactuated leg mechanism. It has three joints: joint 1, joint 2 and joint 3. Each joint angle (or extension in the case of a prismatic joint) is defined by a combination of the actuator input and the deflection of the associated passive element. The leg requires five parameters

$(\theta_1, \theta_3, S_1, S_2, S_3)$ to define its full configuration with respect to contact forces, although it has two actuators. Even if this mechanism had an actuator at joint 2, making every joint actuated, we would still consider it as an underactuated system because the serial compliance at each joint provides an additional degree of freedom. The state of the leg is defined by five parameters; however, the passive degrees of freedom, $S - i$, are coincident with the joints so that the relationship between joint velocities and tip velocity can be written as follows:

$$J \begin{bmatrix} \dot{\theta}_1 + \dot{S}_1 \\ \dot{S}_2 \\ \dot{\theta}_3 + \dot{S}_3 \end{bmatrix} = \begin{bmatrix} \dot{x} \\ \dot{y} \\ \dot{\phi} \end{bmatrix}$$

Because of the compliances, if the actuator positions are fixed, the leg configuration will change when different forces are applied to the tip of the leg. Conversely, it is possible to vary the actuator positions so that the foot position and orientation remain fixed when varying loads are applied to it. For example, the prismatic actuator θ_3 in Figure 2.1 can extend by Δl to account for a compression of the serial compliance, S_3, in response to a force directed along the distal link.

2.1.2 Foot trajectory

Figure 2.2 shows the position vector of the foot in two-dimensional space with respect to the body coordinate frame, denoted by $\vec{r}(t) = [x_r, y_r]$.

The actuator input $\vec{\theta}(t) = [\theta_1, \theta_2, .., \theta_n]$ is a periodic function with period T.

$$\vec{\theta}(t) = \vec{\theta}(t + T)$$

The unloaded position and orientation of the foot are functions of the actuator inputs:

$$[\vec{r}(t), \phi] = F(\vec{\theta}(t))$$

The compliance matrix for the leg is dependent on leg configuration, thus it is function of $\vec{\theta}(t)$.

$$C(\vec{\theta}(t))$$

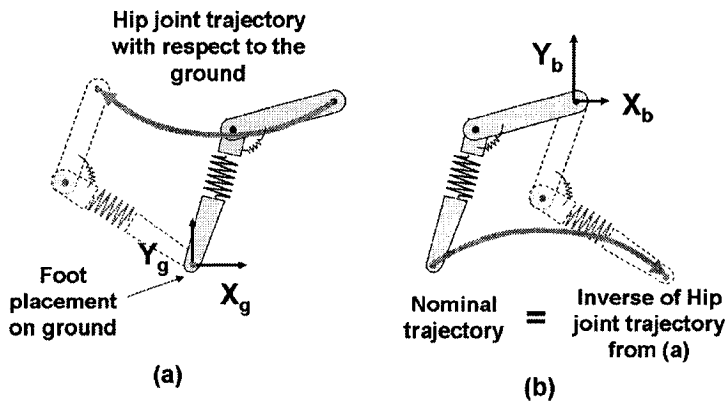

Figure 2.3: (a) Trajectory of hip joint observed in the ground coordinate frame. In the case of a running robot with compliances, the trajectory of the hip joint is usually concave during the stance phase. (b) Correspodning trajectory of the foot in a coordinate frame attached to the hip joint.

Given periodic actuator inputs, the foot follows a periodic trajectory. The position along this trajectory can be parameterized by $(0 < \beta < 2\pi)$ where β is the arc length. Thus,

$$[\vec{r}(t), \phi] = f(\beta)$$

As mentioned earlier, the unloaded foot trajectory describes the motion of the foot without external forces. The robots in operation, however, constantly interact with environment. Compliances in legs undergo deflection in accordance with body dynamics. The foot path deviates from the unloaded trajectory in balance with ground reaction forces, which affect the body motion of the robot. The foot position vector is a function of the sum of actuator inputs and compliant deflections:

$$[\vec{r}(t), \phi] = f\left(\begin{bmatrix} \theta_1(t) + S_1(t) \\ \theta_2(t) + S_2(t) \\ .. \\ .. \\ \theta_i(t) + S_i(t) \end{bmatrix}\right)$$

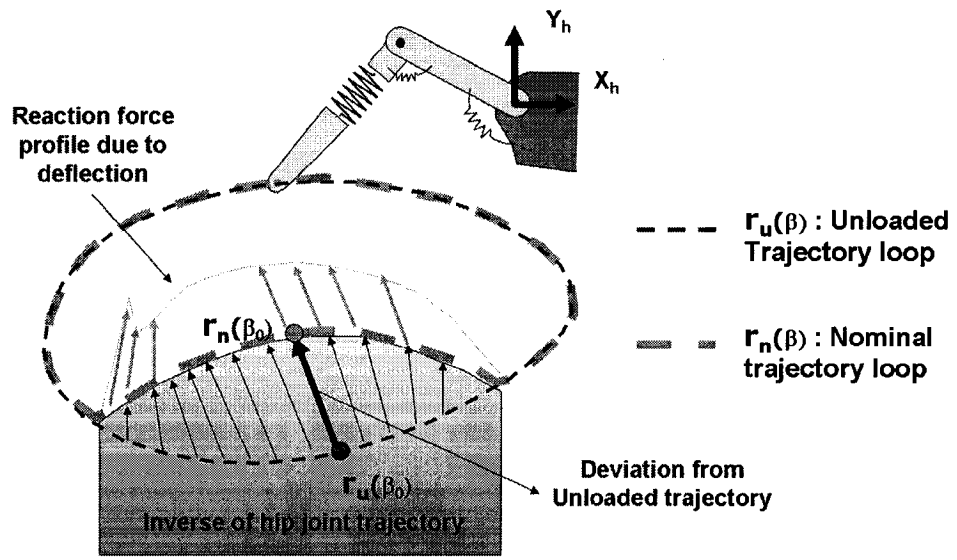

Figure 2.4: Comparison between unloaded and loaded trajectory. When there is no external force on foot, the foot follows the unloaded trajectory. During stance phase, the foot follows the inverse of the hip joint trajectory with a ground reaction force in the body coordinate frame.

Where $S_1, S_2, ..$ are nominal compliant deflections with respect to unloaded state:

$$S_i = jc_i \cdot \tau_i$$

where τ_i is joint torque (or joint force in a prismatic joint) and jc_i is the compliance at the ith joint. Note that the compliance is often substantial, so that the S_i may be comparable to the θ_i.

Under steady conditions, ignoring disturbances, the modified foot trajectory is called the *nominal trajectory*. Because we are assuming steady conditions, this trajectory is also a repeating periodic function and can be described in terms of a single parameter so that we have $r_n(\beta)$.

During stance, the nominal trajectory may differ significantly from the unloaded trajectory. Assuming that the foot makes a point contact with the ground and does not slip, the nominal foot trajectory is approximately the inverse of the hip trajectory with respect to the ground. Thus, the foot position trajectory with respect to the

ground is given by

$$ {}^{g}\vec{r}_b(\beta) + {}^{g}_{b}R(\beta) \cdot {}^{b}\vec{r}_f(\beta) = {}^{g}\vec{(r)}_f $$

where the nominal trajectory of the foot with respect to the hip is ${}^{b}\vec{r}_f(\beta)$ and the hip joint position respect to the ground is ${}^{g}\vec{r}_b(\beta)$. The product ${}^{g}_{b}R(\beta) \cdot {}^{b}\vec{r}_f(\beta)$ represents the position of the foot with respect to the hip, transformed to the ground coordinate system. If the ground coordinate frame is embedded at the foot contact location, and the body does not appreciably pitch or roll, then ${}^{g}\vec{(r)}_f$ should be equal to zero and we can write

$$ {}^{g}\vec{r}_b(\beta) \cong -{}^{b}\vec{r}_f(\beta). $$

For walking robots, the body trajectory with respect to the ground follows a convex curve during the stance phase. For a running robot, the body trajectory with respect to the ground follows a concave shape during the ground phase. Figure 2.3 shows typical body motion in a running robot and the nominal trajectory.

Figure 2.4 shows a typical running robot's nominal trajectory deviating from an unloaded trajectory during the stance phase. During the flight phase, $r_u(\beta) = r_n(\ )$, assuming that the inertial forces due to the leg masses are neglegible. During the ground phase, $r_u(\beta) \neq r_n(\beta)$.

In practice, the robot is subject to perturbations. The adaptive trajectory $r_a(\beta)$ represents the leg trajectory in real operation. It deviates from the nominal trajectory in response to disturbances caused by irregularities in the ground height, inconsistent foot contact, etc. We assume that the deviation from the nominal trajectory is relatively small so that a linear analysis can be applied to the corresponding additional deflections, δS_i.

2.1.3 Compliance matrix

The general normal form of the compliance matrix in robotics is introduced in [83], representing responsive characteristics of the system at a given configuration. The compliance matrix calculation for a robotic gripper is derived by Cutkosky and Kao[38]. The compliance matrices provide useful tools for analysis of the desired

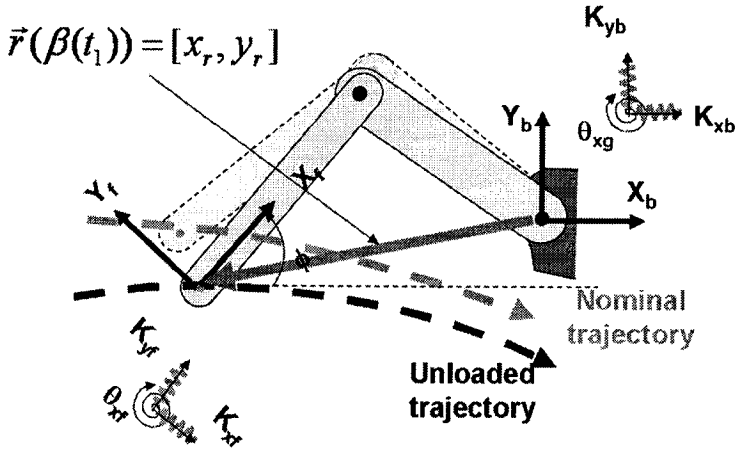

Figure 2.5: Compliance matrix in the body coordinate frame and in the foot coordinate frame

grasp force and stability of a hand. Compliance matrices in different coordinate systems can be related to each other in terms of the Jacobian matrix[38] provided that the deflections are small. The derivations of compliance matrices for a leg follows the procedure presented in the literature [38].

Because compliances are lumped at the joints, the compliance matrices are diagonal in joint space:

$$C_j = dia(jc_1, jc_2, ...jc_n)$$

A joint torque vector τ causes deflection in the joint compliance vector S=[S_1 S_2 ...S_n]^T,

$$C_j\tau = S.$$

As noted earlier, the nominal loaded trajectory may deviate significantly from the unloaded trajectory, in which case the torques and forces at the joints must be calculated accounting for the deflected configuration of the limb. Focusing on the nominal trajectory, small relative motions of the joints produce small displacements

of the foot with respect to the nominal trajectory:

$$J\delta q = \delta X$$

where $J(\beta)$ is the (configuration dependent) Jacobian matrix. Conversely, the forces at the joints are related to those at the tip as:

$$\delta\tau = J^T \delta F$$

where $\delta\tau = [\ \delta\tau_1\ \delta\tau_2\ ....\ \delta\tau_n]^T$.

Given the definition of a compliance matrix we can write

$$\begin{aligned} \delta S = C_j \delta\tau = C_j J^T \delta F \\ J\delta S = J C_j J^T \delta F \\ \delta X = J C_j J^T \delta F. \end{aligned}$$

By inspection of the equation above, we see that the compliance matrix in the work space of the foot is

$$C = J C_j J^T \tag{2.1}$$

where

$$C = \begin{bmatrix} c_{xx} & c_{xy} & c_{x\theta} \\ c_{xy} & c_{yy} & c_{y\phi} \\ c_{x\phi} & c_{y\phi} & c_{\phi\phi} \end{bmatrix}$$

.

Figure 2.5 shows the compliance matrix in the body frame and the equivalent compliance matrix in the foot coordinate frame, ${}^bC$ and ${}^fC$ respectively. The relationship the between two frames is described by vector $r(\beta) = [x_r, x_r, \phi]$, which gives the position and orientation of the foot coordinate frame with respect to body. A cartesian coordinate transformation matrix R [37] for this planar case is:

$$R = \begin{bmatrix} cos(\phi) & sin(\phi) & x_r \cdot sin(\phi) - y_r \cdot cos(\phi) \\ -sin(\phi) & cos(\phi) & x_r \cdot cos(\phi) + y_r \cdot sin(\phi) \\ 0 & 0 & 1 \end{bmatrix} \tag{2.2}$$

Transforming compliances between frames

Velocities and small motions can be transformed between frames as $V_f = {}^f_b R \cdot V_b$ and $\delta X_f = {}^f_b R \cdot \delta X_b$, respectively. As a reciprocal relationship, it can be shown through the conservation of virtual work that $F_b = R^T \cdot F_f$. Combining these relationships we have:

$$\begin{aligned} \delta X_f = {}^f_b R \cdot \delta X_b &= {}^f_b R \cdot (C_b \cdot \delta F_b) \\ &= {}^f_b R \cdot C_b \cdot ({}^f_b R^T \delta F_f) \\ &= C_f \cdot \delta F_f \end{aligned} \tag{2.3}$$

or

$$C_f = {}^f_b R \cdot C_b \cdot {}^f_b R^T \tag{2.4}$$

2.1.4 Compliance Superposition

Compliance superposition is useful for design of an underactuated leg. One reason for using compliances instead of stiffnesses is that compliances add in series along a serial kinematic chain. Figure 2.6 shows how each compliance adds up to the total compliance. Where there are springs in parallel, the effective compliance of each element is calculated by temporarily fixing the other compliances to be zero. If other compliant elements are fixed, the system has only one degree of freedom and the compliance matrix element is easily calculated. This method is valid only when the design of interest is a statically determinate system.

An leg example is depicted in Figure 2.7. Following our procedure, the foot compliance matrix is

$$C = JC_jJ^T$$

where,

$$C_j = dia(jc_1, jc_2, jc_3, ...jc_n)$$

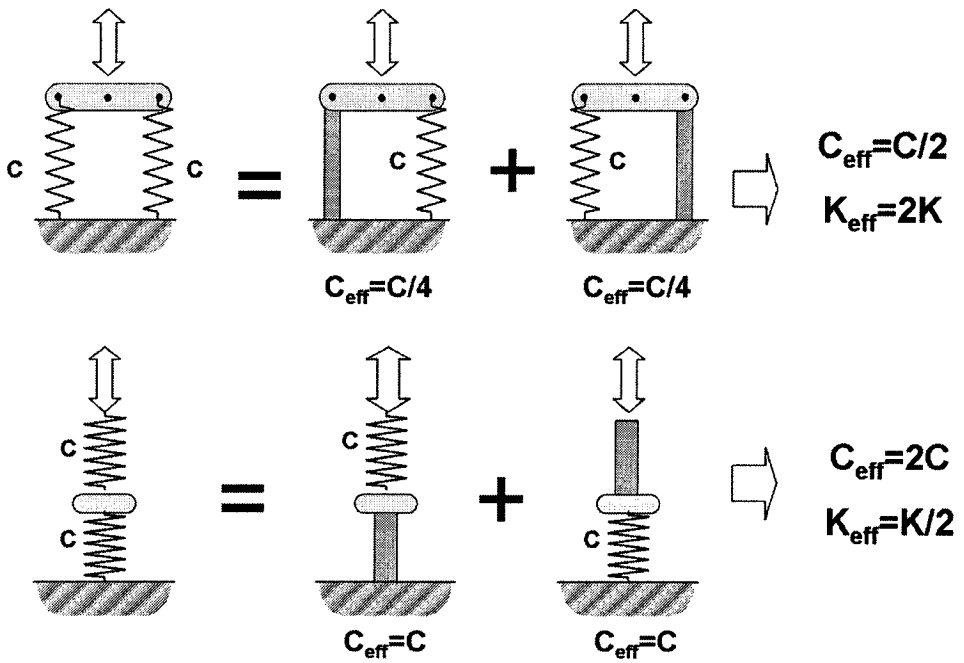

Figure 2.6: Compliance calculation for combination of springs, by superposition.

To compute the compliance matrix for joint 1, other jc_i are temporarily set to zero:

$$C_{j1} = dia(jc_1, 0, 0, ...0)$$

$$C_1 = JC_{j1}J^T.$$

For each joint, C_{j1},C_{j2},C_{j3},C_{j4}...C_{jn} exist. We assume there are no freely pivoting joints, so C_ji is never infinite (in other words, the leg always returns to an equilibrium configuration in the unloaded state). However, it is possible for some joint that $C_ji = 0$, which causes no numerical difficulties. The total compliance matrix is

$$\begin{aligned} C &= C_1 + C_2 + C_3 + ... + C_n \\ &= JC_{j1}J^T + JC_{j2}J^T + JC_{j3}J^T + ... + JC_{jn}J^T \\ &= J(C_{j1} + C_{j2} + C_{j3} + .. + C_{jn})J^T \\ &= JC_jJ^T. \end{aligned} \tag{2.5}$$

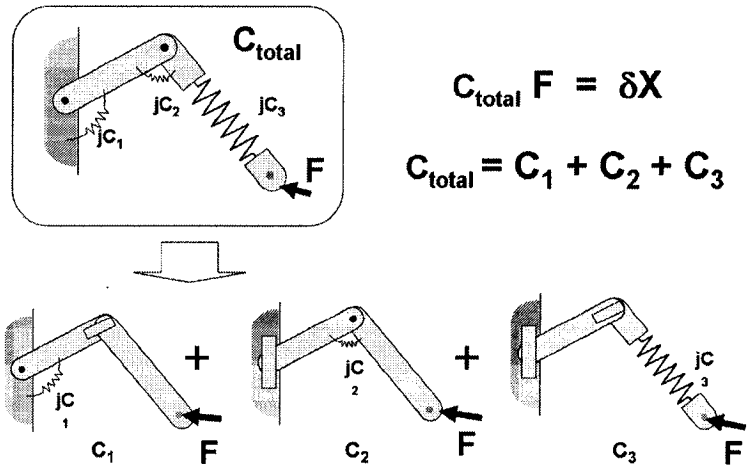

Figure 2.7: Compliance superposition in 2-D linkages

2.1.5 Design procedure of compliant mechanisms in bio-inspired robots

In this section, we introduce the compliant leg design procedure, following the notation just introduced and using the design of a compliant leg for *iSprawl* as an illustrative example.

For the leg compliance design, a simple procedure is introduced:

1. Identify desired behaviors of the designated mechanism.
2. Identify desired norminal trajectory to acheive desired behaviors.
3. Specify compliance matrices for one or more points of interest along the trajectory.

Figure 2.8 shows an example of a compliant mechanism applied on the running robot, iSprawl. It has two kinematic degrees of freedom which correspond respectively to hip rotation (S_1) and a prismatic joint (θ_2, S_2) along the leg. The hip joint has a rotational spring with compliance, jc_1, and the prismatic joint has a linear compliance, jc_2, in series with the actuation.

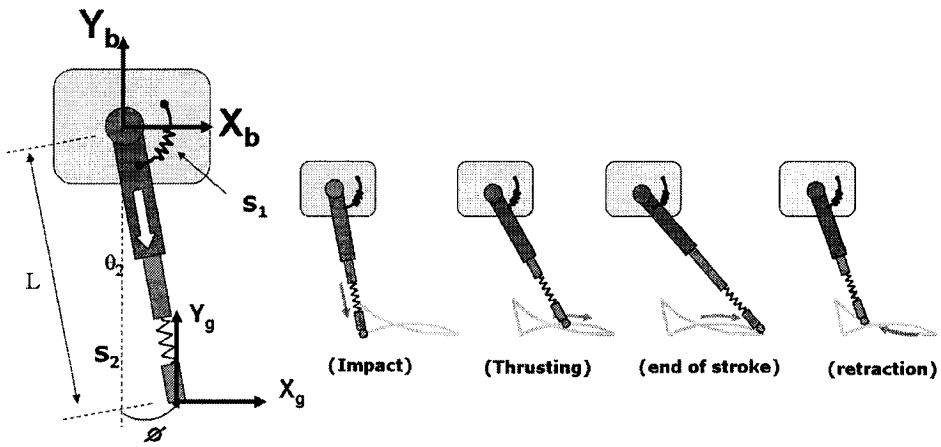

Figure 2.8: (left)Schematics of iSprawl leg. Rotational hip joint is passive and prismatic joint is actuated with serial axial compliance. (right) Sequence of the leg movement.

The desired behavior is not simply defined by mimicking the natural model. The simplified robot model lacks many features of the animal and therefore its mechanical requirements may be different. In the case of *iSprawl*, a desired behavior is to create a smooth body trajectory. The behavior of the center of mass represents a large portion of the overall behavior. The trajectory of the center of mass contains information about the transformations between gravity, kinetic and elastic energy. My operating hypothesis for iSprawl was that a smooth trajectory of the center of mass results in smaller accelerations in the vertical direction during the stance phase, since the acceleration is the second derivative of the position curve. The smaller the acceleration, the smaller the vertical force and the less the frictional losses throughout the power transmission path. In addition, the center of mass trajectory of any legged robot should follow a certain periodic curve, which can be expressed by a Fourier series. To minimize acceleration, the curve should have low magnitudes for any high frequency term in the Fourier expression. Ideally, for minimum acceleration, the center of mass trajectory needs to follow a smooth sine wave matching with stride frequency.

As shown in Figure 2.3, the desired nominal trajectory is obtained from the body trajectory. The desired nominal trajectory of the foot during stance phase is a sine

wave, smoothly continuing from the end of the parabolic curve associated with the flight phase. (The flight phase is the phase between the stance phases of the two tripods. In practice, *iSprawl* drags its rear legs slightly so that it never becomes fully airborne.)

To specify the compliances along the desired trajectory, the compliance matrix is calculated. If the Jacobian matrix is known, we can simply calculate the compliance matrices. In this simple example, the Jacobian matrix and compliance matrices for iSprawl are:

$$J = \begin{bmatrix} Lcos\phi & sin\phi \\ Lsin\phi & -cos\phi \\ 1 & 0 \end{bmatrix}$$

$$C_j = \begin{bmatrix} jc_1 & 0 \\ 0 & jc_2 \end{bmatrix}.$$

The compliance matrix in the work (ground) space is therefore:

$$C = JC_jJ^T$$

$$C = \begin{bmatrix} jc_1L^2(cos\phi)^2 + jc_2(sin\phi)^2 & -jc_1L^2cos\phi sin\phi - jc_2sin\phi cos\phi & jc_1Lcos\phi \\ -jc_1L^2cos\phi sin\phi - jc_2sin\phi cos\phi & jc_1L^2(sin\phi)^2 + jc_2(cos\phi)^2 & -jc_1Lsin\phi \\ jc_1Lcos\phi & -jc_1Lsin\phi & jc_1 \end{bmatrix}.$$

At impact, as the leg angle, ϕ, is close to 90 degrees, the compliance in the vertical direction, $(C_{yy} = jc_1L^2(sin\phi)^2 + jc_2(cos\phi)^2)$, is dominated by the compliance in the cable, jc_2, as shown in matrix above. In mid stance, the vertical compliance is a combination of the rotational and prismatic compliances. At the end of stroke, the axial compliance contributes little and the rotational compliance dominates the vertical compliance as the $cos\phi$ term becomes small. The compliance matrix in the body coordinate frame is dependent upon the leg configuration, which changes over the stride as the Jacobian varies with leg angle.

We can obtain useful information from the compliance matrix in the work space. However, for best performance, the process requires iterative tuning to adjust the compliances in the joint space. The additional analysis is introduced in Chapter 3.

2.2 Differential system

A differential system is a particular class of underactuated mechanism that is used in applications such as the differential drive of an automobile, or a rocker-bogie suspension, to distribute the force or torque. Since it automatically distributes the force mechanically, it requires no sensory feedback and accordingly has no control delay. A rocker-bogie design enables a wheeled robot to traverse rough terrain[112]. Figure 2.9 shows a schematic drawing of a rocker-bogie linkage and an equivalent hydraulic system. A compound differential system can couple more than two degrees of freedom through one actuator. In most cases, the sum of displacements of the subordinate degrees of freedom equals the displacement of the upper level degree of freedom. In the case of a bio-inspired robot, the extra unactuated degrees of freedom in a differential allow it to adapt to the environment.

$$D_{upperDOF} = a_1 \times d_{DOF1} + a_2 \times d_{DOF2} + ... + a_n \times d_{DOFn}$$

The equation above shows how the subordinate systems share the displacement, where a_1,a_2,..a_n are determined by the geometry of the design.

One disadvantage of differential systems is the uncertainty of position when there is no reaction force on both ends. For example,when there is no interaction between the system and environment. In order to compensate for this drawback, return springs are often used to maintain a default position, somewhat compromising the force distribution as shown in Figure 2.9(C).

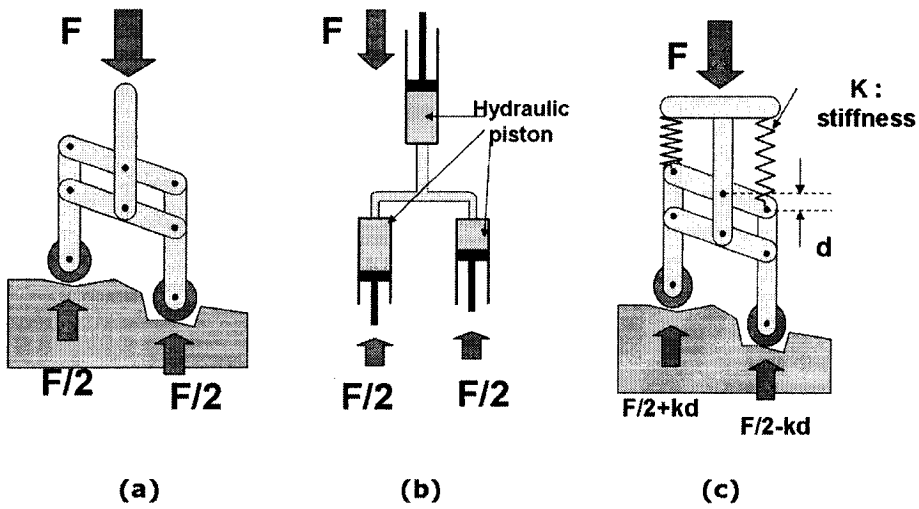

Figure 2.9: Rocker-bogie linkage system and hydraulic differential

Chapter 3

iSprawl: running with passive dynamics

This chapter describes the design features that underlie the operation of *iSprawl*, a small (0.3 Kg) autonomous, bio-inspired hexapod that runs at 15 body-lengths/second (2.3 m/s). These features include a tuned set of leg compliances for efficient running and a light and flexible power transmission system. This transmission system permits high speed rotary power to be converted to periodic thrusting and distributed to the tips of the rapidly swinging legs. The specific resistance of iSprawl is approximately constant at 1.75 for speeds between 1.25 m/s and 2.5 m/s. Examination of the trajectory of the center of mass and the ground reaction forces for *iSprawl* show that it achieves a stable, bouncing locomotion similar to that seen in insects and in previous (slower) bio-inspired robots, but with an unusually high stride frequency for its size.

3.1 Introduction

In recent years a number of robots have been developed that draw their inspiration from running arthropods or insects including *Sprawlita* [30], *Scorpion* [76], *Whegs*

[103] *Mini-Whegs* [95] and *RHex* [108]. When insects are moving rapidly they typically employ an alternating tripod gait and rely heavily on passive mechanical properties to achieve dynamic stability. The sprawled posture with large forces in the horizontal plane, and the compliance and damping in the limbs and joints, serve as "preflexes" [82] that promote stable running and rapid recovery from perturbations [77, 89].

In the case of the *Sprawl* family of robots, the main principles adapted from insects, the cockroach in particular, are:

- a bouncing, alternating tripod gait based on a substantially feed-forward motor pattern [53],
- limb specialization in which the rear legs primarily accelerate the body while the front legs decelerate it [49],
- legs that generate ground reaction forces directed from the feet through the hips [49],
- "hip" joints with significant passive rotational stiffness and damping that help stabilize the gait and recirculate the legs during the swing phase [56, 90, 77].

The *Sprawl* robots are fabricated using a multi-material rapid prototyping process, Shape Deposition Manufacturing [30, 120], that makes it possible to achieve local variations in structural compliance and damping and to embed components such as sensors and actuators for increased ruggedness. Like their exemplars, the *Sprawl* robots are capable of fast locomotion over rough terrain and of executing rapid turns by changing leg thrust angles [85].

The robots can run without any proprioceptive or exteroceptive feedback; however, the addition of ground contact sensors allows the stride period to adapt automatically to changes in terrain or slope [32] and the addition of antennae allows the robots to follow walls at running speeds [36]. A closer look at the dynamics of the running robots reveals motions and ground reaction forces similar to those found in insects and other small animals. This locomotion pattern has been termed SLIP (spring loaded inverted pendulum) in the literature and is seen in many running animals [51].

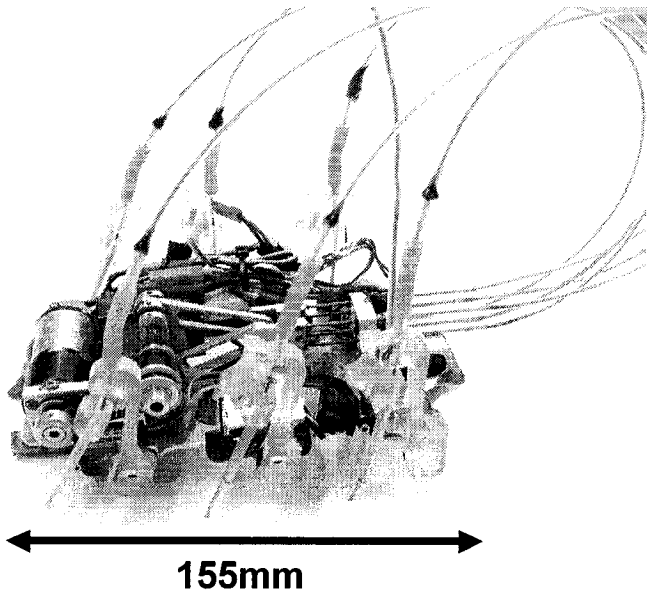

Figure 3.1: *iSprawl*: a fully autonomous hexapedal robot driven by an electric motor and flexible push-pull cables.

A limiting factor in the design of the previous *Sprawl* robots has been their use of pneumatic pistons for propulsion. Although electric motors are ubiquitous in small robots, pistons were chosen for the *Sprawl* robots as powerful, compact linear actuators. The main disadvantage to pneumatic pistons is that they virtually preclude autonomous operation. The volume of compressed gas needed for 10 minutes of operation is such that a gas storage tank would be too heavy to carry on board. Clearly this is a problem since for practical application legged robots need to be power autonomous.

In this chapter, we examine an independent version of the *Sprawl* robots utilizing electric propulsion. The incorporation of a new power transmission system, lithium polymer batteries, and a redesigned set of complaint legs have enabled *iSprawl* to run autonomously at speeds of over 15 body-lengths/second (2.3 m/s). Despite significant changes in the actuation and force generation mechanism, we show that by appropriately tuning the passive compliance in the legs the fast, self-stabilizing behavior of the robot is preserved. This invariance to actuation scheme underscores the generality of the locomotion principles encapsulated in the *Sprawl* family of robots.

3.2 Mechanical Design of *iSprawl*

The most challenging aspects of utilizing electrical actuation for the *Sprawl* robots are converting continuous rotation to periodic thrusting and incorporating sufficient flexibility into the power train to accommodate the repositioning of the legs. Several schemes were investigated before settling on the system presented in this chapter.

One major concern is power density, for which it is desirable to use a single high-speed electric motor as the primary actuation source. For large robots, the actuator energy can be stored elastically and periodically released, as in the case of the Bow Legged Hopper [26] and a number of subsequent legged robots (e.g. [96]). At the scale of *iSprawl* however, it becomes easier to store kinetic energy. This is the approach shown in Figure 3.2, in which a rotating double crank-slider mechanism stores rotational kinetic energy and converts it to alternating push-pull motions for each tripod of legs. As discussed in Appendix A.1, the total rotational kinetic energy

is approximately equal to the power consumed per stride while running.

The push-pull actions must also be distributed to the tips of the flexible, swinging legs. One possible solution is to employ liquid using a master/slave piston arrangement and flexible tubes. An early variant named "Aquasprawl" employed this method and achieved speeds of 3 body-lengths/second. A lighter and more efficient alternative is to use flexible cables in low-friction sleeves, as shown in Figure 3.3. By adding rigid elements to both ends of the shaft and tube, the cables are able to thrust as well as pull. The end result is that the legs of *iSprawl* have a very low rotational inertia and a passive swing frequency of 45 Hz.

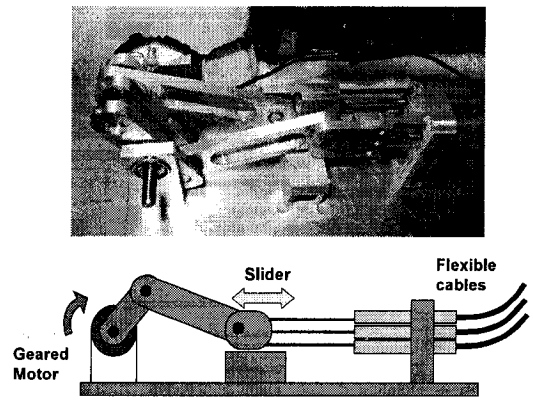

Figure 3.2: Power transmission system for *iSprawl*. A double crank-slider is used to store and convert the rotational energy from the motor to linear oscillations.

As in previous *Sprawl* robots, iSprawl incorporates underactuated leg mechanisms. The motions of the legs back and forth with each step are achieved passively by operating the robot as a resonant system. During each stance phase the hip springs (flexures) are loaded by the motion of the body. During the swing phase this stored energy is used to reposition the legs to their nominal orientation. In addition, remote control servos are mounted at the hips of the middle legs to change the equilibrium leg angles to effect turns, as motivated by the results of [85]. The physical specifications

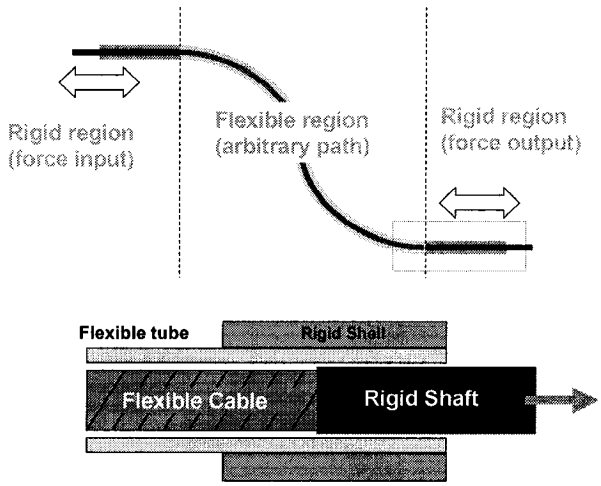

Figure 3.3: Power transmission system for *iSprawl*. Schematic sketch shows the flexible and rigid sections of the push-pull cables.

for *iSprawl* are given in table 3.1.

3.2.1 Leg trajectory

As seen in Figure 3.4, the nominal foot trajectory significantly differs from the unloaded trajectory, which is a straight line with respect to the (rotating) hip coordinate frame. As described in the previous section, iSprawl's underactuated leg design incorporates a single actuated degree of freedom and a passive rotational visco-elastic hip joint. Compliance in the direction of thrusting is dependent on the extension of a rubber tube that is spliced into the flexible sleeve that guides the push-pull cable. Rotational compliance is realized in the flexure of the SDM leg. For better performance of the robot, the compliance needs to be tuned properly because it affects the body dynamics and causes variations in ground reaction forces. Tuning of the compliance is described in the next section.

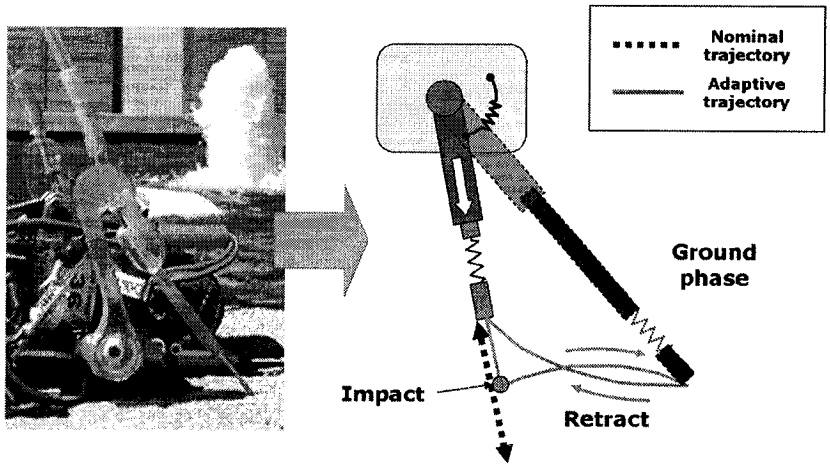

Figure 3.4: Schematic of the leg design of iSprawl shows the unloaded trajectory and nominal loaded trajectory of the foot. Flexible polymeric joints provide rotational compliance. Axial compliance is realized with a rubber tube in the sleeve that guides the cable, as shown in Figure 3.5

Table 3.1: Physical Parameters for *iSprawl*

Body size	155 x 116 x 70 mm (excluding cables)
Body mass	0.3 kg (including batteries and servo circuit)
Maximum speed	2.3 m/s (15 bodylength/s)
Stride frequency	14 Hz
Power consumption	12 W
Motor	Maxon A-max series, 6Watt; 22 mm dia.
	Rated voltage : 6V (actual = 22V)
	Rated torque : 7.36mNm at 6V
	Rated current : 756 mA at 6V
	Actual speed : 21384 rpm at 22V
Gear head	19.8:1, Maxon ϕ24 spur gear
Timing belt	3.2 mm wide, 9:7 speed ratio
Legs	Polyurethane 72DC and 90A
	from Innovative Polymers Inc.
Servo motors	Hitech H5-55 (1.3 Kg cm)
Typical leg motion	25 mm stroke, 25° swing
Battery	6 pack lithium polymer
	(3.7 $\times$ 6 V, 250 mAh per pack)
Battery life	approx. 5 min. at running speed

3.3 Tuning Parameters for Smooth Open-Loop Running

When first assembled, *iSprawl* achieved speeds of approximately 5 body-lengths/second. Review of high-speed video of its motion on a treadmill revealed numerous sources of inefficiency, including excessive and irregular pitch and roll oscillations and bouncing and slippage of the feet. These effects were gradually reduced by adjusting the center of mass location and the equilibrium angles of the front, middle and rear legs following a procedure similar to that of [34]. At this point it became clear that foot contact forces were increasing too rapidly after initial contact, causing abrupt changes to the momentum of the robot and reducing efficiency. The effect is not surprising given that we have replaced a compliant force actuator (pneumatics) with a fixed displacement actuation from the slider-crank mechanism. To achieve a smoother, more SLIP-like

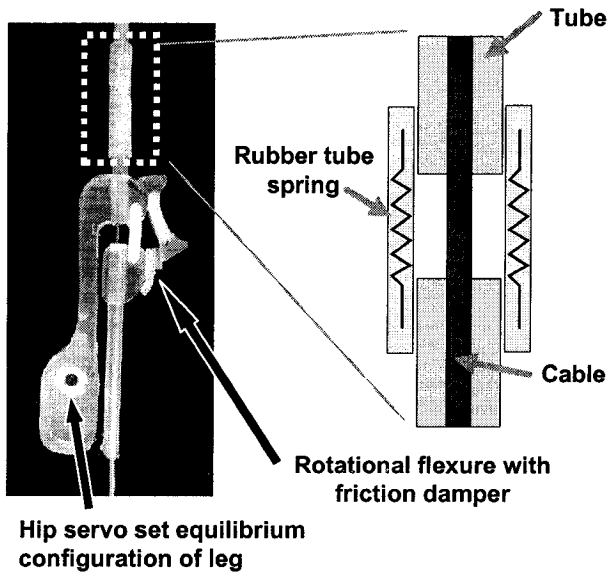

Figure 3.5: Schematic of the leg compression spring design utilizing a tension spring in the flexible sleeve around the push-pull cable. Also shown are the frictional dampers (on front and middle legs).

motion, it was necessary to add tuned axial compliance to the push/pull cables, as shown in Figure 3.5.

3.3.1 Desired Leg Extension Profile

The hypothesis used in tuning the axial leg compliances is that the ideal motion of the robot is a smooth low-amplitude oscillation in the vertical plane and a nearly constant forward velocity, as indicated in Figure 3.6. The constants used in these calculations are listed in Table 3.2. As described in the example in Chapter 2, the desired behavior is to achieve a smooth center of mass trajectory, approximating a gentle sinusoidal curve. The desired leg trajectory is easily achieved by inverting the desired body trajectory. Since the forward velocity is assumed to be contant, instead of comparing desired trajectories, we can use the desired leg extension profile in a rotating reference frame.

Table 3.2: Parameters for Single Analytic Leg Model in Figure 3.6

θ_i	70°	Leg initial angle
θ_f	45°	Leg final angle
f	$14\,Hz$	Leg oscillation frequency
v	$2.3\,m/s$	Body forward velocity
h_{nom}	$35\,mm$	Nominal body height
Δh	$1\,mm$	Change in body height

We begin by assuming that the height, h, of the body follows a sinusoidal path:

$$h(t) = h_{nom} + \Delta h \; sin(2\pi \; 2f \; t) \tag{3.1}$$

where h_{nom} is the nominal body height, Δh is amplitude of oscillation, and $2f$ is the body oscillation frequency (the body's vertical oscillation frequency is twice the leg actuation frequency). The initial leg length, L_0, is given by:

$$L_0 = h_{nom}/sin(\theta_i) \tag{3.2}$$

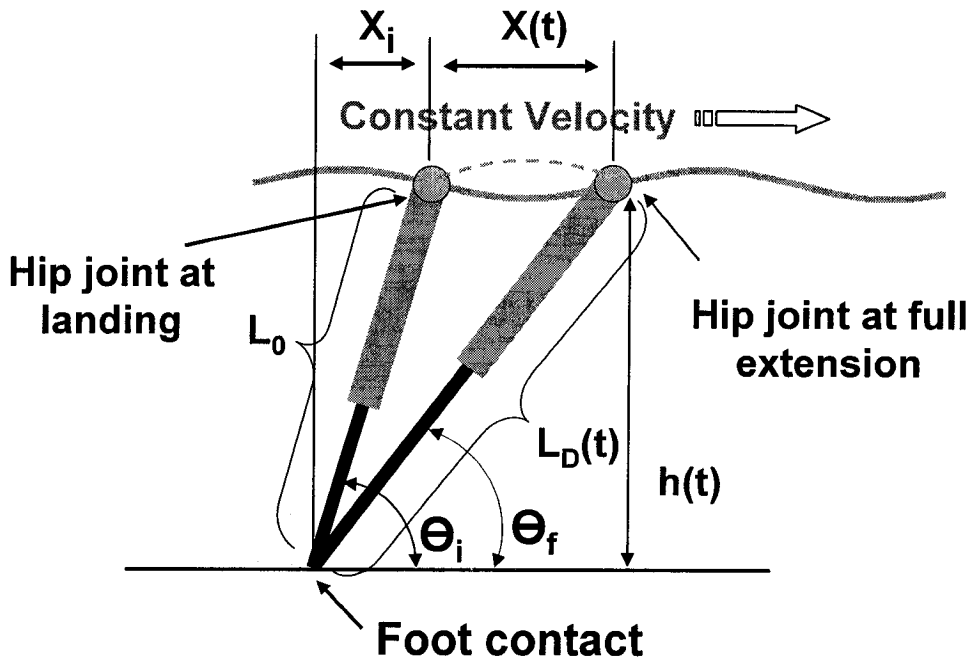

Figure 3.6: Schematic of the desired leg extension profile needed to produce a sinusoidal trajectory of the center of mass during stance. Dashed line shows trajectory that would occur without compression assuming that the foot stays in contact to the ground based only on a kinematic relationship. (In practice, the body trajectory will not exactly follow this kinematic approximation. In particular, the transition between the end of the dotted curve and the solid curve would not be as abrupt.)

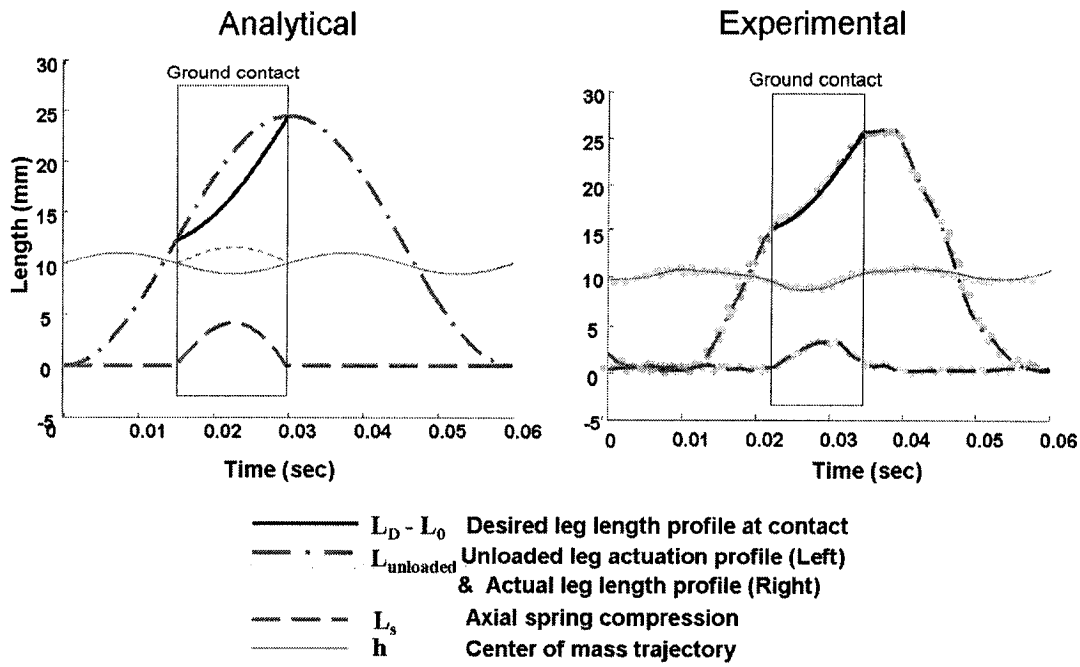

Figure 3.7: The theoretical and experimental leg extension profiles for *iSprawl* running at 2.3 m/s. Also shown are the path of the COM and the extension of the axial spring for each case. The dashed line in the analytical plot shows COM trajectory that would occur without any spring compression. Curves for the measured leg extension and COM trajectory represent averages of three successive strides shown in gray dots.

where θ_i is the leg angle at touchdown. The horizontal position of the body at touchdown is given by:

$$X_i = L_0 cos(\theta_i) \tag{3.3}$$

and the forward position as a function of time is given by:

$$X(t) = v\, t \tag{3.4}$$

which assumes a constant horizontal velocity, v. (This is a reasonable assumption as the actual forward speed varies by less than 3 percent over a stride.)

For the leg to remain in contact, the desired leg length, $L_D(t)$, is given by:

$$L_D(t) = \sqrt{h(t)^2 + (x_i + x(t))^2}. \tag{3.5}$$

For *iSprawl* the unloaded leg extension trajectory, $L_{unloaded}(t)$, which is a function of the crank-slider mechanism (see Appendix A.1 for details) can be approximated as:

$$L_{unloaded}(t) = A_0\ sin(2\pi f t) + L_0 \tag{3.6}$$

where $A_0 = 12.7\,mm$. The leg compression, L_s, is given by:

$$L_s(t) = L_0 + L_{unloaded}(t) - L_D(t). \tag{3.7}$$

The solution of these equations yields the maximum leg spring compression during stance $\Delta L = max(L_s(t)) = 4\,mm$.

The body oscillates vertically at a frequency of $2f = 28\,Hz$, leading to a peak vertical acceleration of:

$$\ddot{h}_{max} = \Delta h(2\pi\ 2f)^2 \tag{3.8}$$

and a maximum vertical ground reaction force of:

$$F_{h,max} = mg + m\Delta h(4\pi f)^2 \tag{3.9}$$

With a body mass, m, of 0.31 kg the maximum predicted force, $F_{h,max}$, is 12.2 N, which correlates well with the peak measured ground reaction forces found in section 3.3.4. The peak force occurs at a leg angle, θ, of approximately 55°, about half way through stance. Although the leg is not a free pin joint due to rotational hip compliance, we assume that the force is acting primarily along the axis of the leg.

Thus the effective whole body leg spring constant should be:

$$k = \frac{12.2\,N/\sin(55°)}{4\,mm} = 3.7\,N/mm. \tag{3.10}$$

The front legs have the largest contribution (roughly 50%) to the vertical stiffness of the tripod. Accordingly, springs with a stiffness of 1.7 N/mm inserted into the legs were found to give best performance. Note that to achieve the effect of a compression spring in series with the push-pull cables, it was actually easier to insert a corresponding tension element (a short section of latex rubber tubing) into the otherwise inextensible sheaths (Figure 3.5).

Figure 3.7 shows the theoretical and the measured leg and body trajectories for a single stride. The trajectories for the measured case were obtained by filming *iSprawl* at 500 frames/second as it ran on a treadmill. The estimated positional accuracy is ± 0.1 mm. The dark lines represent the desired leg extension profile during contact, and the thin lines represent the trajectory of the center of mass. The dashed segment of this line in the analytical plot indicates the center of mass trajectory that would occur without the leg spring, whose compression is indicated by the dashed line at the bottom of the plot. The experimental data show that both the leg extension and center of mass trajectories match the model predictions closely. The experimentally measured axial spring compression is slightly smaller than the predicted value. This is compensated for by the inherent elasticity of the push-pull cable system. We note that the actual ground contact is slightly delayed with respect to the predicted value due to some backlash in the transmission system.

Adding axial compliance to the legs increased the robot's speed by 50%. It also reduced mechanical failures and produced a smoother period-1 gait.

In addition to tuning the axial compliance of the leg extension system, it was necessary to adjust the rotational compliance and damping of the passive hips. As

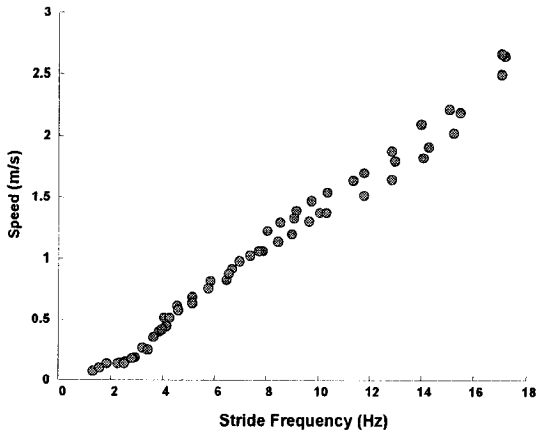

Figure 3.8: Running speed of *iSprawl* vs. stride frequency

with the earlier *iSprawl* robots, the legs are multi-material structures of hard and soft urethane. If the urethane flexures are too stiff, the legs do not flex enough and the stride length is reduced; if they are too soft the robot stumbles and loses open-loop stability [34]. Empirically, rotational stiffnesses of approximately 72 Nmm for the front legs, 54 Nmm for the middle, and 36 Nmm for the rear legs were found to give best results. In earlier *Sprawl* robots, the inherent visco-elasticity of the soft urethane provided adequate damping; for *iSprawl* it was necessary to add small friction dampers to the front and middle legs, as can be seen in Figure 3.5.

3.3.2 Performance

Figure 3.8 shows the relationship between the robot's forward velocity and its stride period. The normal operation point for the robot is at 14–15 Hz, which corresponds to a speed of about 2.3 m/s. The relationship between forward speed and actuation frequency is nearly linear above 4 Hz, with no perceptible change in the motion pattern.

Another value that has been used to measure locomotion speed in a scale independent manner is the Froude number, F, a dimensionless value that relates the inertial force to gravitational force or alternatively the translational kinetic energy to the gravitational potential energy of the system. The Froude number is typically defined as[1]:

$$F = \frac{v^2}{gl}$$

where v is the velocity of locomotion, g is the gravitational constant, and l is a characteristic leg length, often taken in running robots as the distance from the hip to the ground. Alexander and Jayes [6] have shown that a wide variety of animals transition their gait from a walk to a trot at Froude number of 0.3 to 0.5 and a trot to a gallop between 2 and 3. *iSprawl* exhibits a gait transition from walking to running (as defined by the phasing of its kinetic and gravitational potential energy) at about 3.5 Hz and Froude number of 0.36. When running at its nominal frequency of 14 Hz, it has a Froude number about 10.8.

iSprawl's top speed of 2.3 m/s is about 15% slower than the current fastest autonomous hexapedal runner *RHex*, but as *iSprawl* is only about 1/3 as long, its speed relative to size (body-lengths/second) is much larger. The performance of *iSprawl* is the same whether running on a treadmill or on paved surfaces. It easily traverses obstacles less than 2 cm high. In soft terrain, the robot becomes mired due to its small feet. Perhaps a better comparison would be to *Mini-Whegs* [95], which at 0.09 m long and 0.150 kg is a little more than half the size of *iSprawl*. *Mini-Whegs* uses rimless "wheel-legs" as its appendages, which enable it to climb over relatively larger obstacles, but it runs at a slower relative speed. In addition, the thrusting legs of *iSprawl* allow it to make more rapid turns (turn radius of 1.5 vs. 2.5 body-lengths for *Mini-Whegs*) at speeds below 1 m/s.

[1]The original Froude number, in hydrodynamics, is defined as $F = v/\sqrt{gl}$, but this form is used in biomechanics literature

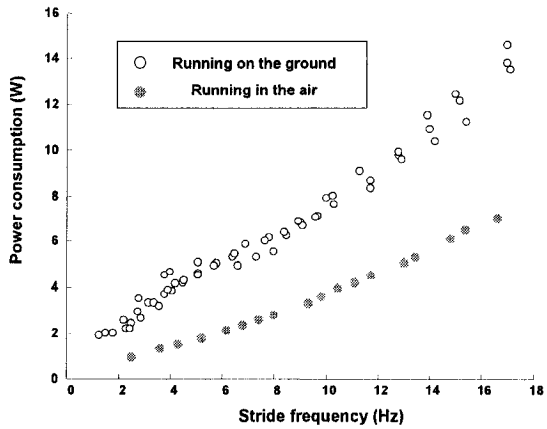

Figure 3.9: Electrical power consumption of *iSprawl* without load and with running load.

3.3.3 Energetics

Since the power supply contributes a relatively significant portion of total mass, energy efficiency is of crucial importance for autonomous legged robots. With the switch from a pneumatic to an electro-mechanical actuation scheme, a significant energetic improvement is realized. Furthermore the precise measurement of the total power consumption is straightforward.

Figure 3.9 shows the total power consumption while running on a treadmill and the non-productive power consumption (i.e., while running in air) as a function of stride frequency. The latter data set should be taken as a lower bound because the transmission forces, and the corresponding friction forces, are higher when the robot is in contact with the ground.

When driven at low frequencies *iSprawl's* power consumption has a larger relative variation since the required motor torque fluctuates throughout the stride. Beyond 5 Hz, the robot runs with a stable gait and a constant power consumption which is linearly proportional to stride frequency. At its top speed *iSprawl* has enough battery

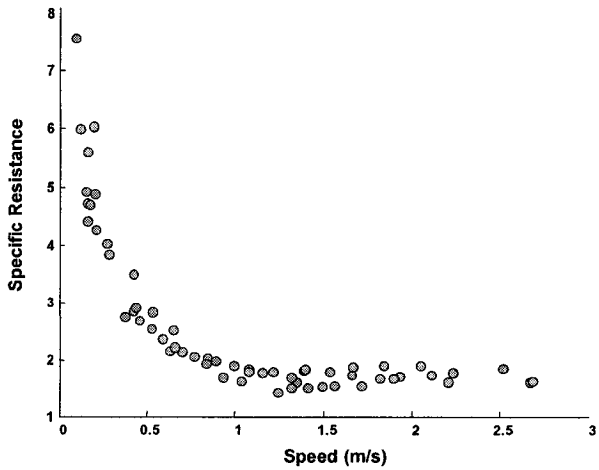

Figure 3.10: Specific resistance vs. speed for *iSprawl* running on smooth terrain.

life to run continuously for about 5 minutes.

For comparison with other legged robots, Figure 3.10 shows the specific resistance, $P(v)/mgv$, as a function of speed, where m is the mass of the robot, v is the forward velocity and $P(v)$ is the total electrical power consumption. For the preferred running speeds of *iSprawl*, corresponding to stride frequencies above 7 Hz and speeds above 1 m/s, the specific resistance is nearly constant at 1.75. This value is comparable to that of other running robots, although higher than the most efficient of them [100, 119]. Looking again at Figure 3.9, we observe that half the total power is consumed in the motor and transmission system, which suggests that specific resistance could be improved with a more efficient motor and gearbox and with an effort to reduce the sliding friction in the cables.

3.3.4 Ground Reaction Forces

A final subject of comparison among *iSprawl*, the earlier *Sprawl* robots, and insects is the pattern of ground reaction forces (GRF). The pattern seen in insects is that the front legs provide a braking force at the start of each step while the rear legs

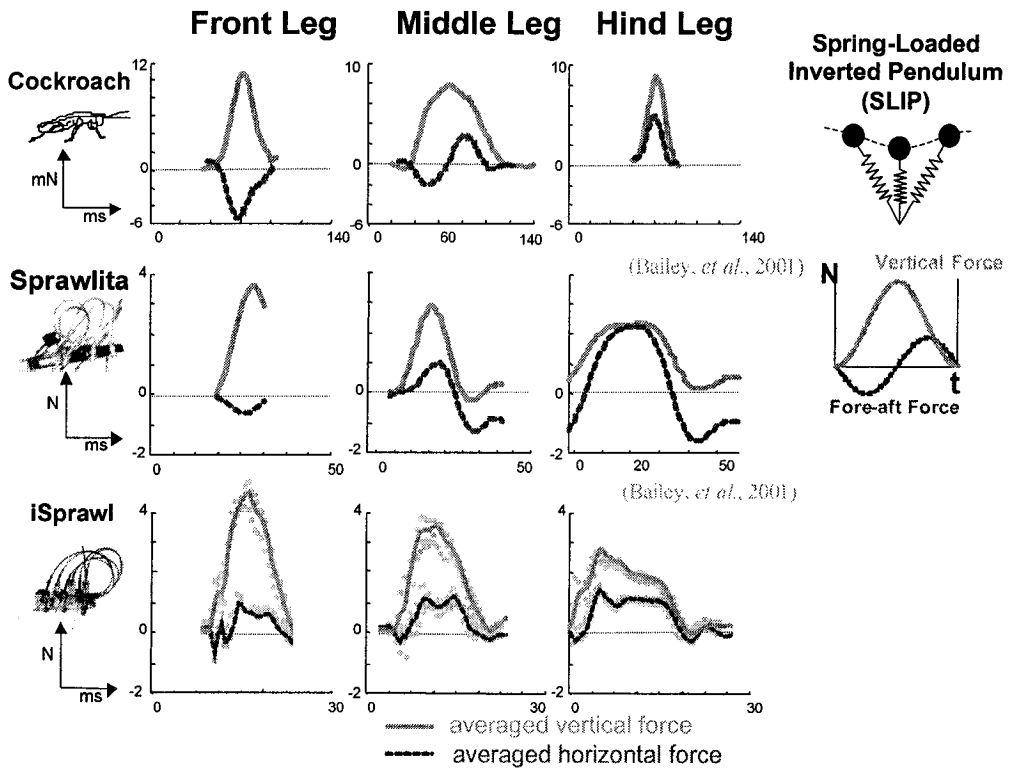

Figure 3.11: The vertical and horizontal individual leg ground reaction forces for a cockroach and *Sprawlita* [4] and for *iSprawl*, in comparison to the idealized SLIP model [9].

provide most of the forward propulsion at the end of each step (taking touchdown as the beginning of the step). The middle legs provide a mixture of propulsion and braking [49]. In addition, the front legs, being most nearly upright, have the largest vertical and smallest horizontal forces. The top two rows of Figure 3.11 show the averaged GRFs for a cockroach running and for *Sprawlita*, one of the first *Sprawl* robots with pneumatic pistons (from [30]). These patterns are similar except that the rear legs of the robot produce a negative horizontal force (drag) at the end of each stride rather than at the beginning as with the insect. The data for *iSprawl* were

taken with the robot running at 2.3 m/s over an ATI Omega force plate, and the signal was conditioned in the same manner as in [30]. The resolution of the sensor is at least 1/40 N in the vertical, and 1/80 N in the ground plane. The force pattern for *iSprawl* is similar to *Sprawlita*, with a couple of noticeable differences: the front legs provide less braking force and the rear legs have less drag. The reduction in parasitic foot drag is partly responsible for the greater speed of *iSprawl*. While the net drag of the feet is considerably less than in previous *Sprawl* robots, the tail of the robot still makes intermittent contact with the ground. The non-zero integral of the leg horizontal forces in *iSprawl* is mainly due to this drag force.

3.4 Summary

The development of a light and flexible power distribution system has allowed the creation of an autonomous, biologically inspired hexapedal runner. A comparison of the locomotion dynamics of the electrically powered *iSprawl* and the pneumatically driven *Sprawl* robots shows that despite the difference in actuation schemes, both robots demonstrate comparably fast and stable running with an open-loop actuation pattern. This suggests that the key design principles embodied in the *Sprawl* robots (namely: sprawled for-aft posture, thrusting legs, and passive hip joints with rotational compliance and damping) may have practical utility beyond this family of robots. A comparison of the leg extension profiles and ground reaction forces between the electric and pneumatic variants of the *Sprawl* robots shows that despite small differences, the essential motions and forces for fast and stable locomotion have been preserved.

We also found that when the passive properties of the robot, including the center of mass location, leg equilibrium angles, and leg stiffnesses were adjusted empirically for smoother running, the robot was able to run more than twice as fast. A more detailed tuning of the leg impedance may result in even faster and more stable running.

In comparison to other legged robots, *iSprawl* achieves an exceptionally high speed and Froude number, chiefly by virtue of having an extremely high stride frequency for its size. A comparison with running animals is somewhat more complicated. *iSprawl's*

Froude number of 10.8 is one at which most animals would have switched from a trot to a gallop. There are some notable exceptions such as elephants, which "Groucho-run" with Froude numbers as high as 3.4 [65] and cockroaches, which continue to use an alternating tripod gait for Froude numbers as high as 6–7 [52]. However, like other animals, cockroaches do not achieve their highest speeds by continuing to increase stride frequencies beyond the normal rate used for running [52]. Rather they increase their effective stride length via aerial phases. In contrast, *iSprawl* runs with a stride frequency comparable to that of a mouse although it has a body weight comparable to that of a well fed rat [62]. In comparison to other robots and to animals, *iSprawl* is capable of high stride frequencies chiefly because of the very low rotational inertia of its legs. This, in turn, is a direct consequence of having a single actuation source mounted in the body, with reciprocating motion directed to the feet via push-pull cables. Indeed, given the passive 45 Hz swing frequency of the legs, the maximum running frequency could, in theory, be even higher if a different motor and battery source were used.

Chapter 4

Spinybot: Climbing with compliant microspines

A new approach for climbing hard vertical surfaces has been developed that allows a robot to scale concrete, stucco, brick and masonry walls without using suction or adhesives. The approach is inspired by the mechanisms observed in some climbing insects and spiders and involves arrays of microspines that catch on surface asperities. The arrays are located on the toes of a robot and consist of tuned, multi-link compliant suspensions. This chapter also discusses toe suspension properties to conform to surface irregularities and to distribute climbing loads among many spines. The principles are demonstrated with a new climbing robot, SpinybotII, that can scale a wide range of exterior walls, carry a payload equal to its own weight, and cling without consuming power. The research on SpinybotII has been a joint work with Alan Asbeck and his contribution on initial ideas of foot manufacturing, the linkage design, and spine scaling analysis are gratefully acknowledged.

4.1 Introduction

In recent years, there has been considerable progress in small, legged robots that can run rapidly and stably over rough terrain [31, 108, 104, 47]. Climbing and maneuvering on vertical surfaces presents a more difficult challenge, one that robots are just

beginning to address. Small robots that can climb a variety of hard and soft surfaces unobtrusively and cling for extended periods of time without high power consumption would be beneficial for applications such as surveillance or the inspection of hard-to-reach locations.

Previously developed climbing robots have generally employed suction cups [78, 80, 127], magnets [18, 122] or adhesives [43, 44] to cling to smooth vertical surfaces such as windows and interior walls. None of these approaches is suitable for porous or dusty exterior surfaces such as brick, concrete, stucco or stone. Other climbing robots employ hand and foot holds in the manner of a human climber [19, 25]. A recent innovation employing a controlled vortex [1] to create negative aerodynamic lift has been demonstrated on brick and concrete walls with considerable success. However, this approach consumes significant power (including when the robot is stationary), unavoidably generates noise and is more difficult to adapt to non-flat surfaces such as window ledges and corners.

When we look at animals that exhibit agility on vertical surfaces, we find a variety of methods employed [28]. Larger animals such as cats and raccoons have strong claws that can penetrate wood and bark surfaces. Tree frogs and many insects employ sticky pads [45, 46]. Geckos and some spiders utilize large numbers of very fine hairs that achieve adhesion via *van der Waals* forces on almost any kind of surface [15, 72, 9]. Other insects, arthropods and reptiles employ small spines that catch on fine asperities [40]. All of these approaches are worthy of examination for climbing robots. However, dry adhesives and spines are particularly attractive for hard, dusty, exterior surfaces.

4.2 Spine and Surface scaling

Insects and arthropods that climb well on vertical surfaces often have legs equipped with large numbers of small, sharp spines. At a larger scale, geckos that frequent rock surfaces such as cliffs and caves have small claws on each toe in addition to their dry adhesive structures [125]. Unlike the larger claws of a cat, spines do not need to penetrate surfaces. Instead, they engage small surface asperities. Several studies in the biology literature have considered the problem of spine/surface interaction.

Dai et al. [40] present a planar model of spine/asperity contact and compute the maximum load per spine as a function of spine strength, relative size of the spine tip versus that of an asperity, and coefficient of friction. As expected, for rough surfaces the mechanical strengths of the spine and asperity become the limiting factors; for smoother surfaces friction is more important, and the ability to pull along the surface is much reduced.

Given the general correlation in nature between spine or claw size and animal size, we ask: for a climbing robot of a certain size, how large should the spines be? For a 0.4 Kg robot we might expect spines or claws similar to those seen in squirrels or large climbing lizards. However, this argument ignores the point that spines of hardened steel are much stronger and stiffer than their natural counterparts. If the strength of the spine/asperity contact were not a constraint, the spines should be as small as possible.

The reason behind this argument is that many natural surfaces, and some man-made surfaces such as concrete and stucco, have an approximately fractal surface topography [35, 60, 61] so that characteristic surface features (asperities) can be found over a wide range of length scales. Following the arguments of Dai et al. [40] for spines of a certain tip diameter, d_s, we are interested in asperities of average diameter $d_a > d_s$to obtain effective interlocking. Given the self-similar nature of fractal surfaces, we can expect the density of such asperities to grow at least as $1/d_a^2$ per unit area of the wall. In practice, there is a lower limit to the useful spine dimensions. When steel spines catch on asperities on concrete or stucco, the contact typically fails in one of three ways [10]:

- plastic failure of the base of the spine in bending,
- excessive elastic rotation of the spine tip causing it to slip off the asperity,
- brittle failure of the asperity itself.

In each of these cases, if we take a dimension such as the spine tip diameter, d_s, as a characteristic length and scale everything uniformly, then the maximum load of the spine/asperity contact increases as d_s^2 (see Appendix A.2 for details).

SpinybotII employs two rows of spines on each foot, each spine having a tip diameter of approximately 25 μm. The maximum force per spine/asperity contact is 1-2 N, and the probability of finding useable asperities per square centimeter of wall is high. To summarize the preceding arguments, as spines become smaller the robots can ascend smoother surfaces because the density of useable spine/asperity contacts increases rapidly. However, the feet need larger numbers of spines because each contact can sustain less force. In order to make use of large numbers of spines, the first two design principles behind climbing with microspines are therefore:

- ensure that as many spines as possible will independently find asperities to attach to,
- ensure that the total load is distributed among the spines as uniformly as possible.

The design of feet that embody these principles is described in next section. In addition, as with any climbing robot, it is important to keep the center of gravity as close to the wall as possible and to avoid imposing any forces or moments at the feet that could lead to premature detachment. The features of SpinybotII that achieve these effects are described in Section 4.5.

4.3 Toe and Foot Design: Promoting Attachment and Load Sharing

The feet on SpinybotII represent the sixth generation of a compliant, spined design. Each foot contains a set of ten identical planar mechanisms, or "toes." Each of the toes is a compliant multi-bar linkage, independent of its neighbors and able to stretch parallel to the wall under a load. Thus, if a toe catches an asperity, neighboring toes are not prevented from catching their own asperities because they will continue to slide down the wall as the caught toe stretches. Figure 4.2 shows a side view of the robot on a concrete wall and a detail of a single foot, showing several of the planar toe mechanisms, each of of which bears two spines (several of which are visibly engaged).

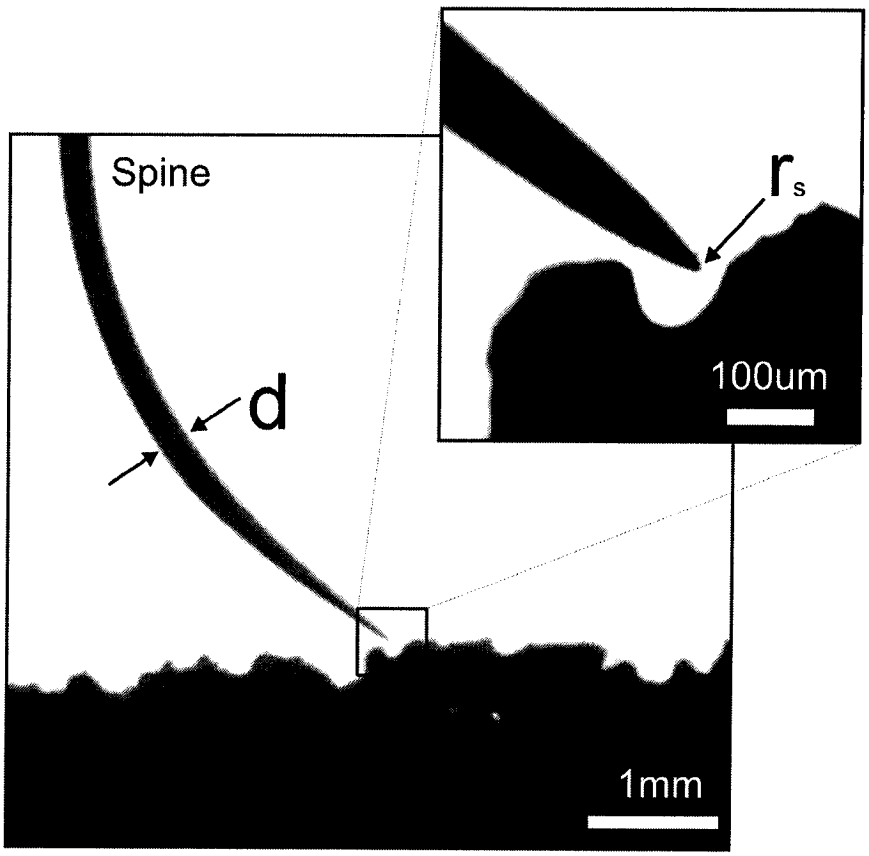

Figure 4.1: Profile photograph of typical spine, with shaft dia., $d = 270\mu m$ and tip radius $r_s = 10\mu m$, engaging a rough profile of 80 grit aluminum oxide sandpaper.

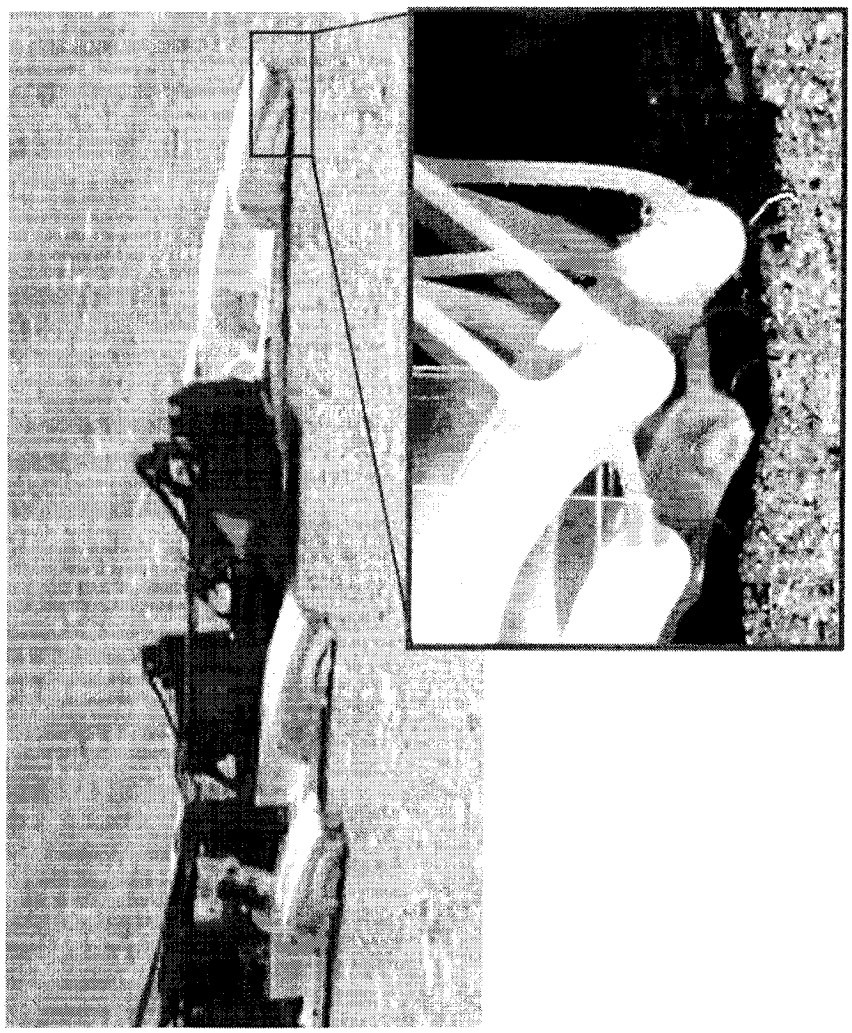

Figure 4.2: Picture of upper section of SpinybotII on concrete wall and detailed view of several spines independently engaging asperities on the concrete surface.

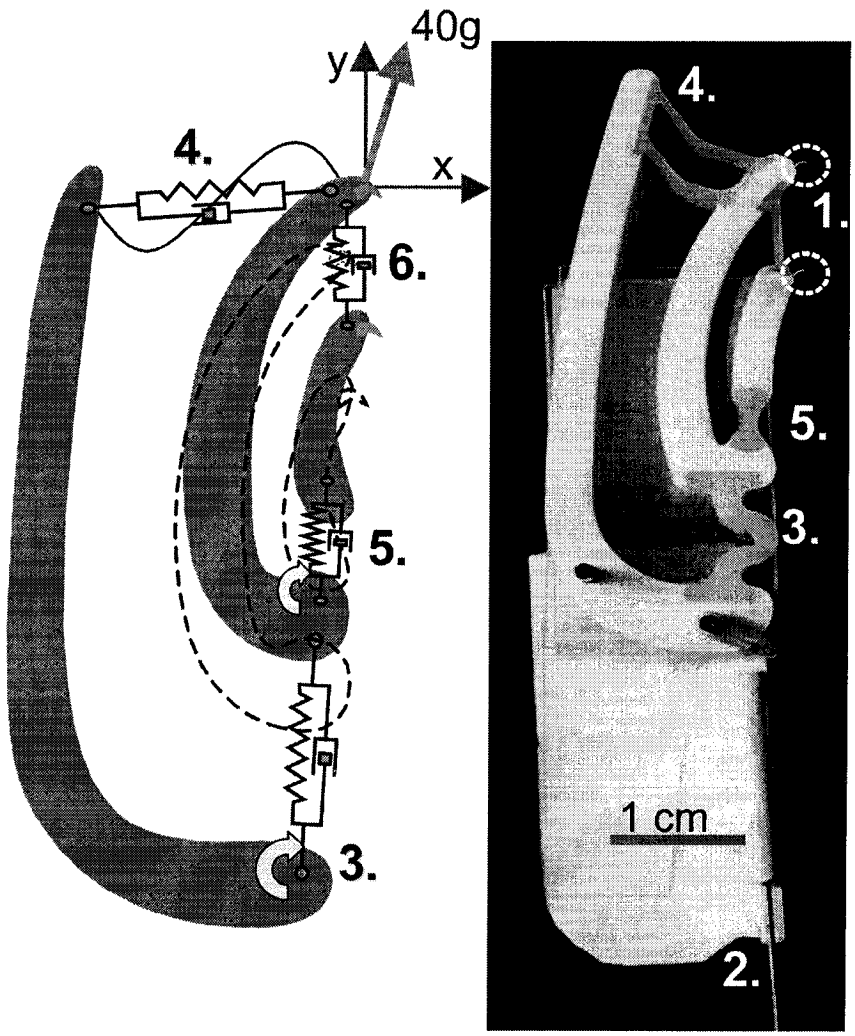

Figure 4.3: Photograph and equivalent elastic linkages for one toe of the climbing robot. Linkage at left shows the deflected position for a 40g load, superimposed on the undeflected position (shown in dotted lines). Key to labels: **1.** 200 mm diameter spines (inside dotted circles), **2.** tendon for applying loads, **3.** soft urethane flexure permitting travel in y direction, **4.** buckling flexures with large compliance value in the $-x$ direction under compression, lower compliance under tension, **5.** primarily rotational flexure for the proximal spine, **6.** buckling/lift-off flexure for proximal spine.

The mechanisms are created using a rapid prototyping process, Shape Deposition Manufacturing [92, 21] that permits hard and soft materials to be combined into a single structure. In the present case, the white and grey materials are hard and soft urethanes, of 75 Shore-D and 20 Shore-A hardness, respectively (Innovative Polymers Inc.). The resulting structure can be approximated as an elastic multi-link mechanism, as shown in Figure 4.3.

The spines are approximately 1.5 mm long with a 200 μm shaft diameter and 10-35 μm tip radius. They are embedded directly into the hard white links during the SDM process. The soft urethane flexures provide both elasticity and viscoelastic damping. They permit greater extensions without failure than miniature steel springs (as were used on some of the earlier foot designs).

Following the approach from Chapter 2, for small deflections, the linear and rotational compliance of each spine in the two-dimensional cartesian coordinate plane can be modeled using a 3x3 compliance matrix, C, taken with respect to a coordinate system embedded in the spine:

$$\begin{bmatrix} c_{xx} & c_{xy} & c_{x\phi} \\ c_{xy} & c_{yy} & c_{y\phi} \\ c_{x\phi} & c_{y\phi} & c_{\phi\phi} \end{bmatrix}$$

At initial contact, we require that c_{xx} be very big for displacements in the $-x$ direction, so that a large number of toes can conform to uneven surfaces without requiring a significant normal force. This is accomplished through the flexures at the end of the toe (labeled 4. in Figure 4.3), which are designed to buckle so that they have a very high compliance for $-x$ deflections. For small tensile loads on the foot (in the $+x$ direction), some toes will still be compressed from the foot's engaging motions. c_{xx} should still be big in this case so these compressed toes do not push the foot away from the wall. This presents a design compromise since a smaller c_{xx} will move the spines back to the wall more quickly if they should slip and undergo a "skipping over the wall" phenomenon. Finally, for large tensile loads, c_{xx} should be small so the toes can disengage from the wall. This is also accomplished with the flexures at the end of the toe.

Table 4.1: SpinybotII Toe Compliance Matrices

Outer Spine:

$$\begin{bmatrix} 6.612 & 0.725 & -0.0197 \\ 0.725 & 1.45 & 0.00209 \\ -0.0197 & 0.00209 & 1.11 \end{bmatrix}$$

Inner Spine:

$$\begin{bmatrix} 7.27 & 0.909 & -0.0312 \\ 0.909 & 6.36 & -0.00282 \\ -0.0312 & -0.00282 & 1.72 \end{bmatrix}$$

Units:

$$\begin{bmatrix} mm/N & mm/N & rad/N \\ mm/N & mm/N & rad/N \\ rad/N & rad/N & rad/Nmm \end{bmatrix}$$

C Matrix:

$$\begin{bmatrix} c_{xx} & c_{xy} & c_{x\phi} \\ c_{xy} & c_{yy} & c_{y\phi} \\ c_{x\phi} & c_{y\phi} & c_{\phi\phi} \end{bmatrix}$$

At the same time, c_{yy} should be moderate, as it represents a trade-off. A softer c_{yy} allows each toe to stretch more in the longitudinal direction to increase the probability that it will catch an asperity during the downward stroke of the foot; but if c_{yy} is too big, the mechanism will require an excessive stroke length to support a given load. In essence, these factors determine the "asperity search length" for the downward stroke of the toe. At the same time, c_{xy} should be small so that stretching in the y direction does not cause the spines to retract. The $c_{x\phi}$ and $c_{y\phi}$ terms should also be small and, preferably, slightly negative so that displacements in the x or y direction are not accompanied by anticlockwise rotations in the (x, y) plane that would lead to premature disengagement.

The compliance matrix C was measured on a Spinybot toe, for both the outer and inner spines, relative to the outermost hard member of the toe. The compliances were measured around an operation point of (-0.13cm, 0.13cm) in the (x,y) directions. The results are shown in Table 4.1, and they can be seen to generally correspond to the desired values as discussed previously.

The toe mechanism shown in Fig. 4.3 was also modeled using Working Model^{TM} software (MSC Inc.), and the various linear and rotational compliance elements were adjusted to match bench-top test results of SpinybotII toes. The results are summarized in Table 4.2. The mechanism is designed so that initial contact at the inner, or proximal, spine actually forces the distal spine slightly outward ($+x$ direction) to increase the probability that it will also contact an asperity.

Once one or both spines have contacted the wall, the toe can apply a force that

Table 4.2: Compliances and Damping Parameters for Toe Linkage

Location (numbered label, Fig. 4.3)	Parameter in kinematic model c = linear compliance element b = linear damping element c_t = rotational compliance element
3.	c = 16.7 mm/N b = 0.1 Ns/m c_t =2 rad/Nmm
4.	c = 1.11 mm/N in tension c = 20 mm/N in compression b = 0.02 Ns/m
5.	c =1 mm/N b = 0.001 Ns/m c_t = 10 rad/Nmm
6.	c = 16.7 N/mm b = 0.1 Ns/m

is mainly vertical, with a small inward ($+x$) component to help the robot climb. Fig. 4.3 shows the effect of a typical 40 gram load sustained by one toe in climbing.

4.4 Underactuated leg design

An important observation of agile scansorial animals like geckos is that they employ *multi-level conformability* (e.g. lamellae, toes, and limbs) and *redundancy* (multiple pads per toe, multiple toes per foot, and multiple feet in contact) for reliable climbing. The same principles have been found necessary for SpinybotII. Accordingly, the entire foot mechanism is mounted on a prismatic joint with an elastic suspension that allows it to move up to 1 cm in the distal ($+y$) direction (see Fig. 4.4). In addition, the entire foot assembly is spring loaded by a second elastic element behind the pivot, where it is connected to a rotary RC servo motor. The result is an under-actuated R-R-P serial kinematic chain that traces a loop trajectory, as shown in Fig. 4.4, when the servo motor rotates back and forth. After some experimentation, the best elastic elements were found to be 6.4mm diameter elastic bands commonly used for dental braces.

Following the framework introduced in Chapter 2, each SpinybotII leg is an underactuated linkage system. The first joint, θ_1, is rigidly attached to the R-C servo motor. The second joint, S_2, is a passive prismatic joint (an elastic band) as a part of the four bar linkage. This elastic band provides tension selectively according to the configuration. The third joint, S_3, is a prismatic joint that passively helps promote force distribution among the legs. The trajectory of the foot is generated by rotation of the first joint, in combination with contact forces. Unlike cursorial robots, climbing robots cannot produce large forces against the wall surface. Accordingly, the compliance in the normal direction must be high. In the case of SpinybotII, the second, rotary joint temporarily becomes a free joint at the start of the stance phase to accommodate this requirement. In Chapter 5, it will be seen that Stickybot exhibits a very soft, nonlinear compliance in the normal direction for the same reason.

The design of adaptive underactuated legs for climbing robots is closely related to adhesive or attachment properties of the feet. The spines exhibit a highly directional

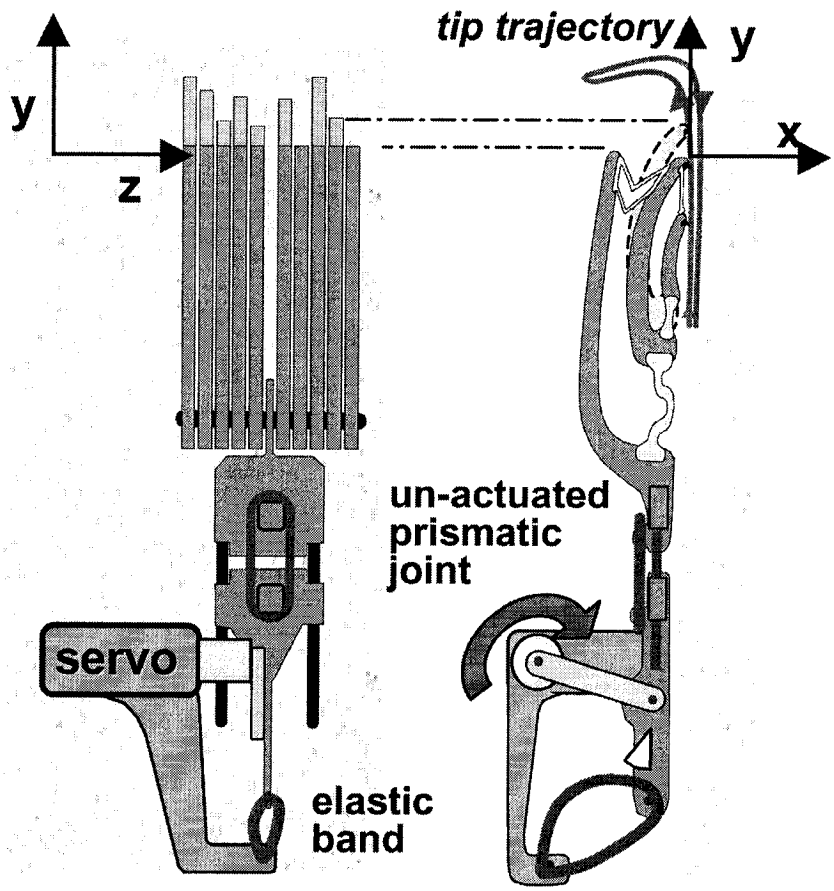

Figure 4.4: Side and plan view of one foot containing ten toes. The toes can deflect independently of each other. In addition, the entire foot can displace in the distal (y) direction due to an un-actuated prismatic joint.

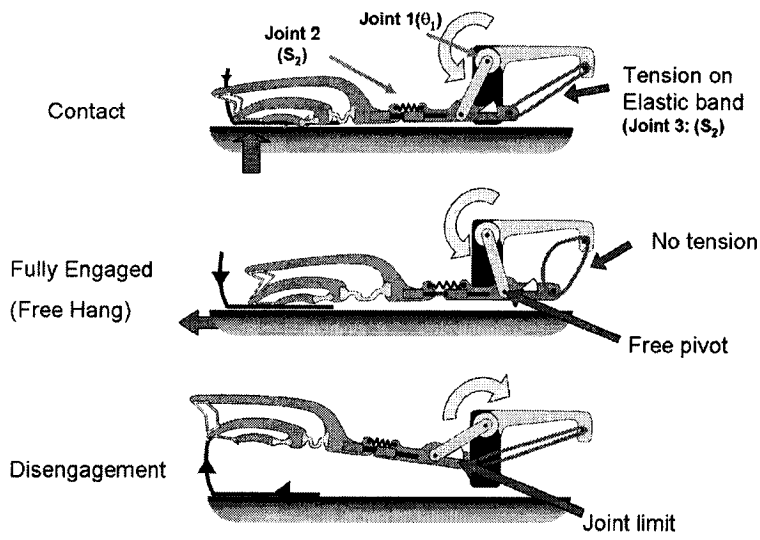

Figure 4.5: The sequence of motions is accomplished using an underactuated mechanism consisting of a single rotary RC servo motor and an elastic band that is taut while the foot is disengaged. **Top**: Tension in rubber band helps engagment of spines to asperities. **Middle**: When the foot is engaged, the loose elastic band prevents forces that would push the robot away from the wall. **bottom**: A hard stop causes the leg to lift off the wall as the servo rotates upward, with the elastic band keeping the leg pushed against the hard stop.

behavior; they generate large forces parallel to the wall and small inward forces when properly loaded. The SpinybotII leg is designed to utilize this directional characteristic to facilitate attachment and detachment. Upon engagement, the normal force is a function of the compliance in the leg and the preload of the elastic band. The compliance is high, so that minor variations in the position of the robot with respect to the wall produce only small variations in the normal force. Instead, the normal force is mainly a function of the preload in the elastic band, which is adjusted by choosing a band of a particular length and controlling the amount that it is stretched. Once the foot has engaged some asperities, the nominal trajectory of the foot deviates from unloaded trajectory resulting in forces.

The transition between one set of feet and the next is somewhat tricky. For secure engagement, the preload in the passive linkage plays a crucial role. However, this preload can cause the body to be pushed away from the surface after full engagement because previously attached feet become detached and stop providing a pull-in force. In Figure 4.5, the rubber band applies forces normal to the surface for only short period of time during engagement and becomes loose to remove undesirable reaction forces.

In summary, recalling the design process introduced in Chapter 2, we have several steps involved in designing the SpinybotII leg mechanism:

1. Identify desired behaviors of the designated mechanism
2. Identify desired norminal trajectory to acheive desired behaviors
3. Specify compliance matrices of points of interest along the trajectory.

The most important desired behavior is to achieve straight, stable and reliable climbing. This, in turn, requires (1) minimum reaction forces in the normal direction and (2) keeping the entire mass of the robot as close as possible to the wall at all times. In order to satisfy these conditions, the desired trajectory of the leg should be a nearly straight line along the wall. For this loaded trajectory, the desired compliance in normal direction to the wall needs to be large. (The actual SpinybotII leg has infinite compliance just after engaging the feet.) The compliance in the vertical

direction, which is a combination of toe compliance is chosen to distribute the forces among the feet, especially when there is sudden movement such as slight slip.

The first joint, θ, has no compliance, and we have two compliant joints, S_2 and S_3. The Jacobian matrix for these joints is:

$$J = \begin{bmatrix} 0 & 1 \\ 13.3 & 0 \\ 0.133 & 0 \end{bmatrix}$$

The dimensions are mm for length and radians for angle. The compliance matrix at the desired configuration is:

$$C_j = \begin{bmatrix} 4.0 & 0 \\ 0 & 6.3 \end{bmatrix}$$

$$C = JC_jJ^T$$

$$C = \begin{bmatrix} 6.3 & 0 & 0 \\ 0 & 707.5 & 7.07 \\ 0 & 7.07 & 0.078 \end{bmatrix}.$$

In this leg compliance matrix, c_{yy} is much bigger than c_{xx}. This enables an extremely soft suspension in the normal direction to the wall so that the variation of the preload on engagment is small. As mentioned earlier, we tune the preload by changing the length and the pre-stretch of the rubber band.

4.5 Body Design: Promoting Load Sharing and Stability

The robot utilizes an alternating tripod gait, similar to that found in climbing insects (see Figure 4.6). At any time, the robot is ideally clinging by three feet. Like many climbing animals, the robot also has a tail which reduces the forces required at the front limbs to overcome body pitch-back from the wall. This pitch-back moment is produced by gravity acting at the center of mass, which is located approximately 2 cm

Table 4.3: SpinybotII Specifications

Mass	0.4 Kg
Max payload	0.4 Kg
Climbing speed	2.3 cm/s
Distance: COM to wall surface	2.0 cm
Batteries	lithium polymer total 340 mAh, 7.4 volts
Processor	40 MHz PIC
Servo motors (7 total)	0.37 Nm torque
Camera	0.02 Kg

outward from the wall. The weight of the robot, including lithium polymer batteries, wireless camera, and PIC microprocessor is 0.4 Kg. It can carry an additional payload of 0.4 Kg while climbing.

The climbing speed is quite slow (2.3cm/s) but can easily be improved upon with the addition of structural damping in the limbs and toe suspension. On initial contact of each foot with the wall, the spines and leg as a whole oscillate as underdamped structures. Such oscillations reduce the probability of engaging useful asperities as the spines are stroked along the wall. The addition of structural damping will greatly improve climbing performance and permit climbing at greater speeds. Higher performance motors may also be desirable.

While the main concern for vertical climbing is to avoid pitching back from the plane of the wall, it is also important to maintain rotational stability in the plane of the wall so that momentary slips to not become catastrophic. As seen in Figure 4.6 the center of mass of SpinybotII lies within a polygon of contacts when three feet are attached to the wall. If only two feet are attached, the center of mass generally remains within the polygon of contacts, due to the elongated body design. Also, as observed in climbing insects and reptiles, the legs have a slight inward pull toward the centerline of the robot. This arrangement reduces the upsetting moments (in the

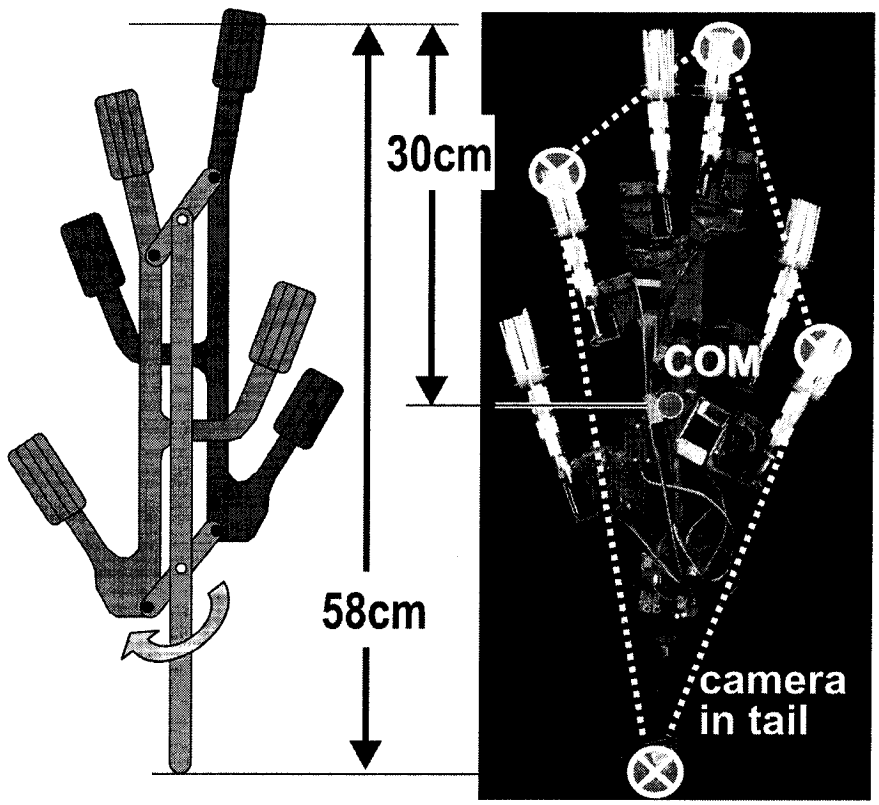

Figure 4.6: Photograph of SpinybotII wall and diagram of climbing mechanism. Each set of three legs is attached to a mechanism that allows the robot to "ratchet" its way up the wall with an alternating tripod gait. A long tail helps to reduce the pitching moment. The center of mass (COM) is within the polygon of contacts, to minimize yawing rotations in the plane of the wall.

Table 4.4: Effect of Scaling Parameters on Toe Compliances. Desired suspension compliances in the x- and y-directions (i.e., $1/k_{xx}$ and $1/k_{yy}$, respectively) vary as a function of robot weight, spine size and number of spines. The values in the table show how the compliances should be varied to maintain a constant x-direction compliance for the entire foot, and appropriate displacements in the y-direction, to engage most of the spines while not over-extending them. Usually the required number of toes n depends on the spine size, leading to $n \propto 1/r_s$ for a constant robot mass.

Compliance $(1/k)$	Normal Direction	Axial Direction
Number of toes n	$\sim 1/n$	$\sim 1/n$
Robot mass m	*constant*	$\sim 1/m$
Spine tip radius r_s	*constant*	$\sim r_s$

plane of the wall) about the center of mass, should one of the legs momentarily lose its grip. If one of SpinybotII's three attached feet loses its grip, the robot will continue, usually only suffering from a slight change in heading; if multiple feet lose their grip it falls.

4.6 Discussion

SpinybotII climbs reliably on a wide variety of hard, outdoor surfaces including concrete, stucco, brick, and dressed sandstone with average asperity radii >25 μm. The essential principles behind its operation include using many miniature spines with a compliant suspension that ensures that the load is shared uniformly among them. The same principles can also be applied to larger robot platforms. Desired spine tip radius is a function of average asperity size for the surfaces to be climbed and not of robot size.

A more challenging problem is to tackle rough or corrugated surfaces or, in general, surfaces that have roughness comparable to spine length. Either the feet and toes must have enough "suspension travel" to accommodate the contours of the surface or they must have an additional active degree of freedom, like the toes of geckos or the tendon-actuated tarsus of insect legs. On contoured surfaces it should be possible to exploit internal "grasp" forces, in a manner similar to that used by robots that

climb with hand-holds and foot-holds [25, 19], for additional security. The compliant suspension of the spines will become an increasingly difficult design challenge as spines are made smaller: smaller spines necessarily have a smaller clearance, possibly preventing them from reaching deep holes in the surface while maintaining a favorable loading angle.

Another challenging problem is to climb surfaces with much lower roughness than concrete or sandstone, such as polished stone or interior wall panels. For smooth panels the average asperity radius may be on the order of a few micrometers, requiring spine tip radii of perhaps 1 μm. These extremely small spines will be over 100 times weaker than the spines on SpinybotII and a large number of them will be required, unless the overall mass of the robot can be reduced correspondingly. Going still smaller, we approach the dimensions of the hairs that are being investigated for synthetic dry adhesives [9, 91, 114, 57]. At the smallest scales, hairs utilizing adhesion have two advantages over microspines or nanospines: they are less sensitive to the local surface normal distribution and they are loaded primarily in tension, rather than in bending.

For a given surface, at a small enough length scale, the surface will appear fractal. For length scales smaller than this, the number of asperities per unit area will grow as $1/r^2$. Since the spine strength grows as r^2, we hypothesize that the total weight that can be sustained per unit of surface area using spines is approximately constant. This weight per unit area number will depend on the distribution of surface normal angles, which is related to the surface's fractal dimension.

An interesting question is whether some combination of spines and adhesive hairs will ultimately prove most effective for scaling a variety of hard vertical surfaces. Different surfaces have different distributions of surface normal angles. Spines perform best on surfaces with normal angles close to 90°, while dry adhesives do best on smoother surfaces with normal angles closer to 0°. To be able to climb the widest variety of surfaces, both spines and dry adhesives could be used.

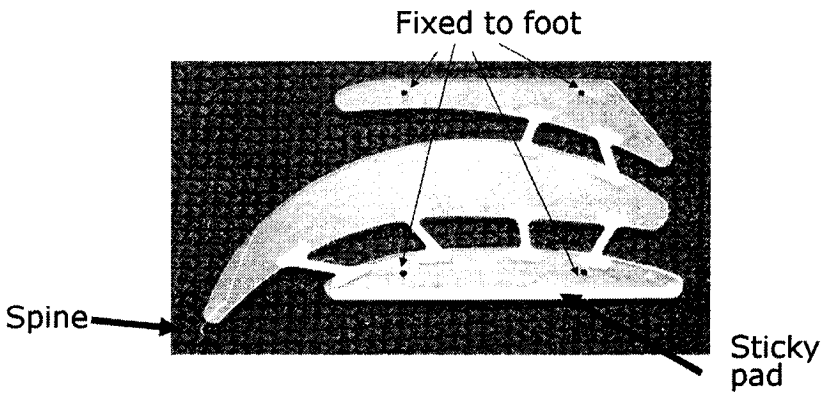

Figure 4.7: Photograph of new toe design. For heavier robots, this toe design is thinner and studier at higher forces. Flexure(white part) angle is aligned in various angle from bottom structure such that the toe produce nonlinear stiffness.

4.6.1 Adapting Spines to Heavier Robots

The design principles above can be readily applied to other robot platforms, with some adaptation required to accommodate larger loads. As discussed in the previous section, the desired spine tip dimensions are primarily a function of the surfaces to be climbed, and not of robot size. Consequently, for a given spine size, a heavier robot requires more spines per foot and the risk of spine failure (or surface failure) is greater. In other words, it is more essential to load the spines uniformly. The loading problem is complicated by the need to tune the compliances of the toes based on total robot weight and total number of spines, as discussed in Section 4.3. The toes also need to stretch independently of their neighbors to ensure that each spine has a high probability of engaging asperities and to ensure load sharing. Consequently, it does not suffice simply to make the toes robust and stiff.

Fig 4.7 shows a new toe suspension design with a $200\mu m$ spine. The number of spines per unit width is higher than previous design because the thickness of the toe is 0.8mm which is slightly thinner than Spinybot's. Also, this design excludes the buckling flexure, which tends to buckle out of the plane in a thinner toe design, and

employs mutiple flexures for both normal and tangential compliances. Flexures in the back (right side in the picture) participate less when the tangential force is relatively low and produce more resistance force as the tangential force increases. This non-linear effect allows each toe to carry higher forces and keep a low stiffness for small deflections, facilitating force distribution. A soft polyurethane layer at the bottom of the structure provides adhesion when the foot is brought into contact with smooth surfaces. This toe design allows a 4kg robot to cling to surfaces such as a stucco wall.

Chapter 5

Stickybot : Climbing with Directional adhesion

Stickybot is a bio-inspired robot that climbs smooth vertical surfaces such as glass, plastic and ceramic tile at 4 cm/s. The robot employs design principles adapted from the gecko including a hierarchy of compliant structures, directional adhesion, and control of contact forces to achieve control of adhesion. In this chapter, I describe the design and fabrication methods used to create under-actuated, multi-material structures that conform to surface roughness ranging from centimeters to micrometers. At the finest scale, the undersides of Stickybot's toes are covered with arrays of small, angled polymer stalks. Like the directional adhesive structures used by geckos, they readily adhere when pulled tangentially in the direction that the stalks are inclined; when pulled in the opposite direction, they release. Working in combination with the compliant structures and directional adhesion is a force control strategy that balances forces among the feet and promotes smooth attachment and detachment of the toes.

5.1 Introduction

Mobile robots that can climb and maneuver on vertical surfaces are useful for inspection, surveillance, and disaster relief applications. Previous robots capable of climbing exterior building surfaces such as stucco and brick have utilized microspines similar

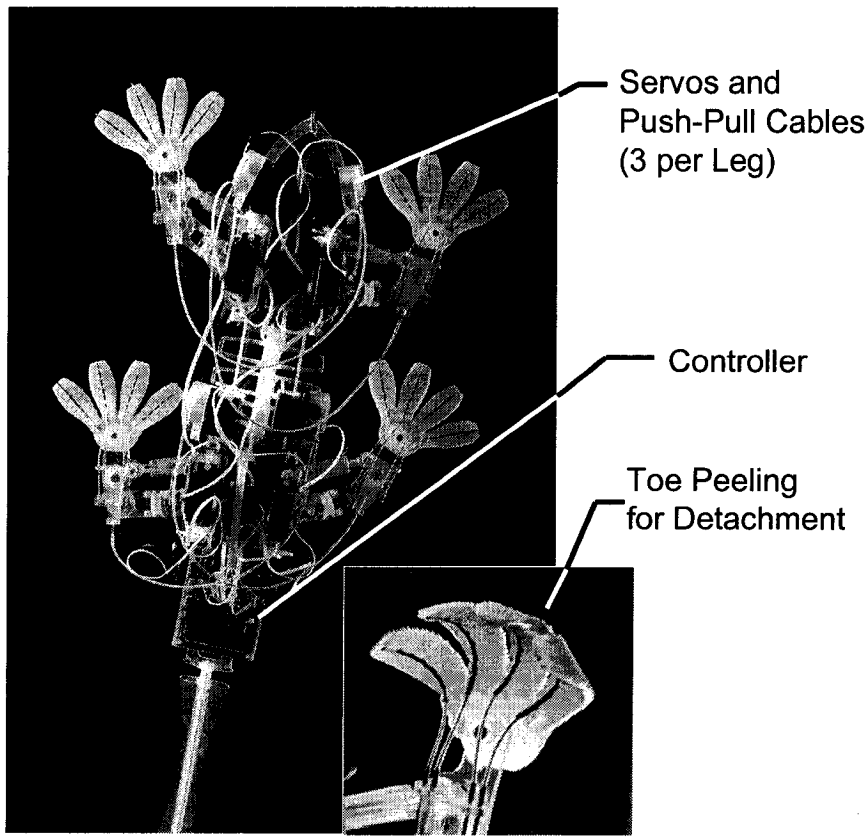

Figure 5.1: Stickybot, a new bio-inspired robot capable of climbing smooth surfaces. Inset: detail of toes curling to facilitate detachment.

to those found on insects [10, 109] or a controlled vortex that creates negative aerodynamic lift [1]. Smooth vertical surfaces have been climbed using suction [79, 127], magnets [17, 121], and pressure-sensitive adhesives (PSAs), such as tape [42, 118]. PSAs exhibit high adhesion on smooth surfaces but foul easily and require relatively high forces for attachment and detachment. Some researchers have circumvented this problem by using spoked-wheel designs that allow the detachment force at a receding point of contact to provide the necessary attachment force at the next [42]. Wet adhesive materials have also been employed, drawing inspiration from tree frogs and snails [33]. All of these solutions have been successful, but are limited in their range of surfaces. To develop a robot capable of climbing a wide variety of materials, we

have taken design principles adapted from geckos. The result is Stickybot (Fig. 5.1), a robot that climbs glass and other smooth surfaces using directional adhesive pads on its toes.

Geckos are arguably Nature's most agile smooth surface climbers. They can run at over 1m/s, in any direction, over wet and dry surfaces of varying roughness and of almost any material, with only a few exceptions like graphite and Teflon [11]. The gecko's prowess is due to a combination of "design features" that work together to permit rapid, smooth locomotion. Foremost among these features is hierarchical compliance, which helps the gecko conform to rough and undulating surfaces over multiple length scales. The result of this conformability is that the gecko achieves intimate contact with surfaces so that van der Waals forces produce sufficient adhesion for climbing [11].

The gecko's adhesion is also directional. This characteristic allows the gecko to adhere with negligible preload in the normal direction and to detach with very little pull-off force, an effect that is enhanced by peeling the toes in "digital hyperextension" [12].

A consequence of the gecko's directional adhesion is that it must control the orientation of its feet when ascending or descending. In addition, the gecko controls the tangential contact forces to achieve smooth climbing with minimal pull-off forces [13].

In the following sections, I discuss hierarchical compliance, directional adhesion and force control for climbing in more detail and describe how they are implemented in Stickybot. I also provide details of the design and fabrication of Stickybot's feet equipped with arrays of directional polymer stalks (DPS). I present the results of experiments to confirm the DPS directional behavior and describe the controller used to ensure that they are loaded appropriately. I also present a comparison of attachment and detachment forces for Stickybot climbing with directional versus non-directional adhesives, illustrating the advantages of the former. I conclude with a discussion of some of the limitations of the current Stickybot technology and plans to overcome them for faster, more robust and more dirt-tolerant climbing in the future.

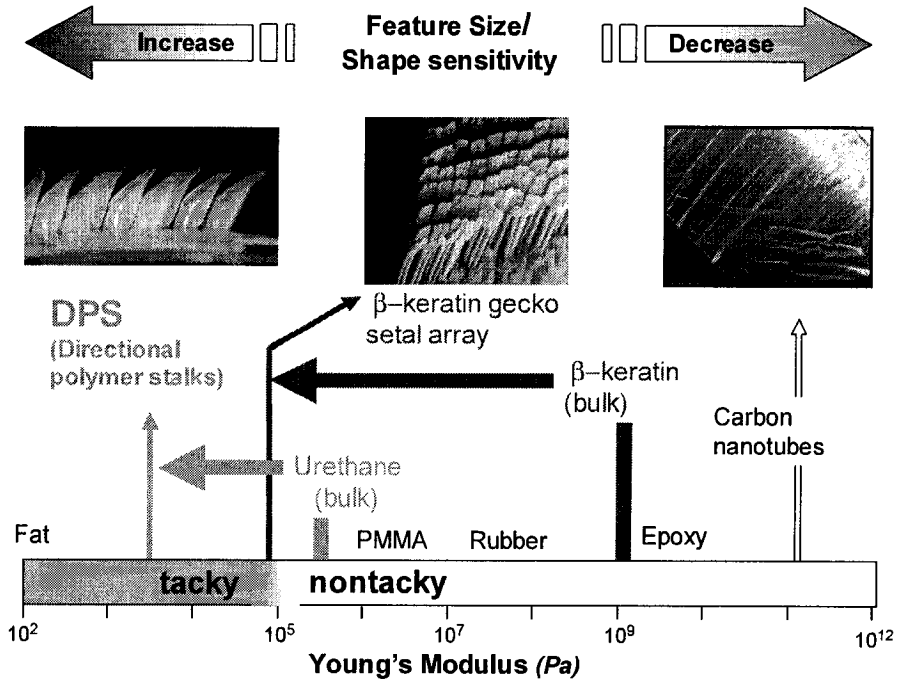

Figure 5.2: Modulus of bulk material and feature size of distal end of different structures. Microstructured geometries can lower the overall stiffness of bulk materials so that they become tacky. This principle allows geckos to use β-keratin for their adhesive structures. At smaller scales, tip geometry plays a less important role in adhesion forces, for a given bulk material modulus.

5.2 Adhesion and Compliance

When two surfaces are brought together, adhesion is created via van der Waals forces. Since van der Waals forces scale as $1/d^3$ where d is the local separation between two flat surfaces [67], it is critical for the surfaces to be within an order of 10s of nanometers of each other. Pressure-sensitive adhesives (PSAs) accomplish this with a soft layer that flows and conforms to the surface, thus maximizing the contact area. PSAs can provide sufficient adhesion levels for a robot to climb a wall [42, 118], but they have several disadvantages compared to the hierarchical compliant structures used by geckos. To adhere to rough surfaces an additional layer of conformability is usually required, which is why high performance adhesive tapes for relatively rough

surfaces often have a backing layer of soft foam [99]. Substantial preloads in the normal direction are required to achieve adhesion and large forces are also required for detachment, leading to inefficient climbing. In addition, PSAs quickly become contaminated with dirt and lose their stickiness.

To overcome the limitations of PSAs, there has been recent interest in creating synthetic "dry" or "self-cleaning" adhesives that do not foul over time. These adhesives use stiff, initially non-sticky bulk materials in combination with microstructured geometries to conform to surfaces. Figure 5.2 shows some adhesive solutions ordered in terms of feature size, effective modulus and general trend of shape sensitivity based on size. For a material to be considered tacky, its effective modulus must be less than 100kPa [11, 39, 14]. This "tack criterion" comes from the need to conform intimately to a surface in order for van der Waals forces to become significant. The gecko conforms to surfaces despite having a relatively high bulk material stiffness ($\approx$ 2GPa for β-keratin) [11] by using a hierarchy of microstructures consisting of lamellae, setae, and spatulae. This hierarchical geometry lowers the effective stiffness of the whole structure to make the system function like a tacky material without causing fouling. A fibrillar structure also helps force distribution by splitting contact surfaces.

Several types of synthetic dry adhesives have been manufactured, including arrays of vertically oriented multiwall carbon nanotubes [124, 126] and polymer fibers [58, 73, 97, 113]. These adhesives use stiff, hydrophobic materials and have achieved useful levels of adhesion, but only with careful surface preparation and high normal preloads.

An alternative method to creating adhesives is to start with a somewhat softer material on the order of 300kPa to 3MPa. These materials can employ larger feature sizes and still conform to surfaces because they are softer to begin with. Unlike dry adhesives, these materials will attract dirt; however, in contrast to PSAs, they can be cleaned and reused. One such example is a microstructured elastomer tape [41, 98].

In addition to the effective stiffness of the corresponding structure, the size and shape of the contacting elements are important in sustaining adhesion [8, 54, 55, 58, 75, 123]. For a given loading direction, having a special tip geometry is benificial to reduce stress concentration, thereby increasing the adhesion of a single distal element.

Interestingly, at smaller scales, tip geometry is less important than at larger scales since less deformation energy is required to conform and achieve a desired stress distribution across the contact surface. Therefore, for smaller sizes, sensitivity to tip geometry is relatively low but for larger features the tip geometry dramatically affects adhesion, at constant bulk material stiffness. Figure 5.2 (top) shows the general tendancy of shape sensitivity. The arrows from three different examples indicate only the tip size, independent of their Young's modulus. At relatively large tip sizes ($O(100\mu\text{m})$), the optimal tip geometry, where stress is uniformly distributed along the contact area, has a theoretical pulloff force of 50-100 times that of a poor tip geometry [54]. A softer material for the tip reduces deformation energy and decreases the shape sensitivity but increases the chances of fouling and clumping. In order to achieve a balance among prevention of fouling and clumping, low effective stiffness, low shape sensitivity and a wide range of possible loading conditions, it is advantageous to have smaller tips. These considerations help to explain the evolution of extremely small distal structures, such as the spatulae with dimensions of a few hundred nanometers, on the gecko.

5.2.1 Hierarchical Conformability in the Gecko

For climbing rough surfaces such as cave walls and trees, many levels of conformability are required. In the gecko, the flex of the body and limbs allows for conformation at the centimeter scale. The body presses flat against curved surfaces to reduce the pull-in forces needed to prevent pitching back. At the scale of a several millimeters, the toes conform independently to local surface variations. The bottom surfaces of the toes are covered with lamellae that conform at the millimeter scale. The lamellae consist of arrays of setal stalks, as shown in Figure 5.2 and 5.3. The consequence of the gecko's hierarchical system of compliances is that it can achieve levels of adhesion of over 500kPa on a wide variety of surfaces from glass to rough rock and can support its entire weight in shear from just one toe [16].

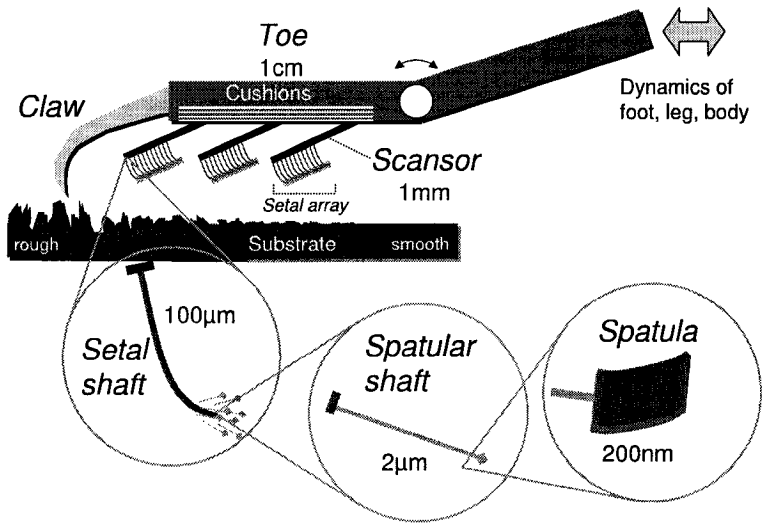

Figure 5.3: Hierarchy of compliant structures in the gecko for conforming at many length scales. (From [14], reprinted with the permission of K. Autumn).

5.2.2 Hierarchical Conformability in Stickybot

Stickybot uses an analogous, albeit much less sophisticated, hierarchy of conformable structures to climb a variety of smooth surfaces (Fig. 5.4). At the body level, Stickybot has 12 servo-motors and 32 degrees of freedom, making it highly underactuated. The structures of the torso, legs and feet are manufactured using Shape Deposition Manufacturing [21, 120] with two grades of polyurethane (Innovative Polymers: 72 Shore-DC and 20 Shore-A hardness). The upper and lower torso and forelimbs are reinforced with carbon fiber, making them the strongest and stiffest components. The middle of the torso is designed as a compromise between sufficient compliance to conform to surfaces and sufficient stiffness so that normal forces of approximately $\pm$1N can be applied at the feet without excessive body torsion.

The feet of Stickybot consist of four segmented toes molded with two grades of polyurethane that sandwich a thin polyester fabric (Fig. 5.5). The fabric flexes easily, but is relatively inextensible so that it transmits shear stresses across the surface of the foot to avoid the buildup of stress concentrations, and subsequent peeling, at the proximal regions of the toes.

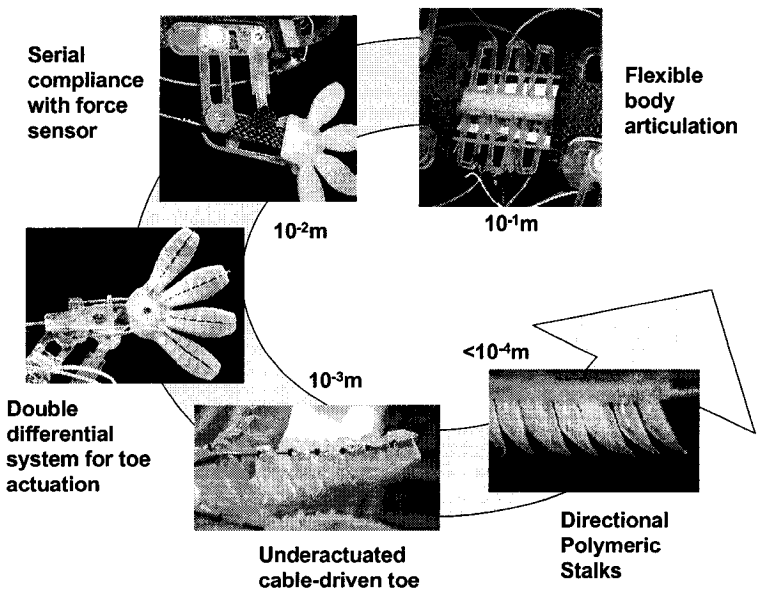

Figure 5.4: The elements of Stickybot's hierarchical compliance over a range of length scales.

The bending of the toes allows them to conform to gently curved surfaces (r $\geq$ 5cm, where r is the radius of curvature) and to peel backward in a motion that approximates the digital hyperextension that geckos use to facilitate detachment. The action is created using a servomotor connected via push-pull cables in sleeves, attached to a rocker-bogie linkage located at the foot (Fig. 5.6).

The profile of the steel cable running along the topside of each toe is calculated to achieve a uniform stress distribution when the toes are deployed on a flat surface (Fig. 5.7). Assuming an approximately uniform toe width, the sum of the forces in the y direction is given as:

$$T\sin\theta - T\sin(\theta + \delta\theta) + F_N = 0 \tag{5.1}$$

where T is the force acting along the cable, θ is the angle of the cable with respect to the horizontal, and F_N is the normal force acting on the bottom of the toe. To ensure uniform attachment of the foot, a constant pressure on the bottom of the toe is desired:

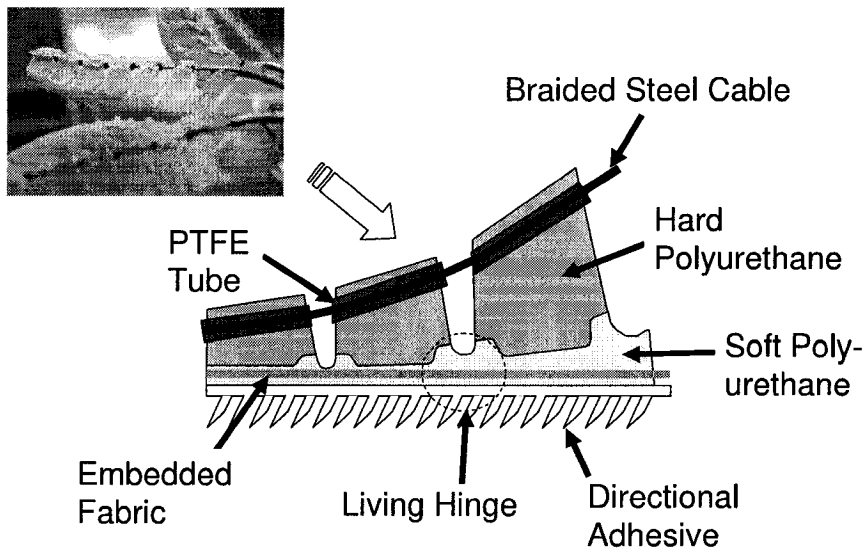

Figure 5.5: Schematic of cross section view of Stickybot toe fabricated via Shape Deposition Manufacturing.

$$\frac{T\left(\sin\left(\theta+d\theta\right)-\sin\theta\right)}{dx}=\frac{F_N}{dx}=\sigma. \tag{5.2}$$

Expanding the term $\sin\left(\theta+d\theta\right)$ and assuming that $d\theta$ is small such that $\cos d\theta = 1$ and $\sin d\theta = d\theta$ yields:

$$\cos\theta d\theta=\frac{\sigma}{T}dx. \tag{5.3}$$

Integrating both sides and solving for θ gives:

$$\theta=\arcsin\left(\frac{\sigma x}{T}\right). \tag{5.4}$$

The slope of the cable profile is thus:

$$\frac{dy}{dx}=\tan\left(\arcsin\left(\frac{\sigma x}{T}\right)\right). \tag{5.5}$$

Integrating with respect to x yields the profile of the cable:

$$y\left(x\right)=-\frac{T}{\sigma}\sqrt{1-\left(\frac{\sigma x}{T}\right)^2}, \tag{5.6}$$

which is simply a circular arc with radius T/σ.

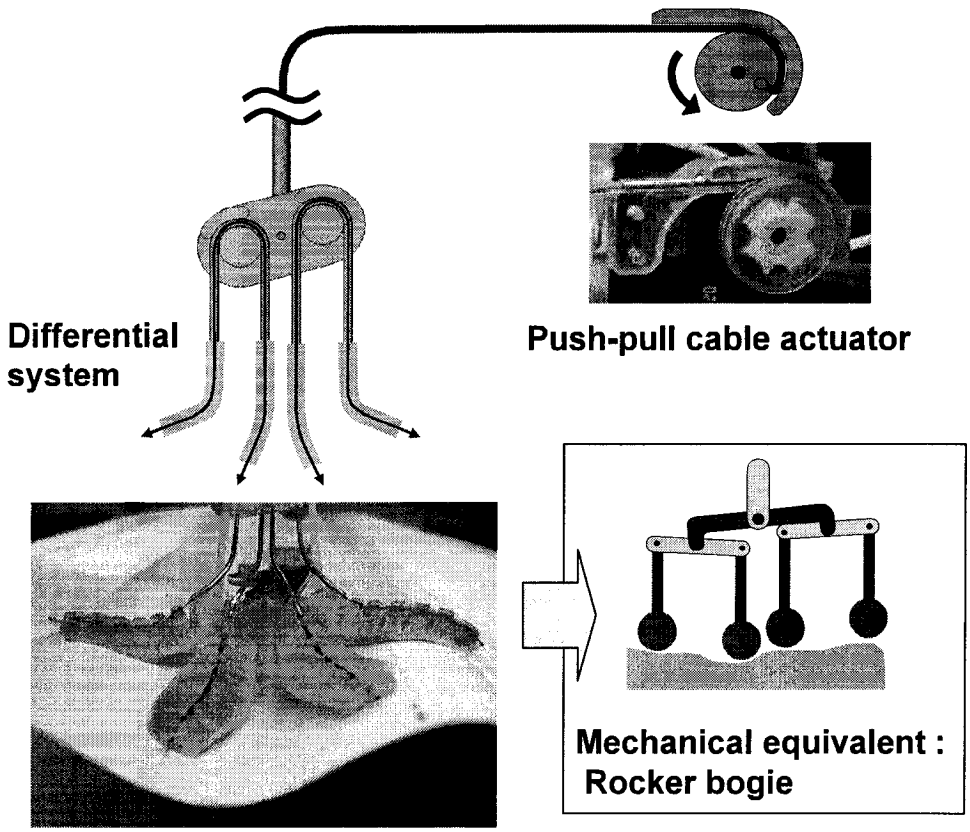

Figure 5.6: Two stage differential system actuated by a single push-pull actuator. It facilitates conformation on uneven surfaces and distributes the contact forces among four toes.

At a scale of less than hundreds of micrometers, Stickybot conforms to the surface with synthetic adhesive patches (Figure 5.5). Currently, the best results have been obtained using arrays of small, asymmetric features made out of polyurethane or silicone rubber with a modulus of elasticity of $300 - 500$kPa (Fig. 5.8). For climbing robots, loading in the tangential dominant. Therefore, the tip geometry needs to be designed for distributing the tangential load. This requirement limits the available size over which we can control the tip geometry. The bulk material modulus is chosen for low normal effective stiffness and enough range of motion in loading direction to accommodate imperfect alignment between the toes and the climbing surface. A

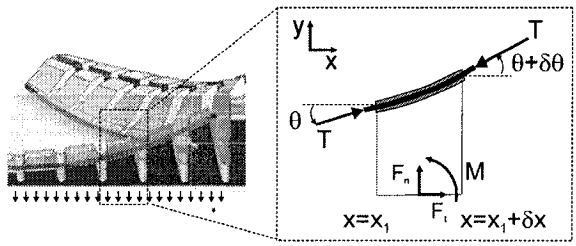

Figure 5.7: Details of nomenclature used to calculate cable profile of the toes.

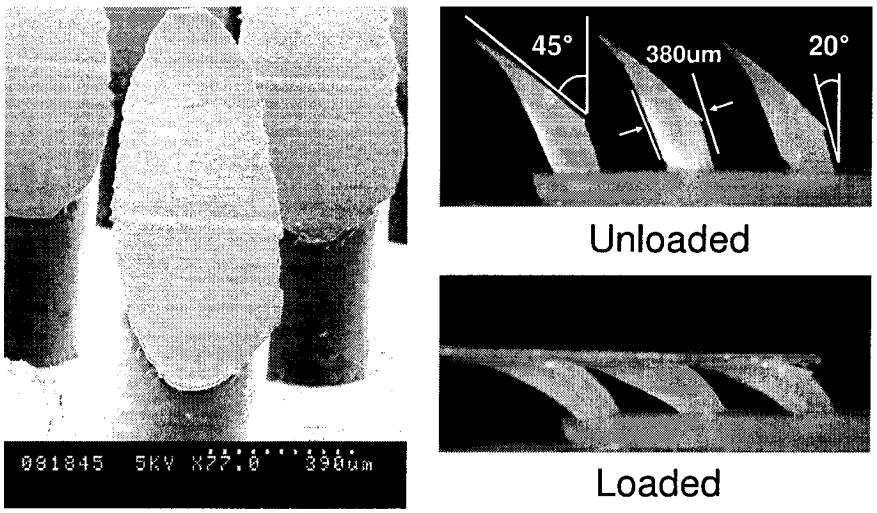

Figure 5.8: Anisotropic stalks comprised of 20 Shore-A polyurethane. Stalks measure 380 μm in diameter at the base. The base angle is 20° and the tip angle is 45°.

detailed description of the directionality of the patches is given in the following section, including the manufacturing process and importance of the anisotropic geometry. We are currently investigating alternate manufacturing methods that will yield finer feature sizes and comparable adhesion with stiffer materials.

5.3 Directional Friction and Adhesion

As discussed in [12], the gecko's toe structures are only adhesive when loaded in a particular direction. Moreover, the amount of adhesion sustained is a direct function

of the applied tangential load. In other words, the gecko can control adhesion by controlling tangential forces. The anisotropic adhesion results from the gecko's lamellae, setae, and spatulae all being angled instead of aligned vertically. Only by pulling in the proper direction does the gecko align its microstructures to make intimate contact with the surface.

Directional Polymer Stalks (DPS) were designed and manufactured to create an adhesive that is also directional like the gecko's system. DPS are made out of a soft polyurethane (Innovative Polymers, IE-20 AH Polyurethane, 20 Shore-A hardness, $E \approx$ 300kPa) and are shown in Figure 5.8. Later DPS are made out of silicon rubber which is more durable and produces more consistent adhesion force although its adhesion is lower than polyurethane. Because of the complexity of the gecko hierarchical system, the initial bulk material can be quite stiff; however, DPS begin with a fairly soft material that is already marginally sticky. Geometric properties were determined empirically, drawing inspiration from the shapes of gecko setae. Not having fine distal structures like spatulae, the DPS need low stiffness tips in order to make contact without high normal preload. The sharp and thin ($< 30\mu$m) tip shape of DPS is designed to create a softer effective stiffness when pulled parallel to the angle of inclination.

The overall mold to create DPS consists of three parts. The middle mold is made out of Delrin, which has good machinability and relatively low surface energy so that it does not bond to the curing polymer. First, V-shaped grooves are made in a 1.6mm thick Delrin sheet as shown in Figure 5.9. Before the drilling process, the top mold is fabricated by casting silicone rubber on the middle mold. On the 45° slanted surfaces and at a 20° tilted angle, 380μm holes are made in a hexagonal pattern, maximizing stalk density. The bottom mold is made out of a wax that has the Stickybot toe pattern.

Before pouring polymer, the middle and bottom mold are assembled. After pouring polymer on this assembly, the top mold is applied, squeezing out any excess material. The DPS array is released after curing by disassembling the molds. An alternative manufacturing method has also been used to create softer and smoother tip surfaces. Instead of using a top mold, excess polymer is simply wiped off of

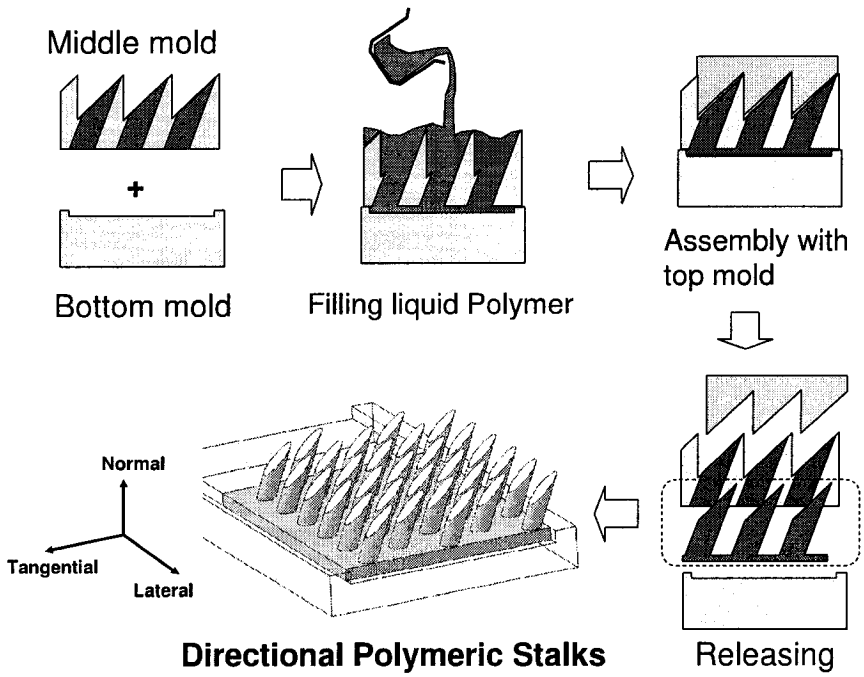

Figure 5.9: Molding process used to fabricate anisotropic patches. Mold is manufactured out of hard wax and then filled with liquid urethane polymer. A cap eliminates contact with air and creates final tip geometry.

the 45° slanted surfaces and the polymer is exposed to air during curing. Exposure to atmospheric moisture during the cure creates softer and stickier tips. However, this method is less desirable because it is difficult to control the moisture-induced softening. The wiping process is also labor-intensive.

The DPS were tested using a three-axis positioning stage and a six-axis (ATI Gamma Transducer) load cell in order to study their adhesive characteristics. The stage was able to control motion of the DPS in the normal, tangential (fore-aft), and lateral direction of the DPS (Fig. 5.9). The load cell was used to measure the pulloff force when the patches detached from a glass substrate. Patches of the DPS were brought into contact, preloaded, and then pulled away from the glass at different departure angles. When the patches are pulled in directions along the stalk-angle they exhibit moderate amounts of adhesion. When pulling in the opposite directions, adhesion disappears and Coulomb friction is observed.

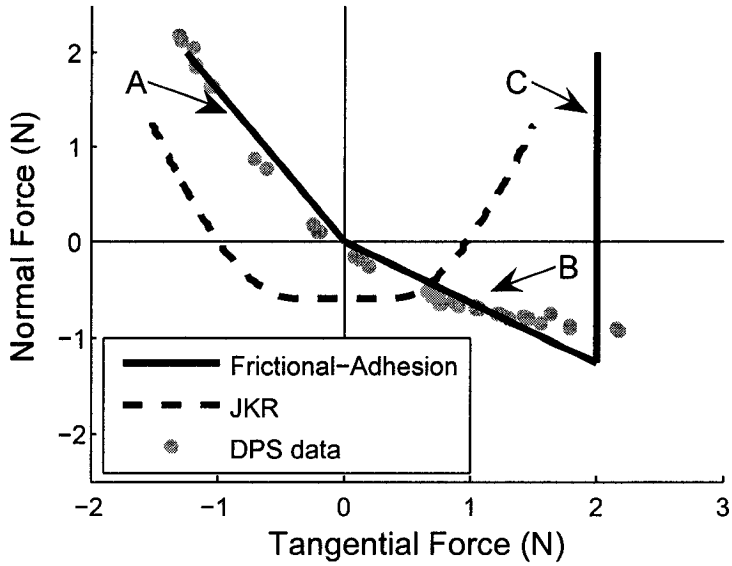

Figure 5.10: Comparison of the frictional-adhesion model [12] and the Johnson-Kendall-Roberts (JKR) model [69] with pulloff force data from a single toe of Stickybot's directional adhesive patches (513 stalks). (A) When dragged against the preferred direction, the directional patch exhibits friction and no adhesion. (B) When dragged in the preferred direction, the directional patch demonstrates adhesion proportional to the shear force, albeit with saturation at the highest levels (unlike gecko setae). (C) The frictional-adhesion model has an upper shear force limit. In comparison, the JKR model shows the typical behavior of an isotropic elastic material with adhesion.

Data from the tests are shown in Figure 5.10 for the normal-tangential plane, plotted in force-space. Figure 5.10 also shows the frictional adhesion model, which has been proposed in [12] as a simple way to describe the macroscopic gecko adhesion system, and the well-known isotropic Johnson-Kendall-Roberts (JKR) model for elastomers [69]. The JKR model provides a relationship between the contact area and the normal force for a frictionless contact. To generate the curve in Figure 5.10, the contact area was first calculated as a function of normal force and then a uniform shear strength was assumed across the contact area in order to arrive at a shear force limit, essentially relaxing the frictionless requirement after determining the contact area. While this may be a rough approximation, it is able to provide a qualitative

picture of the forces that can be sustained by contacts fitting the JKR model. The frictional adhesion model has been scaled to fit the data from the DPS patches and the JKR model has been scaled for comparison purposes. Mathematically, the frictional adhesion model is given by:

$$\begin{array}{c} F_N \geq -\frac{1}{\mu} F_T \\ F_N \geq -\tan(\alpha^*) F_T \end{array} \quad \begin{cases} F_T < 0 \\ 0 \leq F_T \leq F_{max} \end{cases} \tag{5.7}$$

where α^* is the critical angle [12], μ is the coefficient of friction, F_T is tangential (shear) load, taken positive when pulling in the adhesive direction, and F_N is the normal force, taken positive when compressive. The limit, F_{max}, is a function of the maximum shear load that a gecko or robot can apply, the material strength, and the shear strength of the contact interface. Equation 5.7 shows how the maximum adhesion is directly related to the amount of tangential force present.

The curves in Figure 5.10 are the respective two-dimensional limit curves for the contact, i.e. the limiting combinations of normal and tangential force that will cause the contact to fail. The DPS show behavior similar to the frictional adhesion model for the gecko and are clearly anisotropic with respect to adhesion. The DPS data also resemble data that would be obtained for peeling a sticky, elastic tape as described in the Kendall peel model [70]. In this case, although the toe patches are not peeled like a tape from one edge, the individual stalk tips do peel like tape of tapering thickness. However, the behavior of the DPS arrays at the origin (approaching zero tangential force and normal force) is closer to that of the frictional adhesion model than the Kendall tape peeling model.

Figure 5.11 shows the corresponding pulloff force data for the DPS in the normal-lateral plane. Not surprisingly, the DPS show symmetric behavior when pulled in the positive or negative lateral direction. The amount of adhesion depends on the amount of tangential loading that is also present. Taken together, the two data sets in Figure 5.10 and 5.11 represent slices of a convex three-dimensional limit surface in force space. Forces within the limit surface are safe; forces outside the surface will cause failure through sliding or detachment.

A consequence of the directional behavior of the DPS array is that the amount of

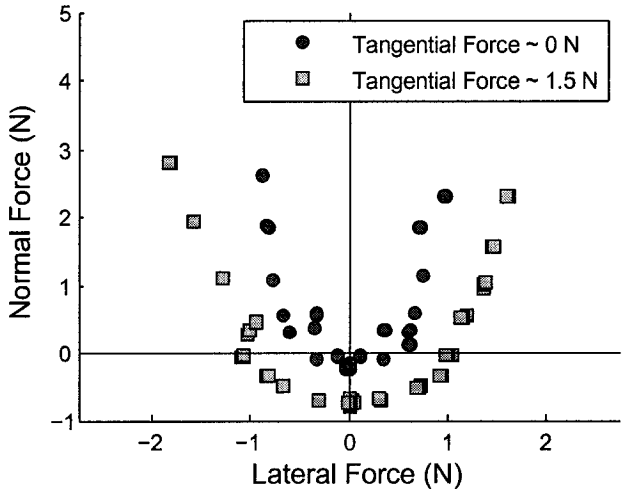

Figure 5.11: Pulloff data for the DPS patches in the normal-lateral plane. Data is shown for two different levels of tangential force, approximately 0 N and 1.5 N.

adhesion can be controlled by changing the tangential force. To increase the available adhesion, the robot can pull harder in the tangential direction. Conversely, to facilitate smooth detachment the robot can unload the foot in the tangential direction, approaching the origin in Figure 5.10. In contrast, an isotropic elastic material described by the JKR model is difficult to detach smoothly because maximum adhesion is present when the tangential force is zero.

More generally, the directional adhesion in geckos and Stickybot requires different force control strategies than isotropic adhesion. A simple two-dimensional model can be used to illustrate the difference. Figure 5.12 shows schematically the optimal tangential forces at the front and rear feet of a planar gecko or robot perched on surfaces of various inclinations. There are three equilibrium equations in the plane and four unknowns, corresponding to the magnitudes of the normal and tangential forces at each foot. The remaining degree of freedom is the magnitude of the internal (compressive or tensile) force, parallel to the surface, between the front and rear feet: $F_{Int} = F_{T1} - F_{T2}$. The internal force can be adjusted to keep each contact within its corresponding limit surface. Let $\mathbf{F_i} = [F_{Ti}, F_{Ni}]$ be the contact force at the i^{th} foot. The contact model can be defined by a parametric convex curve $\mathbf{R}(x, y)$, with

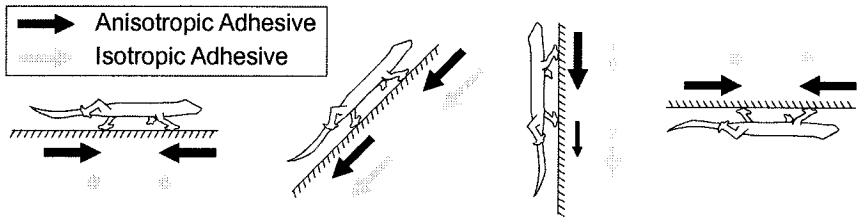

Figure 5.12: Schematic of optimal tangential forces for a planar two-legged climber under isotropic versus anisotropic adhesion at different inclinations. Arrow directions and magnitudes shown in proportion to optimal tangential forces (dot represents zero tangential force).

points $\mathbf{F} = [F_T, F_N]$ lying inside the curve being stable contacts. The distance any particular foot is from violating a contact constraint is then:

$$d_i = \min_{x,y}(||\mathbf{F_i} - \mathbf{R}(x,y)||). \tag{5.8}$$

For a model with two feet in contact with the surface, the overall stability margin becomes $d = \min(d_1, d_2)$, where d_1 represents the front foot and d_2 represents the rear foot.

Results of optimizing stability for the planar model using both the contact models given in Figure 5.10 are given in Figure 5.12. On vertical surfaces the front foot must generate adhesion to prevent pitch-back. The anisotropic model predicts that the front foot should bear more of the weight, since increasing tangential force increases available adhesion. The opposite is true for the isotropic model, namely that the rear foot should bear more weight because tangential forces on the front foot decrease adhesion. On inverted surfaces, the isotropic model predicts zero tangential forces since gravity is pulling along the normal, maximizing adhesion. Alternatively, the anisotropic model cannot generate adhesion without tangential forces and in this case the rear foot must be reversed and both feet must pull inward to generate tangential forces that will produce enough adhesion for stability. Interestingly, the anisotropic model also predicts the same foot reversal strategy is optimal on level ground, which would increase the maximum perturbation force that could be withstood. The predictions of the anisotropic model qualitatively match observations of geckos running on walls and ceilings and reorienting their feet as they climb in different directions

[13].

5.4 Distributed Force Control

5.4.1 Distributed Force Control in the Gecko

As the previous section suggests, unlike a walking or running quadruped, a climbing gecko or robot must pay continuous attention to the control of internal forces whenever its feet are in contact with the climbing surface. In the gecko, it has been observed that even at speeds of over 1m/s, attachment and lift-off are smooth, low-force events[13]. The gecko does not need to produce decelerating contact forces while climbing, but it does need to adjust the orientation of its feet as it maneuvers, to ensure that toes are always loaded in the proper direction for adhesion. On overhanging surfaces the body-oriented lateral forces are high, as one would expect, and directed inward toward the center of mass. Geckos can also use their tails to affect the dynamic force balance. If the front feet lose their grip, the tail immediately presses against the wall and the rear legs provide the necessary pull-in force [13].

5.4.2 Distributed Force Control in Stickybot

To achieve smooth engagement and disengagement and control of internal forces, Stickybot employs force feedback in the tangential (fore-aft) direction, coupled with a grasp-space stiffness controller. The control is implemented in hardware using a single master microcontroller (PIC18F4520) and four slave microcontrollers (PIC12F683) connected using an I^2C bus. The master microcontroller runs the control code and outputs the twelve pulse-width-modulated signals to independently control each of Stickybot's servos (two servos for each leg and an additional servo for flexing the toes). Each slave microcontroller reads and digitizes the analog force sensor data from a single leg and transmits that digital data to the master over the I^2C bus.

5.4.3 Leg compliance design for force control

Geckos exhibit dynamic climbing, involving extensive usage of body articulation and fluctuation of kinetic energy. However, the desired behavior of the Stickybot is smooth and reliable quasi-static climbing. In order to minimize the contact forces on the feet, a nearly constant speed is desired with minimum fluctuations in force in the vertical and normal directions. Therefore, the desired trajectory of the body is straight line with respect to the ground coordinate frame. As shown in Figure 2.3, the desired nominal trajectory of the foot is obtained from the body trajectory. In this case, the desired foot trajectory is also straight line.

The Stickybot legs have three degrees of freedom with two actuators. In tangential (fore-aft) direction, R/C servo motors control force with serial compliance. A pair of magnets and a Hall effect sensor allow for mapping from deflection of the compliant element to force. In the normal direction to the surface, wing motors control foot position with serial compliances as shown in Figure 5.13. Fore-aft motion is accomplished with a parallelogram linkage. The upper link of the parallelogram is a prismatic joint with an internal spring, which provides the dominant lateral compliance of the leg. The lateral compliance is large enough to account for the deviation between the desired straight-line trajectory of the foot with respect to the body and the arc traced by the parallel linkage. Ideally, an additional actuator would be required in the lateral direction to control all three force components at the foot.

In the sagittal plane shown in Figure 5.13, compliance is crucial for achieving the desired behavior. The tangential compliance needs to tuned to provide the desired amount of deflection from gravity and to actively distribute the forces among the legs. The normal compliance in wing degree of freedom allows for the reliable control of the preload for the DPS. This is the most critical part of the force control system for reliable climbing. The DPS require a small, but repeatable amount of preload in the normal direction to engage the surface reliably. If the applied preload is too large, it will tend to push the robot away from the wall and disengage the other attached feet. Unlike the case in motion over level ground, vertical climbing requires continuous attention to the ratios of forces in the normal and fore-aft directions. In operation, one Stickybot foot can create about 20g of normal force without disturbing

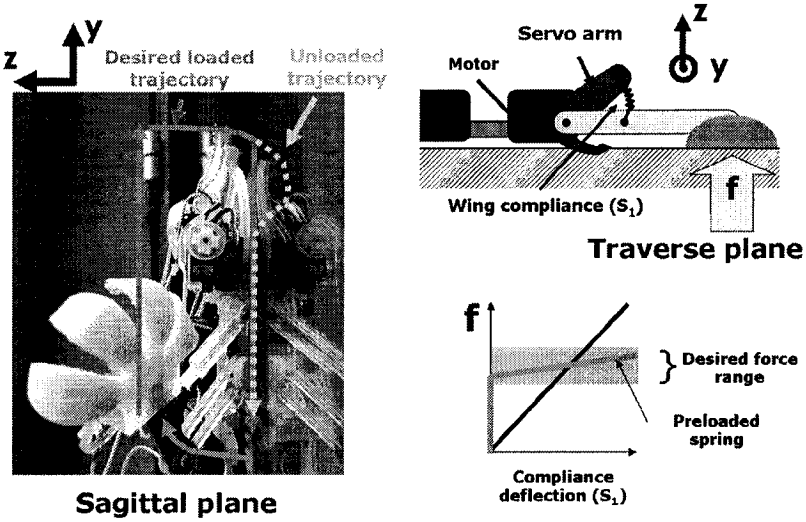

Figure 5.13: (left) Stickybot loaded and unloaded foot trajectories are shown in the sagittal plane(y-z), (right) Schematic representation of the wing compliance and the force-deflection relationship for a linear spring as compared to the preloaded case.

the balance of the body, whereas the typical vertical force per foot is around 200g which is a half of the body weight.

In order to assure reliable attachment of feet, a reliable preload force is required. From this standpoint, the compliance in the wing direction should be large so that minor variations in the attitude of the body and the distance between the body and the wall do not produce significant variations in the normal force. However, if the compliance is very soft, there is a large wasted motion in loading up the compliance until the desired value of force is achieved and in unloading it as the foot is detached. A solution to this problem is to use a soft extension spring, in series with the wing actuator, with a fixed preload such that the spring only starts to stretch when a certain force level is exceeded. The relationship between force and wing compliance deflection is shown in Figure 5.13. The shaded band indicates the desired range of force in the normal direction.

Following the notation introduced in Chapter 2, we can calculate the Jacobian matrix for the leg. Here, we assume that the ankle is a spherical joint and we ignore the rotation of the foot:

$$J = \begin{bmatrix} 2 & 0 & 0 \\ 0 & 50 & 0 \\ 0 & 0 & 50 \end{bmatrix}.$$

The joint space compliance is given as

$$C_j = \begin{bmatrix} 5 & 0 & 0 \\ 0 & 0.0011 & 0 \\ 0 & 0 & 2.8 \end{bmatrix}.$$

The dimensions are mm for length and radians for angles. Therefore, the compliance matrix in the work space is

$$C = JC_jJ^T$$

$$C = \begin{bmatrix} 20 & 0 & 0 \\ 0 & 2.8 & 0 \\ 0 & 0 & 100 \end{bmatrix}.$$

5.4.4 Force Sensors

Stickybot's force sensors are located on its shoulder joints (Fig. 5.14) and measure the deflection of an elastomeric spring via a ratiometric Hall effect sensor (Honeywell: SS495A). The Hall effect sensor outputs an analog voltage as a function of its position between two anti-aligned magnets. This analog voltage is digitized and run through a software low-pass filter at 50Hz.

The mapping from tangential force to sensor output is affected by the nonlinearity of the viscoelastic spring and the Hall effect sensors' output as a function of displacement. In addition, as Stickybot's limbs rotate, both tangential and lateral forces can contribute to the displacement in the compliant element. However, due to the computation and space limitations of Stickybot's master microcontroller, the control law simply models the mapping as a linearization about zero force and zero displacement. Figure 5.15 provides a comparison of the tangential force sensor output with the tangential and lateral contact forces for two successive contact periods, as

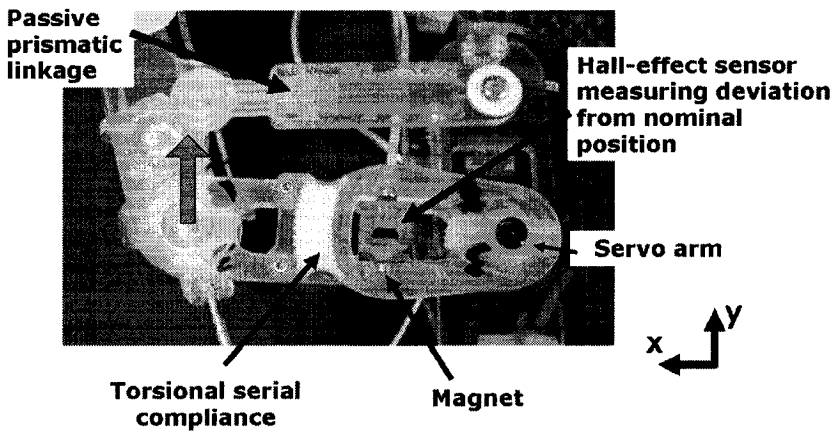

Figure 5.14: Stickybot leg compliances are shown in the dorsal plane (x-y). The tangential force sensor measures deflection of serial compliance element at the shoulder joint.

measured by a vertical force plate mounted to the same six-axis load cell used in the previously described pulloff experiments. The figure shows that the tangential force sensor tracks the tangential forces relatively closely and that the lateral forces are small because, unlike the gecko, Stickybot cannot reorient its feet.

5.4.5 Force Controller

When multiple limbs are in contact with the climbing surface, Stickybot's controller must consider how to coordinate them while continuing its vertical motion. This presents two different and sometimes contradictory goals: force balancing and leg positioning. In order to handle this tradeoff, Stickybot's controller implements a grasp-space stiffness controller [71]. Since Stickybot uses servomotors that only accept position commands, the stiffness control law is given as:

$$\mathbf{y_{cmd}}(t) = \mathbf{y_{ff}}(\phi(t)) + \mathbf{C}(\mathbf{f_s}(t) - \mathbf{f_d}(\phi(t))) \tag{5.9}$$

where $\mathbf{y_{cmd}}$ is the vector of stroke servo commanded positions, $\mathbf{y_{ff}}$ is the feed forward position command (open loop gait), $\mathbf{C}$ is the compliance matrix, $\mathbf{f_s}$ is the vector of force sensor readings, $\mathbf{f_d}$ is the vector of desired tangential forces, and $\phi(t)$ is a

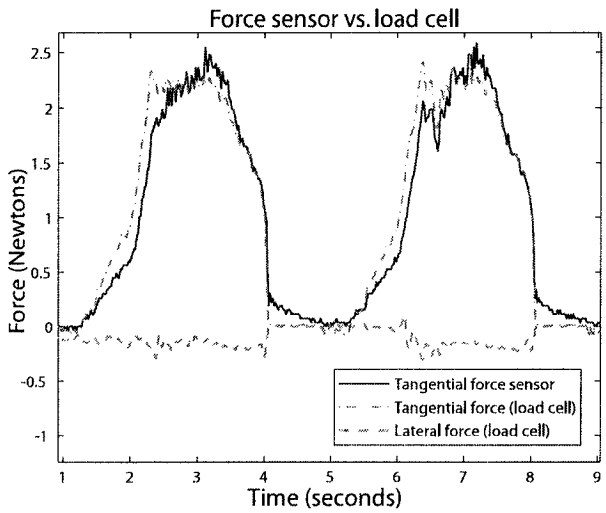

Figure 5.15: Unfiltered tangential force sensor readings compared to tangential and lateral forces measured using a force plate mounted to a load cell.

function that maps from continuous time into periodic gait phase. While a diagonal compliance matrix, $\mathbf{C}$, would result in independent leg control, during stance it is defined as:

$$\mathbf{C} = \mathbf{G}^{-1}\mathbf{C_0}\mathbf{G} \tag{5.10}$$

where $\mathbf{C_0} \neq \mathbf{I}$ is a diagonal gain matrix and $\mathbf{G}$ is the grasp matrix given as:

$$\mathbf{G} = \frac{1}{2}\begin{bmatrix} 1 & 1 & 1 & 1 \\ 1 & -1 & 1 & -1 \\ 1 & 1 & -1 & -1 \\ 1 & -1 & -1 & 1 \end{bmatrix} \tag{5.11}$$

The grasp matrix is comprised of four independent "grasp modes", or ways to linearly combine the force sensor data. The first row in $\mathbf{G}$ corresponds to summing the tangential forces (Fig. 5.16). The second row corresponds to a measure of the sum of moments about the center of mass (the difference between total tangential force on the left and right limbs). The third and fourth rows are chosen such that $\mathbf{G}$ is orthogonal, thereby leaving four independent modes of control. The chosen values for those rows correspond to fore-aft and diagonal coupling of the limbs respectively.

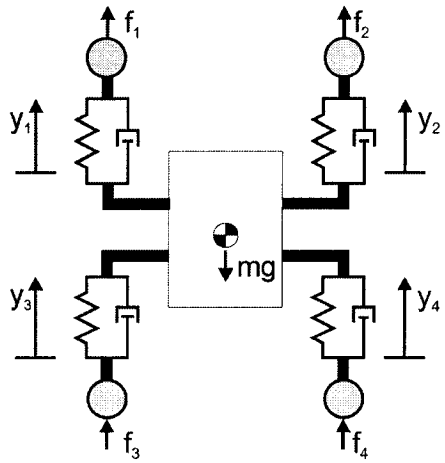

Figure 5.16: Schematic used to generate values for the grasp matrix

The implementation of stiffness control in grasp space creates a framework for force distribution. By increasing the compliances of all but the total-tangential mode, the robot will evenly distribute the forces between feet and achieve force balance while remaining stiff to variations in loading.

5.5 Results

Stickybot is capable of climbing a variety of surfaces at 90° including glass, glossy ceramic tile, acrylic, and polished granite at speeds up to 4.0cm/s (0.12bodylengths/s, excluding the tail). The maximum speed of Stickybot on level ground is 24cm/s and is limited by the speed of its actuators (Table 5.1).

Figure 5.17 presents typical force plate data of Stickybot climbing vertical glass. The left side shows data from the rear left foot and the right side displays data from the front right foot. Forces are in Newtons and time in seconds. Data from two successive runs are shown to give an indication of the repeatability.

Section A (0 to 1.5 seconds) represents the preloading and flexing of the foot. There is almost no force in the lateral (X) direction during preload. The tangential force (-Y) is increasing. Although each foot would ideally engage with negligible normal force, there is a small amount of positive normal force during engagement.

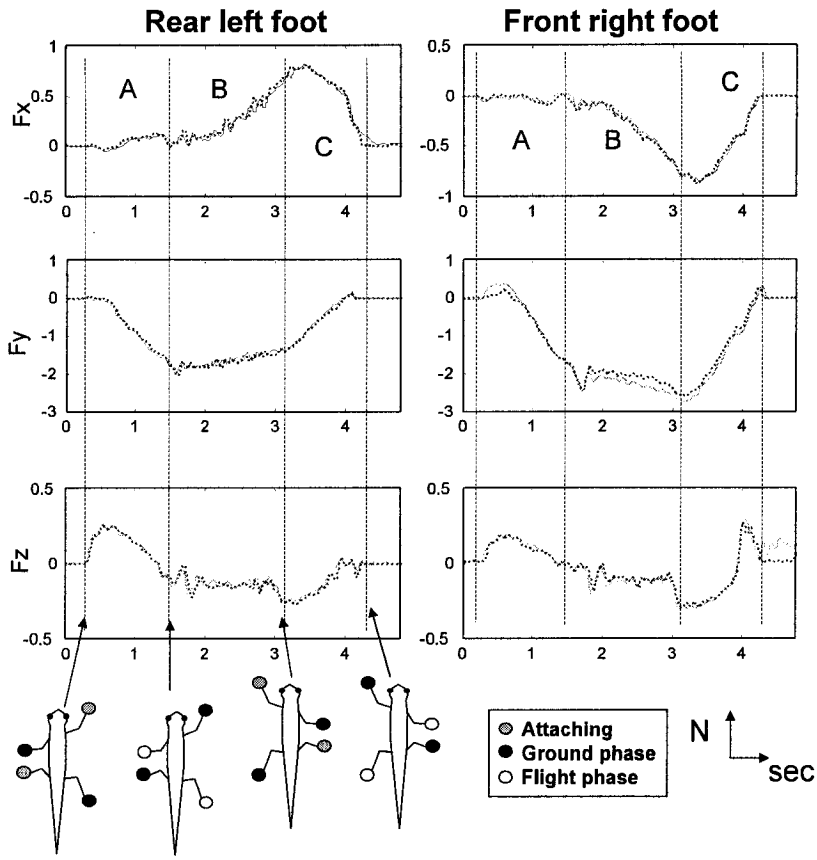

Figure 5.17: Force plate data of rear left foot (left) and front right foot (right) of Stickybot climbing with a 6s period at a speed of 1.5cm/s. Data filtered at 10Hz. Two successive runs are shown to illustrate repeatability.

Weight transfer between diagonal pairs also occurs during section A.

Section B represents the ground stroke phase. There are equal and opposite forces in the X-direction for the front right and rear left feet, indicating that the legs are pulling in toward the body. This helps stabilize the body and is similar to the lateral forces exhibited in geckos (and in contrast to the *outward* lateral forces observed in small running animals such as lizards and insects) [13]. The Y-direction shows relatively steady tangential force, and the Z-direction indicates adhesion on both the front and rear feet. Note that this differs from gecko data, in which the rear feet exhibit positive normal force [13]. This is due to the fact that Stickybot uses its tail

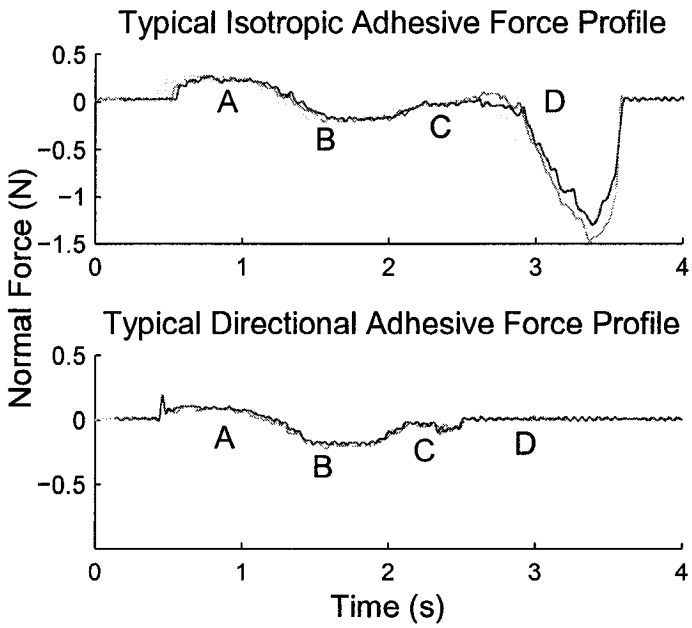

Figure 5.18: Comparison of normal force profiles of anisotropic and isotropic patches on a climbing robot. Point A on the curves refers to the preloading phase of the cycle. Point B highlights when the foot is in the adhesive regime during a stroke. Points C and D are when the foot is unloaded and detached, causing large normal forces in the case of the isotropic patch.

to prevent the body from pitching back, and geckos usually use their rear feet.

In section C, Stickybot releases the feet both by reducing the tangential force (Y) and by peeling (utilizing digital hyperextension). Both the front and rear feet exhibit low detachment forces in the Z-direction, especially the rear foot. We note also that the transition between B and C is accompanied by a temporary increase in adhesion (-Z force) and subsequent decrease as the opposite diagonal feet come into engagement.

Figure 5.18 shows a comparison of the force data for climbing with directional versus isotropic adhesive elastomeric pads. In this test, the isotropic pads were composed of arrays of pillars connected by a thin outer membrane of soft polyurethane (Innovative Polymers: 20 Shore-A hardness) to increase the contact area on smooth surfaces. The data for three successive cycles are shown to give an estimate of cycle to cycle

variability. In each case, the robot cycled a single leg through an attach/load/detach cycle using the same 6-axis load cell as in the previous tests. The other three limbs remained attached to the wall. As the plots show, the isotropic patches required a somewhat larger normal force (A) to produce comparable amounts of combined tangential force and adhesion for climbing (B). The unloading step for the anisotropic patches (C) is accomplished rapidly and results in negligible detachment force as the leg is removed. In contrast, the isotropic patch requires a longer peeling phase (C) and produces a very large pull-off force as the leg is withdrawn. This large detachment force was the main limitation of the isotropic patches, producing perturbations that frequently caused the other feet to slip.

Fig.5.19 shows the tangential and normal contact forces exerted by Stickybot's front left foot during one climbing step. The limit surface provides useful information in planning force trajectories for the feet during an attachment, loading and detachment cycle. Stickybot only controls internal forces in the tangential direction, and because we are climbing vertically, the lateral forces are negligible. Therefore, only the tangential-normal cross section of the limit surface is shown. Also, when climbing, Stickybot generally does not achieve a full normal preload to obtain maximum adhesion as shown in Figure 5.10. The characteristic angle, α, in the fourth quadrant slightly increases as the preload increases. Consequently, we assume that $\alpha^* \approx 15°$, consistent with a light preload whereas the maximum angle is 25°. A nominal force cycle starts with a modest preload (A) to bring the DPS patches into good contact with the climbing substrate. However, the normal force should not be so large that it tends to push the robot off the wall. The shear forces are then increased (A-B) so that the available adhesion also increases for the stance phase (B). Toward the end of the stance phase, the opposite (right) front foot requires an initial normal preload, which increases the required adhesion at the left foot (C) to maintain equilibrium. When it is time to detach the foot, the shear load and adhesion are simultaneously reduced (C-D) and transferred to the right front foot. Because the limit surface of the DPS intersects the origin, the foot can be released effortlessly and smoothly (D), with little energy expended in detaching it from the surface. The actual forces for a typical cycle are plotted in Figure 5.19 and labelled with respect to idealized cycle

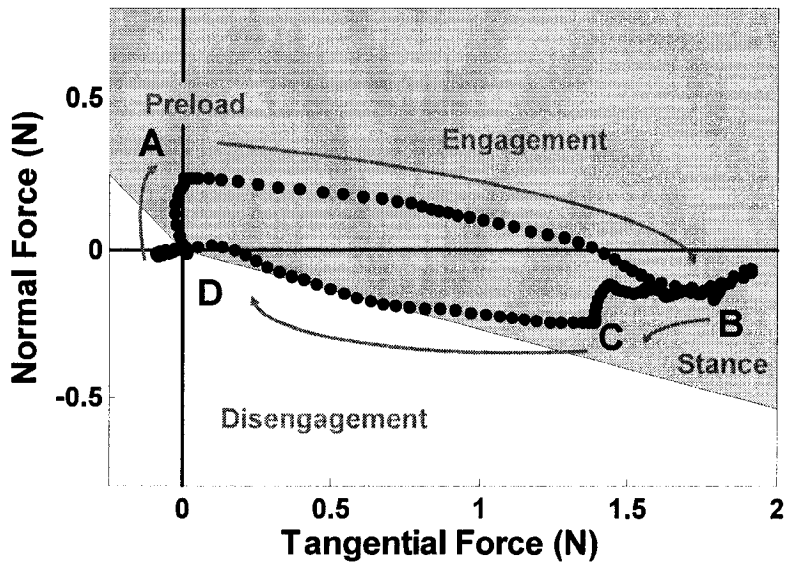

Figure 5.19: Tangential and normal contact forces of StickyBots front left foot during one climbing step. Approximate (Eq. 1) contact limit surface for one foot based on tests of individual DPS patches is also shown. Initial normal preload (A) brings DPS patches into contact with the climbing substrate and then increasing tangential force allows the foot to sustain the required adhesive loads (A-B). At the end of stance (B) the right front foot is brought into contact, increasing the adhesive force at the left foot (C). Smooth detachment is achieved by moving the contact force to the origin in force-space and intersecting the limit surface (D).

(A-D). The only significant differences are due to dynamic effects when the opposite foot is coming into contact (B-C) and at liftoff (D).

5.6 Discussion

Taking cues from geckos, Stickybot uses three main principles to climb smooth surfaces. First, it employs *hierarchical compliance* that conforms at levels ranging from the micrometer to centimeter scale. Second, Stickybot takes advantage of *directional*

Table 5.1: Physical Parameters for *Stickybot*

Body size	600 x 200 x 60 mm (excluding cables)
Body mass	370 g (including batteries and servo circuitry)
Maximum speed	4.0 cm/s (0.05 bodylength/s)
Servo motors	Hitec HB65 x 8 Hs81 x 4
Batteries	lithium polymer x2 (3.7 V, 480 mAh per pack)

adhesion that allows it to smoothly engage and disengage from the surface by controlling the tangential force. This prevents large disengagement forces from propagating throughout the body and allows the feet to adhere themselves to surfaces when loaded in shear. Interestingly, the motion strategy for engaging adhesives is similar to that used for microspines [10]. Third, Stickybot employs *force control* that works in conjunction with the body compliance and directional adhesive patches to control the tangential forces in the feet.

Some of Stickybot's directional adhesive patches have been in continuous use for over 6 months without significant loss in performance; however, because the DPS are made from a polyurethane that degrades with time, their sharp geometric features will eventually dull and the patches will begin to lose some of their adhesive performance. As discussed in Section 5.2, the DPS use relatively large feature sizes and a soft material and therefore require periodic cleaning with a lint roller to maintain enough performance to allow Stickybot to climb well. Another limitation is that the stalk tips can fold on themselves; however, in this case, they can be reconditioned via a more thorough cleaning with soap and water.

The introduction of better adhesive structures with improved hierarchical compliances will allow Stickybot to climb rougher surfaces and yield longer climbs with an increased resistance to becoming dirty. A first priority is to create DPS arrays of smaller stalks and a correspondingly stiffer, more durable and dirt resistant grade of polymer. Other improvements include improved force control and more attention to the gait and control of internal forces. Additional sensors in the feet should allow the robot to detect when good or poor contact has been made, which will improve

the reliability of climbing on varying surfaces. Additional degrees of freedom in the body should allow the robot to master vertical-horizontal transitions and other discontinuities. Once the climbing technology is understood, the ability to climb smooth surfaces will be integrated into the RiSE family of robots in an attempt to design a machine capable of climbing a wide variety of man-made and natural surfaces using a combination of adhesion and microspines [109].

Chapter 6

Conclusions

6.1 Summary

Flexible musculoskeletal structures are one of the "functional principles" of biological models that can inspire designers to create legged robots that are faster, lighter, more robust and easier to control than their traditionally-designed predecessors. Biological study provides numerous examples of the passive roles of muscles, ligaments and tendons.

Although the biological structures found in animal legs are exceedingly complicated, the behavior of these structures often suggests simplified templates that are practical for robotic implementation. For limited tasks, under limited operating conditions, a passive mechanical system can approximate the behavior of the biological counterpart well enough to allow a small robot with a simple control system to perform impressive feats such as running at 15 body-lengths/second or climbing a sheer wall.

An approach is presented in this thesis for the design of compliant leg structures, suitable for application in small robots. The procedure consists of:

1. Bio-inspiration and observation, typically drawing from multiple animal examples;

2. abstraction, and hypothesis of a desired behavior consisting of a periodic *loaded*

trajectory and *compliance matrices* at one of more points along the trajectory;

3. design of robot limbs that approximate the desired behavior through a combination of a small number of position-controlled degrees of freedom and discrete passive compliant elements;

4. analysis and verification that the robot performs as desired;

5. refinement of the trajectory, limb kinematics and compliances as needed.

Following this approach, three bio-inspired robots were designed and presented as examples. First, several design features for autonomous running robots were presented. The iSprawl hexapod was introduced, drawing upon the general design of a previous series of running robots. A novel flexible power transmission using push-pull cables was presented. Working with the new power transmission system, compliant underactuated legs were designed and tuned for fast and smooth running. The tuning process was based on motion tracking results from a high-speed video camera in combination with ground forces measured using a force plate. The result of the tuning is smooth running at 2.3m/sec corresponding to 15 bodylengths/sec.

A second robot, Spinybot, was presented as an example of using compliant linkages to allow small spines to engage asperities (small bumps or pits) on the surface of a vertical wall. The design of Spinybot was inspired by the way in which cockroaches and other insects climb vertical surfaces. The design principles behind the suspensions for the arrays of spines on the toes of Spinybot include provisions for conforming to non-flat surfaces with minimum preload and distributing loads among many spines. The highly under-actuated legs of Spinybot are designed to achieve a particular trajectory that helps spines to gently touch the wall and scrape downward until they engage an asperity. Subsequently, the toes become stiffer as the foot starts to support the vertical load of the robot. Spinybot climbs reliably on a variety of hard, outdoor surfaces including concrete, stucco, brick, and dressed sandstone with average asperity radii >25 μm.

The final example of bio-inspired underactuated design is Stickybot, which is capable of climbing smooth vertical surfaces using van der Waals forces. Stickybot is

inspired by the gecko, and adopts several of the design principles that allow geckos to climb. Among the most important of these are: a hierarchy of compliant structures to conform to surfaces at multiple length scales from centimeters to micrometers; directional adhesion that allows smooth attachment and detachment; a force control scheme that distributes loads among the feet and works with directional adhesion to control the adhesive forces via control of tangential forces at the feet.

Stickybot employs multiple levels of underactuated compliant mechanisms to distribute forces at the levels of the legs, toes and stalks on the undersides of the feet. Stickybot's feet are covered with directional polymer stalks, a unique, tapered elastic structure that conforms to flat surfaces without producing large stress concentrations at the leading edge, which would cause peeling and premature detachment. The toes of Stickybot contain an embedded fabric that is flexible but relatively inextensible, again to avoid the buildup of shear stress concentrations at the proximal regions of the toes. The actuation of the toes is accomplished with a push-pull cable mechanism (derived from iSprawl) that achieves an approximately uniform normal stress when the toes are brought into contact with a surface. Again, this helps to prevent stress concentrations and premature detachment (by peeling) of the feet. As consequence of these various innovations, Stickybot can climb smooth surfaces such as glass, tile and plastic at 4-6cm/sec.

6.2 Future directions

For better performance in various tasks, there are several directions for future research on compliant underactuated mechanism design. First, the compliances should ideally be adjustable during operation. For example, for a running robot such as iSprawl, a significant improvement in the performance may be possible by adapting the stiffness of the rotary and axial elements according to the phase of the leg. When the robot legs are thrusting, the compliance should be moderate so that there is not too much wasted motion. Conversely, when the legs are dragging, the compliance should be very high. This effect could possibly be obtained by using nonlinear compliances. However, for a wider range of tasks, which may include climbing over obstacles or

up steep slopes, the values of the compliances should be dynamically adjustable for best performance. In an analogous application, recent research has shown that prosthetic knee joints with adjustable levels of stiffness and damping are preferable for a range of conditions including walking and climbing up or down stairs. Unfortunately, the implementation of variable-compliance elements introduces significant complexity, particularly at small scales. This remains an area for future work.

Further development of the methodology on compliant mechanism design is another area of research. The approach taken in this thesis permits a rapid cycle of design, fabrication, testing and analysis. However, the critical step of synthesizing particular structures requires considerable intuition and experience. A first step could be to automate the parametric redesign of leg structures, tuning them in response to the information obtained from testing and analysis. Unfortunately, it is still not easy to identify the optimal ground reaction force profiles that will lead to the best performance of a robot in a desired task. Once the desired ground reaction profile has been identified, it is more straightforward to adjust the design parameters such as the link lengths, compliances, etc.

Another future direction of the research will be improvement of the adhesive stalks, DPS, for adhering to a wider range of surfaces. The current DPS produce useful adhesive forces on contact with materials having a narrow range of surface roughness, and they need regular cleaning to maintain performance. DPS lack the hierarchical, nano and micro-scale structure of real gecko lamellae and setae, which permit adhering to rough and dirty surfaces without frequent cleaning. Therefore, the main goal of future directional adhesive research is to develop a hierarchical structure, integrating smaller fibrillar structures onto bigger, DPS-like, stalks to expand the applicable range of surfaces. Other future directions of DPS research include optimization of the tip geometry for more reliable attachment and directionality and exploration in materials science to achieve better self-cleaning. This research requires a fundamental understanding of the behavior of structured materials over a wide range of length scales and the development of novel manufacturing technologies that integrate meso-scale and sub-micrometer fabrication. This research may lead to a vast expansion of capabilities for bio-inspired designs, as we very gradually approach the complexity of

the structures found in nature.

Appendix A

Appendices

A.1 Crank-Slider Kinematics

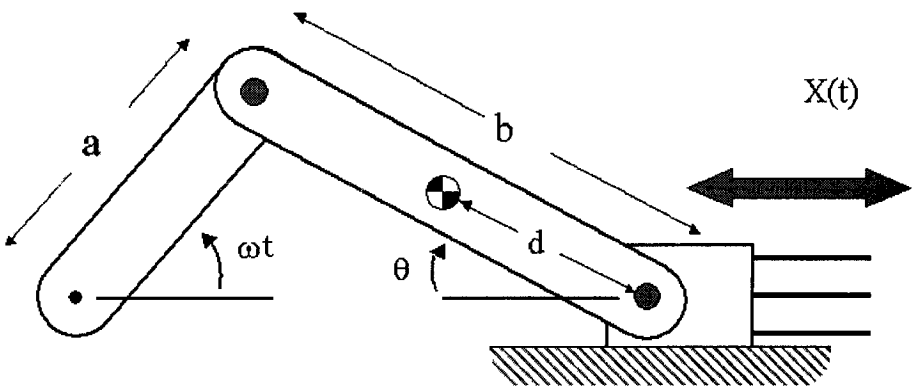

Figure A.1: Schematic of Crank and Slider

By inspection, the slider-crank equation is

$$X(t) = a\cos(\omega t) + b\cos(\arcsin(\frac{a}{b}\sin(\omega t)))$$

where

$$\omega = 94\ rad/s$$
$$a = 12.7\ mm$$
$$b = 38\ mm$$
$$d = 20\ mm$$

For these values, the stroke is an approximately sinusoidal motion of amplitude 12.7 mm.

The kinetic energy stored in the double crank and slider mechanism can be calculated from the physical parameters:

$$I_a = 1177.4\ g\,mm^2 (for\ both\ cranks)$$
$$I_b = 2908\ g\,mm^2 (each\ connecting\ rod)$$
$$m_b = 4.32\ g\ (each\ connecting\ rod)$$
$$m_{slider} = 6.48\ g.$$

However, the total rotational kinetic energy is dominated by the motor inertia, $I_m = 409\,g\,mm^2$, at $\omega_m = 2239$ rad/second:

$$E_{kinetic} \approx \frac{1}{2} I_m {\omega_m}^2 = 1\ Joule$$

or about equal to the energy consumed per stride.

A.2 Spine Failure Modes

The spine/asperity contacts have three primary failure modes.

1. The spine fails plastically at its base due to tensile stress from bending.
2. The spine deflects elastically such that it slips off the asperity.
3. The asperity fails, typically as a particle becomes unbonded from the surrounding matrix.

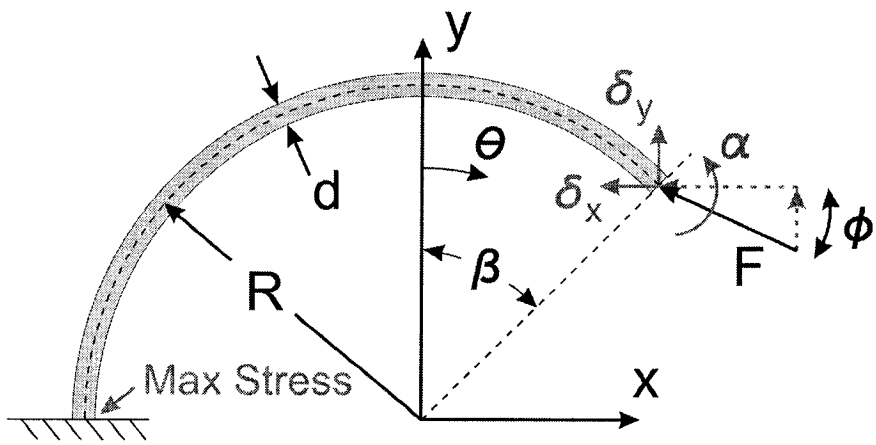

Figure A.2: Curved beam with variables used in spine failure mode analysis.

The first mode of failure is due to the tensile stress at the base of the spine. For a long curved spine, the maximum stress is essentially the same as it would be for a straight cantilever beam [111]:

$$\sigma_{max} = \frac{Mc}{I} = \frac{32fld}{\pi d^4} \propto \frac{1}{d^2} \quad (if \quad \frac{l}{d} = const)$$

where

f = force exerted on tip of the spine
d = diameter of cross section of spine
l = equivalent beam length.

The second mode of failure is excessive tip rotation. Here we can apply Castigliano's Theorem to solve for the tip deflections and rotations for a curved spine [111]. Applying a dummy end moment, M, and solving for the end rotation, α, we obtain:

$$\begin{aligned}\alpha &= \partial U/\partial M \\ &= \frac{R^2}{2EI}[-2F_y + (2F_x + F_y(\pi + 2\beta))cos(\beta) \\ &\quad +(-2F_y + F_x\pi + 2F_x\beta)sin(\beta)] \qquad \propto \frac{1}{d^2} \\ &(if \quad \frac{R}{d} = const. \quad at \ given \ \beta, \ F_x \ and \ F_y)\end{aligned} \tag{A.1}$$

(see figure A.2).

The third mode of failure is that the asperity itself may break off. The literature on surface failure or erosion (e.g. [94, 110]) for cementitious materials such as concrete, or rock with hard crystals in a weaker matrix, generally starts with the Hertz stress distribution at the contact [68]. The maximum pressure is at the center of the contact patch:

$$p_{max} = 3f/2\pi a^2 = (6fE^2/\pi^3 R^2)^{1/3}$$

where

$$\begin{aligned}a &= (3fR/4E)^{1/3} \\ E &= (1-\mu_s^2)/E_s + (1-\mu_a^2)/E_a \\ &\quad (1/R = 1/r_s + 1/r_a)\end{aligned}$$

and the subscripts s and a refer to the spine tip and asperity, respectively.

The worst case tensile stress is at the periphery of the contact patch:

$$\sigma_T = ((1-2\mu_2)p_{max})/3$$

The actual failure will depend on the local stress state, number of cracks and fracture toughness of the material. However, it will be a function of the maximum tensile stress. Therefore we can write that

$$f_{max} = [(\pi\sigma_{max}/(1-2\mu_2))^3(1/2E^2)]R^2$$

The quantity in square brackets is a constant depending on the materials so that, in the end, the maximum sustainable load is expected to vary as the square of the radii of curvature of the spine tip and asperity.

A.3 R_a and R_q Calculation

The linear roughness R_a was calculated by

$$R_a = \frac{1}{N}\sum_{i=1}^{N} abs(x[i] - \bar{x})$$

and RMS roughness R_q was calculated by

$$R_q = \sqrt{\sum_{i=1}^{N}(x[i] - \bar{x})^2},$$

where $x[i]$ is the height of point i in the profile, $\bar{x}$ is the average height of the profile, and N is the number of points in the profile.

Bibliography

[1] http://www.vortexhc.com/vmrp.html.

[2] Oscar pistorius - independent scientific study concludes that cheetah prosthetics offer clear mechanical advantages.

[3] R. McN. Alexander. Elastic Energy Stores in Running Vertebrates. *Amer. Zool.*, 24(1):85–94, 1984.

[4] R. McN. Alexander. *The Elastic Mechanisms in Animal Movement.* Cambridge University Press, Cambridge, 1988.

[5] R. McN. Alexander. Optimum muscle design for oscillatory movements. *Journal of Theoretical Biology*, 184:253–259, 1997.

[6] R. McN. Alexander and A. S. Jayes. A dynamic similarity hypothesis for the gaits of quadrupdeal mammals. *Journal of Zoology*, pages 135–152, 1983.

[7] H. Arai and S. Tachi. Position control of a manipulator with passive joints using dynamic coupling. *IEEE Transactions on Robotics and Automation*, 7(4):528–534, 1991.

[8] E. Arzt, S. Gorb, and R. Spolenak. From micro to nano contacts in biological attachment devices. *Proceedings of the National Academy of Sciences of the United States of America*, 100(9):10603–10606, 2003.

[9] E. Arzt, S. Gorb, and Ralph Spolenak. From micro to nano contacts in biological attachment devices. In *Proceedings of National Academy of Sciences*, volume 100, pages 10603–10606, 2003.

[10] A. Asbeck, S. Kim, M. Cutkosky, W. Provancher, and M. Lanzetta. Scaling hard vertical surfaces with compliant microspine arrays. *International Journal of Robotics Research*, 2006.

[11] K. Autumn. *Biological Adhesives*, volume XVII. Springer-Verlog, Berlin Heidelberg, 2006.

[12] K. Autumn, A. Dittmore, D. Santos, M. Spenko, and M. Cutkosky. Frictional adhesion: a new angle on gecko attachment. *J Exp Biol*, 209(18):3569–3579, 2006.

[13] K. Autumn, S. T. Hsieh, D. M. Dudek, J. Chen, C. Chitaphan, and R. J. Full. Dynamics of geckos running vertically. *J Exp Biol*, 209(2):260–272, 2006.

[14] K. Autumn, C. Majidi, R. E. Groff, A. Dittmore, and R. Fearing. Effective elastic modulus of isolated gecko setal arrays. *Journal of Experimental Biology*, 209:3558–3568, 2006.

[15] K. Autumn and A. Peattie. Mechanisms of adhesion in geckos. *Integrative and Comparative Biology*, 42(6):1081–1090, 2002.

[16] K. Autumn, M. Sitti, Y. Liang, A. Peattie, W. Hansen, S. Sponberg, T. Kenny, R. Fearing, J. Israelachvili, and R. Full. Evidence for van der waals adhesion in gecko setae. *Proc. of the National Academy of Sciences of the USA*, 99(19):12252–12256, 2002.

[17] C. Balaguer, A. Gimenez, J. Pastor, V. Padron, and C. Abderrahim. A climbing autonomous robot for inspection applications in 3d complex environments. *Robotica*, 18(3):287–297, 2000.

[18] C. Balaguer, A. Gimenez, J.M. Pastor, V.M. Padron, and C. Abderrahim. A climbing autonomous robot for inspection applications in 3d complex environments. *Robotica*, 18:287–297, 2000.

[19] D. Bevly, S. Dubowsky, and C. Mavroidis. A simplified cartesian-computed torque controller for highly geared systems and its application to an experimental climbing robot. *Transactions of the ASME. Journal of Dynamic Systems, Measurement and Control*, 122(1):27–32, 2000.

[20] A. A. Biewener, R. McN. Alexander, and N. C. Heglund. Elastic energy storage in the hopping of kangaroo rats. *Journal of Zoology*, pages 369–383, 1981.

[21] M Binnard and MR Cutkosky. Design by composition for layered manufacturing. *JOURNAL OF MECHANICAL DESIGN*, 122(1):91–101, 2000.

[22] L. Birglen and C. M. Gosselin. Force analysis of connected differential mechanisms: Application to grasping. *The International Journal of Robotics Research*, 25(10):1033–1046, October 1 2006.

[23] L. Birglen and C. M. Gosselin. Grasp-state plane analysis of two-phalanx underactuated fingers. *Mechanism and Machine Theory*, 41(7):807–822, 2006/7.

[24] R. Blickhan and R.J. Full. Similarity in multilegged locomotion: Bounding like a monopode. *Journal of Comparative Physiology. A, Sensory, Neural, and Behavioral Physiology*, 173(5):509–517, 1993.

[25] T. Bretl, S. Rock, and J.C. Latombe. Motion planning for a three-limbed climbing robot in vertical natural terrain. In *Proceedings of the IEEE International Conference on Robotics and Automation*, volume 205, pages 2946 – 2953. Piscataway, NJ, USA : IEEE, 2003.

[26] B. Brown and G. Zeglin. The bow legged hopping robot. In *Proceedings of the IEEE International Conference on Robotics and Automation*, 1998.

[27] M. C. Carrozza, C. Suppo, F. Sebastiani, B. Massa, F. Vecchi, R. Lazzarini, M. R. Cutkosky, and P. Dario. The spring hand: Development of a self-adaptive prosthesis for restoring natural grasping. *Auton.Robots*, 16(2):125–141, 2004.

[28] M. Catmill. Climbing. In M. Hildebrand, D.M. Bramble, K.F. Liem, and D.B. Wake, editors, *Functional Vertebrate Morphology*, pages 73–88. The Belknap Press, Cambridge, 1985.

[29] G. A. Cavagna, N. C. Heglund, and C. R. Taylor. Mechanical work in terrestrial locomotion: Two basic mechanisms for minimizing energy expenditure. *American Journal of Physiology*, 233(5):R243–R261, 1977.

[30] J. G. Cham, S. A. Bailey, J. E. Clark, R. J. Full, and M. R. Cutkosky. Fast and robust: Hexapedal robots via shape deposition manufacturing. *International Journal of Robotics Research*, 21(10), 2002.

[31] J. G. Cham, S. A. Bailey, J. E. Clark, R. J. Full, and M. R. Cutkosky. Fast and robust: Hexapedal robots via shape deposition manufacturing. *The International Journal of Robotics Research*, 21(10), 2002.

[32] J. G. Cham, J. Karpick, J. E. Clark, and M. R. Cutkosky. Stride period adaptation for a biomimetic running hexapod. In *International Symposium of Robotics Research*, Lorne Victoria, Australia, 2001.

[33] B. Chan, N. J. Balmforth, and A. E. Hosoi. Building a better snail: Lubrication and gastropod locomotion. *Physics of Fluids*, 17, 2005.

[34] J. E. Clark. *Design, Simulation, and Stability of a Hexapedal Running Robot.* PhD thesis, Stanford University, 2004.

[35] M. A. Costa and M. R. Cutkosky. Roughness perception of haptically displayed fractal surfaces. In *Proceedings of the ASME Dynamic Systems and Control Division*, volume 69-2, pages 1073–1079, 2000.

[36] N. Cowan, E.J. Ma, M.R. Cutkosky, and R.J. Full. A biologically inspired passive antenna for steering control of a running robot. In P. Dario and Chatila R., editors, *Eleventh International Symposium on Robotics Research*, volume 15. Springer Tracts in Advanced Robotics, 2005.

[37] J. J. Craig. *Introduction to Robotics: Mechanics and Control.* Addison-Wesley Longman Publishing Co., Inc., Boston, MA, USA, 1989.

[38] M. R. Cutkosky and I. Kao. Computing and controlling compliance of a robotic hand. *IEEE transactionas on Robotics and Automation*, 5:151–165, 1989.

[39] C. A. Dahlquist. Pressure-sensitive adhesives. In R.L. Patrick, editor, *Treatise on Adhesion and Adhesives*, volume 2, pages 219–260. Dekker, New York, 1969.

[40] Z. D. Dai, S. N. Gorb, and U. Schwarz. Roughness-dependent friction force of the tarsal claw system in the beetle pachnoda marginata (coleoptera, scarabaeidae). *Journal Of Experimental Biology*, 205(16):2479–2488, 2002.

[41] K. Daltorio, S. Gorb, A. Peressadko, A. Horchler, R. Ritzmann, and R. Quinn. A robot that climbs walls using micro-structured polymer feet. In *CLAWAR*, 2005.

[42] K. Daltorio, A. Horchler, S. Gorb, R. Ritzmann, and R. Quinn. A small wall-walking robot with compliant, adhesive feet. In *International Conference on Intelligent Robots and Systems*, 2005.

[43] K. A. Daltorio, S. Gorb, A. Peressadko, A. D. Horchler, R. E. Ritzmann, and R. D. Quinn. A robot that climbs walls using micro-structured polymer feet. In *International Conference on Climbing and Walking Robots (CLAWAR)*, pages 131–138, 2005.

[44] K. A. Daltorio, A. D. Horchler, S. Gorb, R. E. Ritzmann, and R. D. Quinn. A small wall-walking robot with compliant, adhesive feet. In *Int. Conf. on Intelligent Robots and Systems (IROS)*, pages 4018–4023, 2005.

[45] S. B. Emerson and D. Diehl. Toe pad morphology and mechanisms of sticking in frogs. *Biological Journal of the Linnean Society*, 13(3):199–216, 1980.

[46] W. Federle, M. Riehle, A.S.G. Curtis, and R.J. Full. An integrative study of insect adhesion: mechanics and wet adhesion of pretarsal pads in ants. *Integrative and Comparative Biology*, 42(6):1100–1106, 2002.

[47] Y. Fukuoka, H. Kimura, and A. H. Cohen. Adaptive dynamic walking of a quadruped robot on irregular terrain based on biological concepts. *Int. Journal of Robotics Research*, 22(3-4):187–202, 2003.

[48] R. J. Full, K. Autumn, J. I. Chung, and A. N. Ahn. Rapid negotiation of rough terrain by the death-head cockroach. *American Zoologist*, 38(81A), 1998.

[49] R. J. Full, R. Blickhan, and L. H. Ting. Leg design in hexapedal runners. *Journal of Experimental Biology*, 158(UL):369–390, 1991.

[50] R. J. Full and C. T. Farley. Musculoskeletal dynamics in rhythmic systems - a comparative approach to legged locomotion. *Biomechanics and Neural Control of Posture and Movement*, 2000.

[51] R. J. Full and D. E. Koditschek. Templates and anchors: Neuromechanical hypotheses of legged locomotion on land. *Journal of Experimental Biology*, 202(23):3325–3332, 1999.

[52] R. J. Full and M. S. Tu. Mechanics of six-legged runners. *Journal of Experimental Biology*, 148(AR):129–146, 2000.

[53] R.J. Full, D. R. Stokes, A. N. Ahn, and R. K. Josephson. Energy absorption during running by leg muscles in a cockroach. *Journal of Experimenatal Biology*, 201(7):997–1012, 1998.

[54] H. Gao, X. Wang, H. Yao, S. Gorb, and E. Arzt. Mechanics of hierarchical adhesion structures of geckos. *Mechanics of Materials*, 37:275–285, 2005.

[55] H. Gao and H. Yao. Shape insensitive optimal adhesion of nanoscale fibrillar structures. *Proceedings of the National Academy of Sciences of the United States of America*, 101(21):7851–7856, 2004.

[56] M. Garcia, A. D. Kuo, A. M. Peattie, P. C. Wang, and R. J. Full. Damping and size: Insights and biological inspiration. In *International Symposium on Adaptive Motion of Animals and Machines*, Montreal, Canada, 2000.

[57] A. K. Geim, S. V. Dubonos, I. V. Grigorieva, K. S. Novoselov, A. A. Zhukov, and S. Yu. Shapoval. Microfabricated adhesive mimicking gecko foot-hair. *Nature Materials*, 2:461–463, 2003.

[58] S. Gorb, M. Varenberg, A. Peressadko, and J. Tuma. Biomimetic mushroom-shaped fibrillar adhesive microstructure. *Journal of The Royal Society Interface*, 2006.

[59] A. M. Gordon, A. F. Huxley, and F. J. Julian. The variation in isometric tension with sarcomere length in vertebrate muscle fibres. *J Physiol*, 184(1):170–192, 1966.

[60] J. A. Greenwood. Contact of rough surfaces. In I. L. Singer and H. M. Pollock, editors, *Fundamental of Friction: Macroscopic and Microscopic Processes*, pages 37–56. Kluwer Academic Publishers, Dordrecht, The Netherlands, 1992.

[61] J. A. Greenwood. Problem with surface roughness. In I. L. Singer and H. M. Pollock, editors, *Fundamental of Friction: Macroscopic and Microscopic Processes*, page 5776. Kluwer Academic Publishers, Dordrecht, The Netherlands, 1992.

[62] N. C. Heglund, C. R. Taylor, and T. McMahon. Scaling stride frequencies to animal size : mice to horses. *Science*, 186(4169):1112–1113, 1974.

[63] S. Hirose. The development of soft gripper for the versatile robot hand. *Mechanism and machine theory*, 13:351, 1978.

[64] S. Hirose. Connected differential mechanism and its applications. In *International Conference on Advanced Robotics*, pages 319–325, Tokyo, Sept 1985.

[65] J. R. Hutchinson, D. Famini, D. Lair, and R. Kram. Are fast-moving elephants really running? *Nature*, 422:493–494, 2003.

[66] F. Iida and R. Pfeifer. Self-stabilization and behavioral diversity of embodied adaptive locomotion. In Fumiya Iida, Rolf Pfeifer, Luc Steels, and Yasuo Kuniyoshi, editors, *Embodied Artificial Intelligence, International Seminar, Dagstuhl Castle, Germany, July 2003*, volume LNAI 3139 of *Lecture notes in Artificial Intelligence*, pages 119–129, Berlin Heidelberg, Germany, 2004. Springer-Verlag.

[67] J. Israelachvili. *Intermolecular and Surface Forces.* Academic Press, New York, 1992.

[68] K.L. Johnson. In *Contact Mechanics*, pages 72–94. Cambridge University Press, 1985.

[69] K.L. Johnson, K. Kendall, and A.D. Roberts. Surface energy and the contact of elastic solids. *Proc. of the Royal Society A: Mathematical, Physical and Engineering Sciences*, 324(1558):301–313, 1971.

[70] K. Kendall. Thin-film peeling - the elastic term. *Journal of Physics D: Applied Physics*, 8(13):1449–1452, 1975.

[71] J. Kerr and B. Roth. Analysis of multifingered hands. *The International Journal of Robotics Research*, 4(4):3–17, 1986.

[72] A. B. Kesel, A. Martin, and T. Seidl. Adhesion measurements on the attachment devices of the jumping spider evarcha arcuata. *The Journal of Experimental Biology*, 206:2733–2738, 2003.

[73] D.S. Kim, H.S. Lee, J. Lee, S. Kim, K-H Lee, W. Moon, and T.H. Kwon. Replication of high-aspect-ratio nanopillar array for biomimetic gecko foot-hair prototype by uv nano embossing with anodic aluminum oxide mold. *Microsystem Technologies*, 2006.

[74] S. Kim, J. E. Clark, and M. R. Cutkosky. isprawl: Design and tuning for high-speed autonomous open-loop running. *The International Journal of Robotics Research*, 25(9):903–912, September 1 2006.

[75] S. Kim and M. Sitti. Biologically inspired polymer microfibers with spatulate tips as repeatable fibrillar adhesives. *Applied Physics Letters*, 89(261911), 2006.

[76] B. Klaassen, R. Linnemann, D. Spenneberg, and F. Kirchner. Biomimetic walking robot scorpion: Control and modeling. In *Proceedings of the ASME Design Engineering Technical Conference*, volume 5, pages 1105–1112, 2002.

[77] T. M. Kubow and R. J. Full. The role of the mechanical system in control: a hypothesis of self-stabilization in hexapedal runners. *Philosophical Transactions of the Royal Society of London Series B-Biological Sciences*, 354(1385):849–861, 1999.

[78] G. La Rosa, M. Messina, G. Muscato, and R. Sinatra. A low-cost lightweight climbing robot for the inspection of vertical surfaces. *Mechatronics*, 12(1):71–96, 2002.

[79] G. La Rosa, M. Messina, G. Muscato, and R. Sinatra. A lowcost lightweight climbing robot for the inspection of vertical surfaces. *Mechatronics*, 12(1):71–96, 2002.

[80] R. Lal Tummala, R. Mukherjee, N. Xi, D. Aslam, H. Dulimarta, Jizhong Xiao, M. Minor, and G. Dang. Climbing the walls [robots]. *IEEE Robotics and Automation Magazine*, 9(4):10–19, 2002.

[81] T. Libby, K. Meijer, and R.J. Full. Partioning preflex and reflex contributions toward cockroach leg stability: A simulation study. *AMERICAN ZOOLOGIST*, 41(6):1506, 2001.

[82] G. E. Loeb, I. E. Brown, and E. J. Cheng. A hierarchiacal foundation for models of sensorimotor control. *Exp. Brain Res.*, 126:1–18, 1999.

[83] J. Loncaric. Normal forms of stiffness and compliance matrices. *IEEE Journal of Robotics and Automation*, RA-3:567–572, 1987.

[84] B. Massa, S. Roccella, M. C. Carrozza, and P. Dario. Design and development of an underactuated prosthetic hand. In *IEEE International Conference on Robotics and Automation*, volume 4, pages 3374– 3379, May 2002.

[85] A. J. McClung, J. G. Cham, and M. R. Cutkosky. Dynamic maneuvering of a biologically inspired hexapedal robot. In *ASME IMECE-61150 Proceedings*, 2004.

[86] Tad McGeer. Passive dynamic walking. *International Journal of Robotics Research*, 9(2):62–82, 1990.

[87] T. A. McMahon. Mechanics of locomotion. *International Journal of Robotics Research*, 3(2):4–28, 1984.

[88] T. A. McMahon. The role of compliance in mammalian running gaits. *Journal of Experimental Biology*, 115(1):263–282, March 1 1985.

[89] K. Meijer and R. J. Full. Stabilizing properties of invertebrate skeletal muscle. *American Zoologist*, 39, 1999.

[90] K. Meijer, T.M. Libby, and R.J. Full. Passive stability provided by the musculoskeletal properties of an insect leg. *AMERICAN ZOOLOGIST*, 40(6):1129–1130, 2000.

[91] C. Menon, M. Murphy, and M. Sitti. Gecko inspired surface climbing robots. Proceedings of the IEEE International Conference on Robotics and Biomimetics (ROBIO), 2004.

[92] R. Merz, F.B. Prinz, K. Ramaswami, M. Terk, and L. Weiss. Shape deposition manufacturing. In *Proceedings of the Solid Freeform Fabrication Symposium*, volume 1-8, August 1994.

[93] L. A. Miller and S. Dudley. Analysis of a vertical compliance prosthetic foot. *The Journal of Rehabilitation Research and Development*, 34(1):52–57, 1997.

[94] A. W. Momber. Damage to rocks and cementitious materials from solid impact. *Rock Mechanics and Rock Engineering*, 37(1):57–82, 2004.

[95] J. M. Morrey, B. Lambrecht, A. D. Horchler, R. E. Ritzmann, and R. D. Quinn. Highly mobile and robust small quadruped robots. In *Int. Conf. on Intelligent Robots and Systems (IROS2003), Las Vegas*, 2003.

[96] J. G. Nichol and K.J. Waldron. Biomimetic leg design for untethered quadruped gallop. In *Proceedings of the 5th International Conference on Climbing and Walking Robots*, pages 49–54, Paris, France, 02.

[97] M. Northen and K. Turner. A batch fabricated biomimetic dry adhesive. *Nanotechnology*, 16:1159–1166, 2005.

[98] A. Peressadko and S.N. Gorb. When less is more: experimental evidence for tenacity enhancement by division of contact area. *Journal of Adhesion*, 80(4):247–261, 2004.

[99] B. N. J. Persson and S. Gorb. The effect of surface roughness on the adhesion of elastic plates with application to biological systems. *Journal of Chemical Physics*, 119(21):11437–11444, 2003.

[100] I. Poulakakis and M. Buehler. Modeling and experiments of untethered quadrupedal running with a bounding gait:the scout ii robot. *International Journal of Robotics Research*, 24(4):239–256, 2005.

[101] G. Pratt and M. Williamson. Series elastic actuators. In *Proceedings of the IEEE/RSJ International Conference on Intelligent Robots and Systems*, volume 1, pages 399 – 406, July 1995.

[102] G. A. Pratt. Legged robots at mit: What's new since raibert. *IEEE Robotics and Automation Magazine*, 7(3):15–19, 2000.

[103] R. D. Quinn, G. M. Nelson, R. J. Bachmann, D. A. Kingsley, J. T. Offi, T. J. Allen, and R. E. Ritzmann. Parallel complementary strategies for implementing biological principles into mobile robots. *International Journal of Robotics Research*, 22(3/4):169–86, 2003.

[104] R. D. Quinn, G.M. Nelson, R.J. Bachmann, D.A. Kingsley, J. Offi, and R. E. Ritzmann. Insect designs for improved robot mobility. In *Proc. of Climbing and Walking Robots Conference (CLAWAR01)*, pages 69–76. Berns and Dillmann eds., Prof. Eng., 2001.

[105] Marc H. Raibert. Running with symmetry. *Int. J. Rob. Res.*, 5(4):3–19, 1987.

[106] Thomas J. Roberts, Richard L. Marsh, Peter G. Weyand, and C. Richard Taylor. Muscular force in running turkeys: The economy of minimizing work. *Science*, 275(5303):1113–1115, 1997.

[107] J. Kenneth Salisbury and Mandayam A. Srinivasan. Phantom-based haptic interaction with virtual objects. *IEEE Computer Graphics and Applications*, 17(5):6–10, 1997.

[108] U. Saranli, M. Buehler, and D. E. Koditschek. Rhex: A simple and highly mobile hexapod robot. *International Journal of Robotics Research*, 20(7):616–631, 2001.

[109] A. Saunders, D. Goldman, R. Full, and M. Buehler. The rise climbing robot: body and leg design. In *SPIE Unmanned Systems Technology VII*, volume 6230, Orlando, FL, 2006.

[110] G.L. Sheldon and I. Finnie. The mechanism of material removal in the erosive cutting of brittle materials. *ASME Journal of Engineering for Industry*, 88B:393–400, 1966.

[111] C.R. Shigley, J.E.; Mischke. In *Standard Handbook of Machine Design (2nd Edition)*. McGraw-Hill, 1996.

[112] R. Siegwart, P. Lamon, T. Estier, M. Lauria, and R. Piguet. Innovative design for wheeled locomotion in rough terrain. *Robotics and Autonomous Systems*, 40:151–162(12), 31 August 2002.

[113] M. Sitti and R. Fearing. Synthetic gecko foot-hair micro/nano-structures as dry adhesives. *Adhesion Science and Technology*, 17(8):1055, 2003.

[114] M. Sitti and R.S. Fearing. Synthetic gecko foot-hair micro/nano-structures for future wall-climbing robots. In *Proceedings of the IEEE International Conference on Robotics and Automation*, volume 1, pages 1164 – 1170. Piscataway, NJ, USA : IEEE, 2003.

[115] HE ter Keurs, T Iwazumi, and GH Pollack. The sarcomere length-tension relation in skeletal muscle. *J. Gen. Physiol.*, 72(4):565–592, 1978.

[116] A. Thorstensson, G. Grimby, and J. Karlsson. Force-velocity relations and fiber composition in human knee extensor muscles. *Journal of applied physiology*, 40(1):12–16, 1976.

[117] R. Tomovic and G. Boni. An adaptive artificial hand. *IRE Transactions on Automatic Control*, 7(3):3–10, Apr 1962.

[118] O. Unver, M. Murphy, and M. Sitti. Geckobot and waalbot: Small-scale wall climbing robots. In *AIAA 5th Aviation, Technology, Integration, and Operations Conference*, 2005.

[119] J. D. Weingarten, G. A. Lopes, M. Buehler, R. E. Groff, and D. E. Koditschek. Automated gait adaptation for legged robots. In *International Conference in Robotics and Automation*, New Orleans, USA, 2004. IEEE.

[120] L. E. Weiss, R. Merz, F. B. Prinz, G. Neplotnik, P. Padmanabhan, L. Schultz, and K. Ramaswami. Shape deposition manufacturing of heterogenous structures. *Journal of Manufacturing Systems*, 16(4):239–248, 1997.

[121] Z. Xu and P. Ma. A wall-climbing robot for labeling scale of oil tank's volume. *Robotica*, 20(2):203–207, 2002.

[122] Z.L. Xu and P.S. Ma. A wall-climbing robot for labelling scale of oil tank's volume. *Robotica*, 20:209–212, 2002.

[123] H. Yao and H. Gao. Mechanics of robust and releasable adhesino in biology: Bottom-up designed hierarchical structures of gecko. *Journal of the mechanics and physics of solids*, 54:1120–1146, 2006.

[124] B. Yurdumakan, R. Raravikar, P. Ajayanb, and A. Dhinojwala. Syntheic gecko foot-hairs from multiwalled carbon nanotubes. *Chemical Communications*, 2005.

[125] P.A. Zani. The comparative evolution of lizard claw and toe morphology and clinging performance. *Journal of Evolutionary Biology*, 13:316–325, 2000.

[126] Y. Zhao, T. Tong, L. Delzeit, A. Kashani, M. Meyyapan, and A. Majumdar. Interfacial energy and strength of multiwalled-carbon-nanotube-based dry adhesive. *Vacuum Science and Tech B*, 2006.

[127] J. Zhu, D. Sun, and S.K. Tso. Development of a tracked climbing robot. *Journal Of Intelligent And Robotic Systems*, 35(4):427–444, 2002.